

# **Integrated proteome and metabolome profiling of chromophobe renal cell carcinoma**

Inaugural-Dissertation  
to obtain the academic degree  
Doctor rerum naturalium (Dr. rer. nat.)

submitted to the Department of Biology, Chemistry and Pharmacy  
of Freie Universität Berlin

by  
Yi Xiao  
from Hunan, China

February 2020  
Berlin, Germany



The present work was completed at the Mass Spectrometry Facility, Max Planck Institute for Molecular Genetics from January 2017 to December 2019 under the supervision of Dr. David Meierhofer.

I declare that this dissertation is an original report of my research, has been finished by myself and has not been submitted for any previous degree. Contributions from collaborators have been indicated clearly and acknowledged. Due references have been provided on all supporting literatures and resources.

Parts of this thesis have been published as:

Y. Xiao and D. Meierhofer (2019). "Glutathione metabolism in renal cell carcinomas progression and implications for therapies." International Journal of Molecular Sciences 20(15): 3672. <http://doi.org/10.3390/ijms20153672>

Y. Xiao, R. Clima, J. F. Busch, A. Rabien, E. Kilic, S. Villegas, S. Türkmen, M. Attimonelli, K. Jung and D. Meierhofer (2019). "Metabolic reprogramming and elevation of glutathione in chromophobe renal cell carcinomas." bioRxiv 649046. (Preprint) <http://doi.org/10.1101/649046>

Y. Xiao and D. Meierhofer (2019). "Are Hydroethidine-Based Probes Reliable for Reactive Oxygen Species Detection?" Antioxidants & Redox Signaling 31(4): 359-367. <http://doi.org/10.1089/ars.2018.7535>

1<sup>st</sup> Reviewer: Dr. David Meierhofer, Max Planck Institute for Molecular Genetics

2<sup>nd</sup> Reviewer: Prof. Dr. Kevin Pagel, Freie Universität Berlin

Date of defense: May 20, 2020



## Acknowledgements

Firstly, I would like to express my sincere gratitude to my PhD advisor Dr. David Meierhofer for his continuous support of my PhD study and the related research in the last three years, for his patience, guidance, and immense knowledge. David helped me in all the time of research and writing of this thesis. I could not have imagined having a better advisor and mentor for my PhD study.

Besides my advisor, I would like to thank the rest of my thesis committee: Prof. Dr. Kevin Pagel and Dr. Marie-Laure Yaspo, for their insightful comments and encouragement, as well as the hard questions which incited me to widen my research from various perspectives.

Also, this thesis would never be completed without the help of my cooperation partners from the Max Planck Institute for Molecular Genetics, Charité - Universitätsmedizin Berlin, and University of Bari in Italy. Therefore I would like to thank Bernd Timmermann, Jonas Felix Busch, Anja Rabien, Ergin Kilic, Sonia Villegas, Klaus Jung, Rosanna Clima, Marcella Attimonelli for the incredible cooperation and fruitful discussions regarding the experimental samples, details, and data analysis.

I thank all my formal and present colleagues in the lab, Beata Lukaszewska-McGreal, Yang Ni, Robert Gajowski, Natalie Witt, Ayham Alahmad, Vanessa Paffrath, Monica De Luise, Greta Tedesco, Ria Thielhorn for providing a friendly, warmful, and supporting working environment, for the stimulating discussions in our lab meetings, and for all the fun we had in the past years.

Last but not the least, I would like to express my deep gratitude to my friends and family, who supported me with their endless love, care, and encouragement over the years. Especially to my beautiful wife, Min Li and my adorable angel, Mia, for accompanying me and having so many happy times together, love you forever!



# Directory

Acknowledgements .....	V
Directory.....	VII
Abstract.....	XI
Zusammenfassung.....	XIII
1. Introduction .....	1
1.1 Renal cell carcinoma.....	1
1.1.1 Clear cell renal cell carcinoma.....	2
1.1.2 Papillary renal cell carcinoma.....	3
1.1.3 Chromophobe renal cell carcinoma.....	4
1.1.4 Renal oncocytoma .....	6
1.2 Similarities and differences between chRCC and RO.....	6
1.3 Glutathione salvage pathway in chRCC .....	8
1.4 Glutathione and reactive oxygen species .....	9
1.5 Hydroethidine based probes for ROS measurement .....	10
1.6 Mass spectrometry based metabolomics and proteomics .....	11
1.6.1 Mass spectrometry.....	11
1.6.2 Metabolomics.....	14
1.6.3 Proteomics.....	15
1.7 Aim of this thesis.....	17
2. Materials and methods .....	19
2.1 List of buffers .....	19
2.1.1 Buffers for proteome profiling .....	19
2.1.2 Buffers for enzymatic activity measurement .....	19
2.1.3 Buffers for western blot .....	21
2.2 Cell culture .....	21
2.3 Tissue dissection and verification of chRCC.....	22
2.4 Proteomics .....	22
2.4.1 Sample preparation for proteome profiling .....	22
2.4.2 LC-MS instrument settings and data analysis.....	23
2.4.3 Gene set enrichment analysis .....	24

2.5	Metabolomics.....	24
2.5.1	Metabolites extraction and reconstitution .....	24
2.5.2	Metabolome profiling by targeted LC-MS .....	25
2.6	Analysis of TCGA chRCC RNA-seq data .....	25
2.7	Whole exome sequencing and mitochondrial bioinformatics analysis .....	25
2.8	Measurement of the enzyme activities .....	26
2.8.1	Sample preparation for enzyme activity measurement.....	26
2.8.2	Enzymatic activity measurement of Complex I.....	26
2.8.3	Enzymatic activity measurement of Complex II .....	27
2.8.4	Enzymatic activity measurement of Complex III .....	28
2.8.5	Enzymatic activity measurement of Complex IV.....	29
2.8.6	Enzymatic activity measurement of Complex V.....	29
2.8.7	Enzymatic activity measurement of citrate synthase .....	30
2.8.8	Enzymatic activity measurement of hexosaminidase A and B .....	31
2.9	Determination of free and total GSH in plasma and urine.....	31
2.10	The ethidium bromide treated UOK276 cells as an mtDNA depletion cell model... <td>32</td>	32
2.10.1	GSH extraction in ethidium bromide treated cells.....	32
2.10.2	Relative quantification of mtDNA content by qPCR .....	32
2.10.2.1	DNA isolation.....	32
2.10.2.2	Confirmation of the $\rho^0$ status by qPCR.....	32
2.10.3	Reverse transcription-quantitative PCR (RT-qPCR).....	33
2.10.3.1	RNA and protein isolation with TRIzol reagent .....	33
2.10.3.2	Mitochondrial transcripts quantification by RT-qPCR .....	34
2.10.4	Western blot .....	35
2.11	Stable isotopic tracer to quantify the endocytosis in chRCC cells.....	36
2.12	ROS measurement method development .....	36
2.12.1	Synthesis of oxidation products derived from HE, mito-HE, and HPr <sup>+</sup> .....	37
2.12.2	Generation of MRM methods for fluorogenic probes and derived oxidation products and LC-MS/MS conditions .....	37
2.12.3	Sample preparation for fluorogenic probe stability tests and metabolite extraction .....	39
2.12.4	Metabolite extraction and determination of ROS status in a cell line .....	39
2.12.5	LC-MS/MS settings for ROS probes and oxidative products quantification ....	40
2.13	Data evaluation and Statistical Rationale .....	40

2.14 Data availability .....	41
3. Results .....	43
3.1 Proteome profiling of chRCC .....	43
3.2 Metabolome profiling of chRCC .....	48
3.3 Proteomic analysis reveals the downregulation of OXPHOS in chRCC .....	49
3.4 ChRCC display a discrepancy between the abundance of genes coding for- and the proteins involved in the respiratory chain .....	51
3.5 ChRCC are characterized by an increased level of GSH and reduced protein abundance of GSH degrading enzymes .....	53
3.6 The decrease of mtDNA content other than CI mutations may lead to a malfunction of OXPHOS in chRCC .....	55
3.7 A low mtDNA content causes the downregulation of OXHPOS subunits and elevation of GSH levels .....	57
3.8 Gluconeogenesis was completely stalled in chRCC .....	60
3.9 ChRCC feature a depletion of amino acid intermediates and pathways involved in amino acid metabolism .....	62
3.10 ChRCC cells feed on extracellular macromolecules via endocytosis .....	64
3.11 Pharmaceutical inhibition of the PLCG/IP3/Ca <sup>2+</sup> /PKC pathway suppresses the endocytosis in chRCC .....	67
3.12 The hydroethidine-based probes for ROS measurement have high autoxidation rates .....	70
3.12.1 Establishment of an MRM-based method to monitor HE, mito-HE, HPr <sup>+</sup> , and their oxidation products .....	70
3.12.2 Fluorogenic probe stability is a significant concern .....	72
3.12.3 Effects of strong ROS stimulations in cells were smaller than those for autoxidation .....	74
4. Discussion .....	77
4.1 The decreased mtDNA content is the main cause of dysregulation of OXPHOS in chRCC .....	77
4.2 ChRCC features metabolic reprogramming .....	79
4.3 ROS measurement with the hydroethidine-based probes should be interpreted with caution .....	81

5. Conclusion .....	83
References .....	85
List of figures .....	107
List of tables.....	109
Appendix.....	111
List of publications .....	113

## **Abstract**

Chromophobe renal cell carcinoma (chRCC) is derived from intercalated cells of the collecting duct system and comprises approximately 5% of all renal neoplasms. Due to its rarity, the very basic molecular characteristics of chRCC on the proteome and metabolome level still remain to be investigated. In this thesis, the proteomics and metabolomics approaches as well as mitochondrial whole-exome sequencing were employed and integrated to gain insights into the mitochondrial DNA (mtDNA) mutation landscape and to elucidate pathological alterations between chRCC and adjacent kidney tissues. In addition, these results were compared with its benign counterpart, renal oncocytoma (RO), to identify molecular differences between these two highly similar tumor subtypes for the discovery of potential diagnostic markers. An overall downregulation of the oxidative phosphorylation system (OXPHOS) in chRCC was discovered, which is a distinct feature comparing with RO. Furthermore, the main ROS scavenger glutathione was boosted in chRCC, as proteins involved in glutathione degradation were significantly decreased. Besides, the OXPHOS proteins in chRCC were identified to anti-correlate with their corresponding transcripts. The decrease of mtDNA content, rather than the complex I mutations, was the main cause of the OXPHOS downregulation in chRCC, which sequentially caused the increased glutathione level and specifically a poor correlation between the proteins and transcripts of the nuclear-but not the mtDNA-encoded OXPHOS subunits. The metabolic reprogramming including the classical Warburg effect, the down-regulation of gluconeogenesis and all pathways associated with amino acid metabolism was also identified in chRCC. The chRCC cells were found to depend on extracellular macromolecules as an amino acid source by activating endocytosis, which is probably mediated by phospholipase C gamma 2 (PLCG2). The results indicate a direct link between mtDNA depletion, downregulation of OXPHOS and subsequently an increase of glutathione in chRCC. In addition, this study provides novel insights into the rewiring of metabolic pathways in chRCC and identifies PLCG2 as an important player to overcome the nutritional shortage, which might serve as a potential therapeutic target for chRCC. The distinct regulation of the OXPHOS between chRCC and RO can be developed as a potential diagnostic marker.



## Zusammenfassung

Das chromophobe Nierenzellkarzinom (chRCC) leitet sich aus den interkalierten Zellen des Sammelkanalsystems ab und macht etwa 5% aller Nierenneoplasmen aus. Aufgrund seiner Seltenheit müssen die grundlegenden molekularen Eigenschaften von chRCC auf Proteom- und Metabolomebene noch untersucht werden. In dieser Arbeit wurden die Proteome und Metabolome sowie die mitochondrialen Sequenzen des Exoms analysiert und integriert, um Einblicke in die Mutationslandschaft der mitochondrialen DNA (mtDNA) zu gewinnen und pathologische Veränderungen zwischen chRCC und dem benachbarten gesunden Nierengewebe aufzuklären. Darüber hinaus wurden diese Ergebnisse mit ihrem gutartigen Gegenstück, dem renalen Onkozytom (RO) verglichen, um molekulare Unterschiede zwischen diesen beiden sehr ähnlichen Tumorsubtypen zu identifizieren, die potenziell auch als diagnostischer Marker verwendet werden können. Es wurde eine generelle Herunterregulierung des gesamten oxidativen Phosphorylierungssystems (OXPHOS) in chRCC gefunden, was im Vergleich zu RO ein besonderes Merkmal darstellt, da dort spezifisch nur CI erniedrigt war. Darüber hinaus wurde der Haupt-ROS-Fänger Glutathion in chRCC erhöht gefunden, da Proteine, die am Glutathionabbau beteiligt waren, signifikant verringert waren. Außerdem wurde festgestellt, dass die OXPHOS-Proteine in chRCC mit ihren entsprechenden Transkripten nicht korrelieren. Die Abnahme des mtDNA-Gehalts anstelle der CI-Mutationen war die Hauptursache für die Herunterregulierung von OXPHOS in chRCC, die sequenziell den erhöhten Glutathionspiegel und insbesondere eine schlechte Korrelation zwischen den Proteinen und Transkripten des Kern-, aber nicht des mtDNA-codierte OXPHOS-Untereinheiten verursacht hat. Die metabolische Reprogrammierung einschließlich des klassischen Warburg-Effekts, die Herunterregulierung der Glukoneogenese und aller mit dem Aminosäuremetabolismus verbundenen Stoffwechselwege wurde auch in chRCC identifiziert. Es wurde festgestellt, dass die chRCC-Zellen durch Aktivierung der Endozytose, die wahrscheinlich durch Phospholipase C gamma 2 (PLCG2) vermittelt wird, von extrazellulären Makromolekülen als Aminosäurequelle abhängen. Die Ergebnisse weisen auf einen direkten Zusammenhang zwischen der mtDNA-Depletion, der Herunterregulierung von OXPHOS und dem daraus resultierenden Anstieg von Glutathion in chRCC hin. Darüber hinaus bietet diese Studie neue Einblicke in die Änderung von Stoffwechselwegen in chRCC und identifiziert PLCG2 als wichtigen Akteur zur Überwindung des Nährstoffmangels, der als potenzielles therapeutisches Ziel für chRCC dienen könnte. Die eindeutige Regulation der OXPHOS zwischen chRCC und RO kann als potenzieller diagnostischer Marker entwickelt werden.



## 1. Introduction

### 1.1 Renal cell carcinoma

Renal cell carcinoma (RCC) represents approximately 4% of adult malignancies (Siegel, Miller et al. 2019) and was ranked as the sixth deadliest cancer worldwide in 2018 (Bray, Ferlay et al. 2018). The American Cancer Society estimated that about 73,820 new RCC cases would be diagnosed by the end of 2019 and more than 14,770 deaths would be caused by RCC this year in the USA alone (Siegel, Miller et al. 2019). RCC can be classified according to distinct morphologic and molecular genetic features and it is composed of different subtypes, such as clear cell RCC (ccRCC), papillary RCC (pRCC), chromophobe RCC (chRCC), and renal oncocytoma (RO) (Figure 1, Table 1). Many studies have been performed recently to characterize RCC to better understand its classification and subclassification and to elucidate pathway remodeling in these cancers (Sato, Yoshizato et al. 2013, Davis, Ricketts et al. 2014, Cancer Genome Atlas Research, Linehan et al. 2016). A new classification concept based on molecular clustering of chromosomes, DNA, RNA, miRNA, and protein data was proposed (Cancer Genome Atlas Research, Linehan et al. 2016, Ricketts, De Cubas et al. 2018), where the organ of origin does not fully determine the tumor type as the only factor (Hoadley, Yau et al. 2018). Instead, the cancer classification should be based on the similarity of molecular features across different tissue types, which was considered more relevant for targeting the same mutations and oncogenic signaling pathways (Hoadley, Yau et al. 2018).

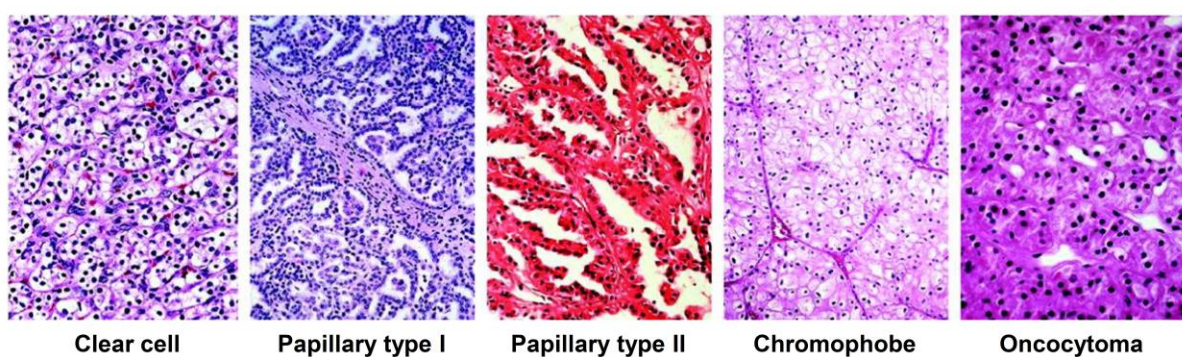


**Figure 1. Histological sections of different subtypes of renal cell carcinoma.**

Figure adapted from (Linehan, Vasselli et al. 2004).

**Table 1. Incidences and main mutations in subtypes of renal cell carcinoma**

RCC subtype	Clear cell	Papillary type I	Papillary type II	Chromophobe	Oncocytoma
Incidence	75%	5%	10%	5%	5%
Main mutations	<i>VHL</i>	<i>MET</i>	<i>FH</i>	<i>TP53, PTEN</i>	<i>mtDNA</i>

*VHL*: von Hippel Lindau; *MET*: MET proto-oncogene; *FH*: fumarate hydratase; *TP53*: tumor protein P53; *PTEN*: phosphatase and tensin homolog; *mtDNA*: mitochondrial DNA.

### 1.1.1 Clear cell renal cell carcinoma

Clear cell RCC (ccRCC) is the most prevalent subtype and accounts for about 75% of all RCCs (Table 1) (Moch, Cubilla et al. 2016). It is an aggressive cancer type that originates from the proximal convoluted tubule, with a recurrence rate of up to 40% after the initial treatment of a localized tumor (Chin, Lam et al. 2006). In its metastatic form, it is associated with a high mortality rate (Motzer, Bacik et al. 2004). CcRCC cells have, in general, a clear cytoplasm, (which helped coin the name “clear cell”) that is circled by an easily distinguishable cell membrane and uniform round nuclei (Figure 1) (Delahunt, Srigley et al. 2014). About 90% of all ccRCC cases carry mutations in the von Hippel-Lindau (*VHL*) tumor suppressor gene (Cancer Genome Atlas Research 2013, Sato, Yoshizato et al. 2013), which was originally identified in a hereditary disease called VHL syndrome (Latif, Tory et al. 1993). The *VHL* protein is a target recruitment subunit in an E3 ubiquitin ligase complex and recruits the hydroxylated hypoxia-inducible factor (HIF) under normoxic conditions for subsequent proteasomal degradation. Thereby, *VHL* can repress the transcription of more than 100 target genes through interaction with HIF1 $\alpha$  and HIF1AN, which plays a vital role in forming the phenotype of ccRCC (Jaakkola, Mole et al. 2001). HIF1 $\alpha$  is a master transcription factor that contributes substantially to the regulation of gene expression that is dependent on oxygen levels. Under normoxic conditions, *VHL* interacts with HIF1 $\alpha$  and hydroxylates the proline residues in the oxygen-dependent degradation (ODD) domains of HIF1 $\alpha$  by recruiting members of the Egl-nine homolog (EGLN) family (Ivan, Kondo et al. 2001, Jaakkola, Mole et al. 2001, Gossage, Eisen et al. 2015). With hypoxia or loss of function of *VHL*, these proline residues cannot be hydroxylated, which stabilizes HIF1 $\alpha$ . Subsequently, HIF1 $\alpha$  forms a HIF1 $\alpha$ -HIF1 $\beta$  heterodimer, and this dimer translocates into the nucleus to enhance the transcription of HIF target genes, which are associated with crucial oncogenic pathways, including glucose uptake, glycolysis (e.g., glucose transporter type 1, *GLUT1*), cell proliferation (e.g., epidermal growth factor receptor, *EGFR*), and angiogenesis (vascular endothelial growth factor, *VEGF*) (Gossage, Eisen et al. 2015,

## Introduction

Riazalhosseini and Lathrop 2016, Posadas, Limvorasak et al. 2017, Wettersten, Aboud et al. 2017).

Furthermore, the gluconeogenic enzyme fructose 1,6-bisphosphatase 1 (FBP1) has been found to be decreased in over 600 ccRCC cases and the decreased expression of FBP1 is associated with poor disease prognosis. FBP1 has two distinct functions, antagonizing the glycolytic flux and inhibiting the nuclear function of HIF $\alpha$  (Li, Qiu et al. 2014), which can explain its ubiquitous loss in ccRCC (Li, Qiu et al. 2014). Besides FBP1, the whole gluconeogenesis pathway has been shown to be severely diminished in ccRCC at the transcriptome (Li, Qiu et al. 2014) and proteome level (Guo, Kouvonen et al. 2015). This stimulates the metabolic switch by increasing glycolytic target genes (Li, Qiu et al. 2014), which is reflected by the metabolomic analysis of ccRCC, where metabolites in the glycolysis pathway show over two-fold increases in abundance compared to the normal kidney (Hakimi, Reznik et al. 2016).

### 1.1.2 Papillary renal cell carcinoma

Papillary RCC (pRCC) represents about 15% of all RCCs (Table 1) and derives from the proximal convoluted tubule, similar to ccRCC (Moch, Cubilla et al. 2016). It is a less aggressive subtype compared to ccRCC and has a high five-year survival rate of 80% to 85% (Steffens, Janssen et al. 2012). The term “papillary” describes the papilla-like protuberances in most of the tumors. It can be further subdivided into type I and type II tumors based on morphological features (Figure 1). Type I pRCC is more common and shows small fibrovascular papillae that are covered by a single layer of small cuboidal cells with scant pale cytoplasm and usually grows slowly (Delahunt and Eble 1997). In contrast, type II pRCC consists of papillae, is lined by large columnar pseudostratified cells with eosinophilic cytoplasm, and is often more aggressive (Delahunt and Eble 1997, Pignot, Elie et al. 2007). Type I and type II pRCC have also been shown to be clinically and biologically distinct. Type I is frequently associated with the alterations in the MET pathway (Cancer Genome Atlas Research, Linehan et al. 2016, Pal, Ali et al. 2018). The proto-oncogene c-Met (MET) protein, a transmembrane receptor tyrosine kinase, can bind to its ligand hepatocyte growth factor (HGF) and activate several downstream intracellular pathways, including focal adhesion kinase (FAK), RAS/RAF/MEK/ERK, and PI3K/AKT (Fay, Signoretti et al. 2014). The frequently activating mutations and amplification of *MET* in type I pRCC enable the activation of MET/HGF signaling and its above-mentioned downstream pathways

to promote cancer cell proliferation, angiogenesis, and malignant transformation (Fay, Signoretti et al. 2014).

Frequent mutations in type II pRCC include *CDKN2A* silencing, *SETD2* mutations, and *TFE3* fusions. Type II tumors are characterized by increased expression of the nuclear factor erythroid 2-related factor 2 (NRF2)–antioxidant response element (ARE) pathway (Cancer Genome Atlas Research, Linehan et al. 2016). The NRF2–ARE pathway is a major regulator of cellular redox balance, and its activation under oxidative stress favors cell survival. Furthermore, fumarate hydratase (*FH*) mutations are also frequently found in type II pRCC (Tomlinson, Alam et al. 2002, Li, Shuch et al. 2017). The *FH* gene encodes a TCA cycle enzyme that catalyzes the hydration of fumarate to malate, and its deficiency causes fumarate and succinate accumulation (Pollard, Briere et al. 2005, Sullivan, Martinez-Garcia et al. 2013). Accumulated fumarate and succinate are believed to be able to suppress the hydroxylation of the proline residues in the ODD domain of HIF $\alpha$ , and thus *FH* mutations in type II pRCC also cause the stabilization of HIF $\alpha$ , similarly to ccRCC (Pollard, Briere et al. 2005, Sullivan, Martinez-Garcia et al. 2013). Some genes (such as *CDKN2A/B* and *TERT*) where mutations can be found in both types (Pal, Ali et al. 2018) play a pivotal role as tumor suppressors by regulating the cell cycle. Mutations of the above-mentioned genes and activation of the onco-pathways are the main driver mutations in the progression of pRCC.

### 1.1.3 Chromophobe renal cell carcinoma

Chromophobe RCC (chRCC) accounts for approximately 5% of all RCCs (Table 1) (Moch, Cubilla et al. 2016), which is thought to originate from the cortical collecting duct, and was first reported in 1985 (Thoenes, Storkel et al. 1985). Different morphological and ultrastructural features of the cytoplasm lead to the identification of the classical chromophobe and the eosinophilic variant. The cells of the classical type usually have abundant clear cytoplasm and a perinuclear halo caused by cytoplasmic organelles being pushed away from the center to form a rim along the cell membrane (Figure 1) (Yusenko 2010). The eosinophilic type has, in general, smaller cells with an inconstant level of cytoplasmic organelles in the periphery. Both cell types frequently coexist in chRCC tumors, usually with one cell type predominating (Yusenko 2010). One of the most characteristic genetic features of chRCC is the monosomy of chromosomes 1, 2, 6, 10, 13, 17, and often 21 (Brunelli, Eble et al. 2005, Haake, Weyandt et al. 2016, Casuscelli, Weinhold et al. 2017, Xiao, Clima et al. 2019). The most commonly mutated genes in chRCC are *TP53* (32%), *PTEN* (20%), and gene fusions involving the *TERT* promoter (Davis, Ricketts et al. 2014,

## Introduction

Haake, Weyandt et al. 2016). Mutations in these tumor suppressors combined with the deletion of one of their chromosomes lead to a complete loss of function. Further mutations with a lower frequency were observed in *MTOR*, *NRAS*, *TSC1*, and *TSC2*, indicating that the genomic targeting of the mTOR pathway occurred in 23% of all chRCC (Davis, Ricketts et al. 2014). Hence, the anticancer functions of TP53 in apoptosis, genomic stability, and the inhibition of angiogenesis and the role of PTEN in the intracellular signaling pathway PI3K/AKT/mTOR are both disrupted and can thus be regarded as major driving events in these chRCC cases. However, no clear driver mutation was discovered in over 50% of the chRCC cases (Davis, Ricketts et al. 2014, Durinck, Stawiski et al. 2015).

ChRCC was reported to have significantly lower microvessel density compared to the other two RCC subtypes, ccRCC and pRCC (Jinzaki, Tanimoto et al. 2000). This is further illustrated by the clinical value of <sup>18</sup>F-fluorodeoxyglucose-positron emission tomography/computed tomography (FDG-PET/CT), which uses a fluorine<sup>18</sup> labeled glucose analog to image and stage tumors, FDG-PET/CT can be used to access the glucose uptake of tumor *in vivo*. Among the three RCC types, chRCC has a significantly lower level of glucose uptake (Figure 2) (Nakajima, Nozaki et al. 2017). Hence, chRCC seems to be poorly supported by the blood vessel. As reprogrammed metabolism is a hallmark of cancer (Hanahan and Weinberg 2011), how chRCC modifies its fundamental metabolism and adapts to the nutrient-poor environment still remains unknown. Due to the comprehensive investigation and research focused on ccRCC, extensive metabolic alterations have been identified in ccRCC and it has been defined as a metabolic disease (Hakimi, Reznik et al. 2016, Linehan, Schmidt et al. 2019). On the contrary, even the very basic metabolic characteristics of chRCC remain to be investigated.

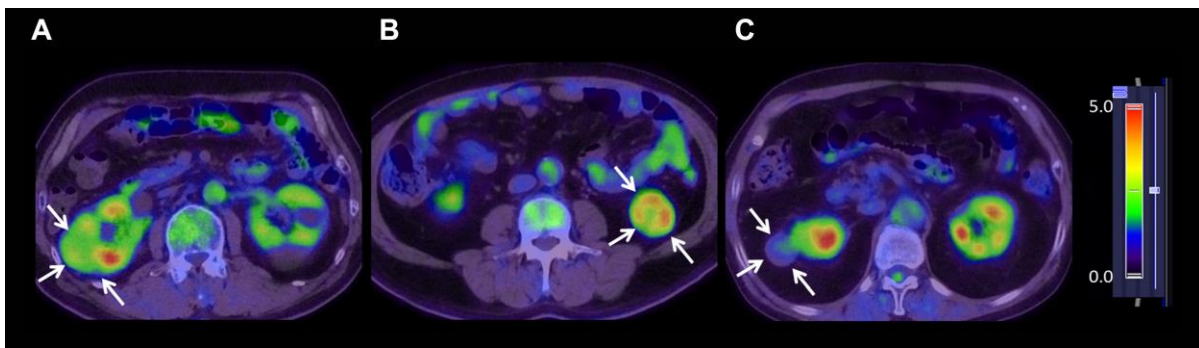


**Figure 2. FDG-PET/CT of ccRCC, pRCC, and chRCC.**

Axial PET/CT images show moderate FDG accumulation in (A: arrow) ccRCC and (B: arrow) pRCC; no FDG accumulation was observed in (C) chRCC PET/CT images. Figure adapted from (Nakajima, Nozaki et al. 2017).

#### **1.1.4 Renal oncocytoma**

Renal oncocytoma (RO) was firstly reported by Zippel in 1942 (Zippel 1941) and is classified as benign renal epithelial neoplasm (Lopez-Beltran, Scarpelli et al. 2006, Lopez-Beltran, Carrasco et al. 2009). It is derived from intercalated cells of the collecting duct system and comprises only a small subset (around 5%) of all renal neoplasms (Table 1). Usually, RO can be cured by nephrectomy. RO typically consists of uniform round / polygonal cells with abundant, intensely eosinophilic and granular cytoplasm, and with uniformly small, round and central nuclei with evenly dispersed chromatin (Figure 1). The two hallmarks of RO are the large amount of mitochondria in the cytoplasm (Tickoo, Lee et al. 2000) and the highly diminished or complete loss of complex I (CI) enzyme activity within the electron transport chain (Simonnet, Demont et al. 2003, Mayr, Meierhofer et al. 2008). The deficiency of CI is mainly due to mutations in mitochondrial DNA (mtDNA), particularly, but not exclusively, in CI genes (Gasparre, Hervouet et al. 2008, Mayr, Meierhofer et al. 2008). Most mtDNA mutations detected in RO are well above the threshold for a pathogenic phenotypic effect due to high heteroplasmic load. The mtDNA mutations above the heteroplasmy threshold appear to reduce tumor growth because of their impaired effect on respiratory complex assembly (Gasparre, Romeo et al. 2011, Ju, Alexandrov et al. 2014). This seems to be the main cause of the indolent, low-proliferating, non-invasive behavior of RO.

## **1.2 Similarities and differences between chRCC and RO**

ChRCC is considered to be the malignant counterpart of RO (Joshi, Tolkunov et al. 2015), as they feature many molecular and histological similarities. Firstly, both of the two tumor types are considered to be derived from the same origin, as discussed above. Secondary, they both show mtDNA mutations and abnormal mitochondrial pathology. RO has above heteroplasmy threshold mtDNA mutations, mainly in CI genes, which leads to its benign feature (Gasparre, Romeo et al. 2011, Ju, Alexandrov et al. 2014). ChRCC, on the other hand, also has been observed to possess mtDNA mutations in CI genes with a frequency of 13% (>50% heteroplasmy rate) (Davis, Ricketts et al. 2014). A pathway analysis of the transcriptome data showed that cases with mutations in *MT-ND5* versus no mutations in this gene in chRCC (almost all from the eosinophilic type) lead to an enrichment of the Gene Ontology term “mitochondrion” (Davis, Ricketts et al. 2014, Ricketts, De Cubas et al. 2018). The eosinophilic chRCC type was even reported to have an increased amount of mitochondria, a typical histological feature of RO (Tickoo, Lee et al. 2000). By analyzing the genomic and transcriptomic signature of RO and chRCC, Joshi et.al found a subset of RO,

## Introduction

which is hypodiploid with loss of chromosome 1, X or Y, and/or 14 and 21 and has a male predominance. This subset of RO might be the precursor of the eosinophilic chRCC (Joshi, Tolkunov et al. 2015), as the eosinophilic chRCC also has a sex bias and a similar pattern of chromosome loss of 1, X, or Y, but with further losses including 2, 6, 10, 13 and 17 (Davis, Ricketts et al. 2014, Joshi, Tolkunov et al. 2015). What's more, a rare cancer susceptibility syndrome, called Birt-Hogg-Dubé syndrome (BHDS), caused by germline mutations in the *FLCN* gene (codes for the folliculin protein), is characterized mainly by fibrofolliculomas, lung cysts, and renal tumors (Figure 3) (Benusiglio, Giraud et al. 2014, Baba, Schmidt et al. 2017). Interestingly, the renal tumors in BHDS patients show multiple histological types, predominantly (70%) chRCC, RO or hybrid type composed of oncocytic and chromophobe elements, very few (9%) even were clear cell type (Hes, Petersson et al. 2013, Benusiglio, Giraud et al. 2014, Baba, Schmidt et al. 2017).

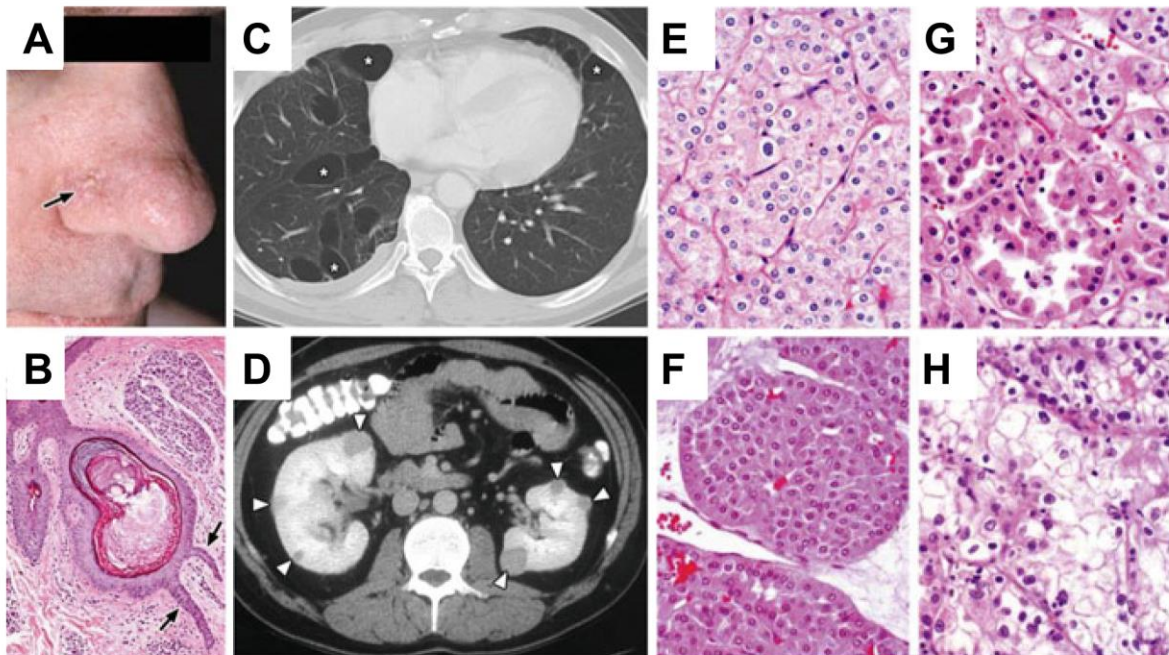


**Figure 3. Clinical manifestations of Birt-Hogg-Dubé syndrome.**

(A) Fibrofolliculomas on the face (arrow). (B) Histology of fibrofolliculoma showing epithelial strands with thick connective tissue stroma (arrows). (C) CT image indicating multiple lung cysts. (D) CT image of bilateral multifocal renal tumors (arrowheads). BHDS-associated renal tumors show multiple histological types: chromophobe RCC (E), oncocytoma (F), hybrid oncocytic tumor (G), and ccRCC (H). Figure from (Pavlovich, Grubb et al. 2005).

### 1.3 Glutathione salvage pathway in chRCC

One common characteristic of cancer is the ability to balance the increased level of oxidative stress with a high level of antioxidants. Glutathione (GSH), a tripeptide thiol antioxidant composed of the amino acids glutamic acid, cysteine, and glycine (Meister 1988), is the main reactive oxygen species (ROS) scavenger in cells. GSH is highly reactive and exists in both a reduced (GSH) and oxidized disulfide (GSSG) form (Kaplowitz, Aw et al. 1985). The predominant form is in the reduced state, which is the most abundant low molecular weight thiol in the cells, ranging from 0.5 to 10 mM in most cell types, whereas extracellular GSH exists in concentrations lower by magnitudes (Meister and Anderson 1983). The de novo biosynthesis of GSH involves two ATP-dependent enzymatic reactions: The first step is catalyzed by glutamate-cysteine ligase (GCL), which ligates the amino group of cysteine to the  $\gamma$ -carboxylate of glutamic acid to form the dipeptide  $\gamma$ -glutamyl cysteine. The second reaction involves GSH synthetase (GSS), which catalyzes a combination of the cysteinyl carboxylate of the dipeptide and the amino group of glycine to synthesize GSH (Lu 2009) (outlined in Figure 4).

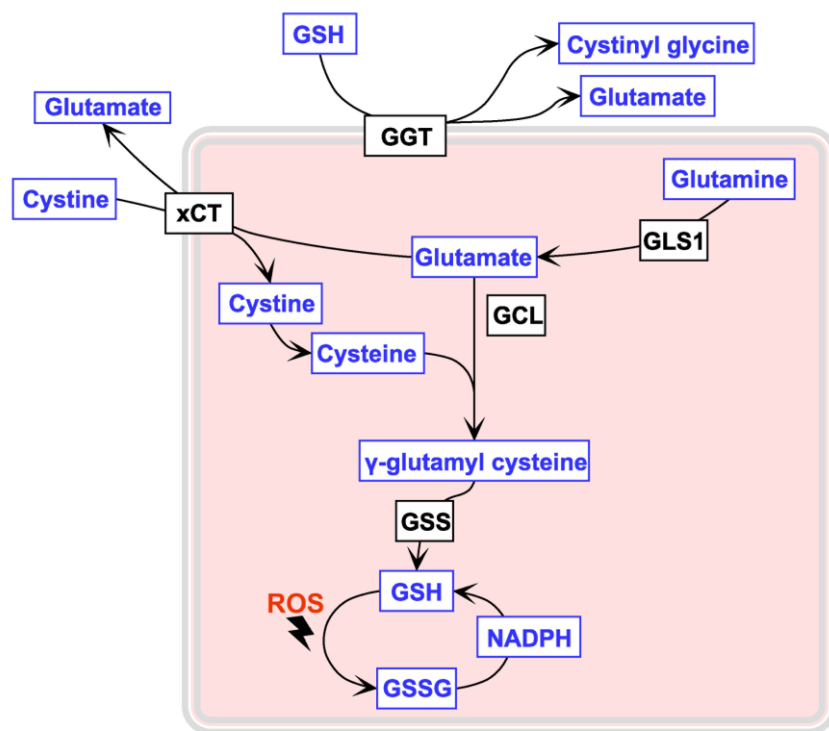


**Figure 4. Schematic overview of glutathione (GSH) metabolism.**

Color codes are defined as follows: black = enzymes or transporters; blue = metabolites. GGT:  $\gamma$ -glutamyl transferase; xCT: solute carrier family 7 member 11, a cystine-glutamate antiporter; GLS1:

## Introduction

glutaminase 1; GCL: glutamate-cysteine ligase; GSS: glutathione synthetase. GSSG: glutathione oxidized form; ROS: reactive oxygen species.

$\gamma$ -glutamyl transferases (GGTs) are membrane-bound, N-terminal nucleophile hydrolases that catalyze the breakdown of extracellular GSH and transfer the  $\gamma$ -glutamyl group from GSH to produce the constituents glutamate and cysteine, which can be further used for intracellular GSH synthesis (Figure 4) (Terzyan, Burgett et al. 2015). Increased serum GGT was reported to be a sensitive marker for metastatic ccRCC (Simic, Dragicevic et al. 2007), because high GGT level positively correlated with advanced stages, higher grades, and the presence of tumor necrosis, and it was further associated with worse survival rates in ccRCC patients (Hofbauer, Stangl et al. 2014). One member of the membrane transpeptidase family GGT is  $\gamma$ -glutamyl transferase 1 (GGT1), which can remove and transfer the  $\gamma$ -glutamyl moiety from extracellular GSH, GSSG, or even GSH conjugates to an amino acid acceptor, known as the GSH salvage pathway. This degradation of extracellular GSH species fuels the cytoplasm of cells to maintain intracellular GSH levels (Terzyan, Burgett et al. 2015). Recent metabolomic profiling studies have identified significantly increased amounts of GSH, GSSG, and its precursor  $\gamma$ -glutamyl cysteine in chRCC compared to normal kidney tissue (Priolo, Khabibullin et al. 2018, Xiao, Clima et al. 2019). Unlike in ccRCC, significantly lower expression of GGT1 has been reported in chRCC (Priolo, Khabibullin et al. 2018, Xiao, Clima et al. 2019). The specific loss of GGT1 in chRCC leads to an increased sensitivity to oxidative stress, mitochondrial damage, and reprogramming of glutamine and glucose metabolism (Priolo, Khabibullin et al. 2018). Interestingly, RO was found to have a similar increase in GSH moieties and decreased levels of GGT1 relative to normal kidney tissues (Kurschner, Zhang et al. 2017).

### 1.4 Glutathione and reactive oxygen species

Increased ROS levels, including the superoxide anion, hydrogen peroxide, and hydroxyl radical, have been reported in many different cancer types. ROS can be either generated by genetic alterations and endogenous oxygen metabolism or by exogenous sources, such as UV light and radiation. ROS were long thought to be only damaging byproducts of the cellular metabolism that can negatively affect DNA, lipids, and proteins (Kim, Kim et al. 2016). However, more recent studies have highlighted the important role of ROS in cell signaling, homeostasis, metabolism, and apoptosis (Kim, Kim et al. 2016).

GSH is the main ROS scavenger in cells. Besides the classical role of GSH acting as a ROS scavenger by being prey for radicals, GSH has several additional functions, including but not

limited to providing a cysteine reservoir (Cho, Johnson et al. 1984), being involved in the maturation of iron-sulfur proteins (Sipos, Lange et al. 2002), detoxifying xenobiotics (Awasthi, Misra et al. 1983), regulating protein bioactivity by S-glutathionylation (Duan, Kodali et al. 2016, Zhang, Liu et al. 2017), and regulating redox signaling (Ren, Zou et al. 2017). In cancer, GSH plays the role of a double-edged sword in its initiation and progression. Moderate ROS levels are widely recognized to trigger cancer initiation and progression by inducing mutations and promoting genome instability, eventually activating oncogenic signaling pathways that promote cell survival, proliferation, and stress resistance (Hussain, Hofseth et al. 2003). On the contrary, massive ROS accumulations can also limit cancer growth by causing severe oxidative damage of biomolecules, which finally can lead to cell death (Hatem, El Banna et al. 2017). As a consequence, cancer cells are required to deliberately balance the levels of ROS and antioxidants (mainly GSH) to maintain redox homeostasis, which sustains viability and growth. For many years, one of the most obvious therapeutic strategies to overcome new balanced redox homeostasis in renal cell carcinoma (RCC) was to fight elevated ROS levels with the supplementation of antioxidants such as vitamins to actively force the tumor into apoptosis. Many clinical trials were initiated, and the outcomes showed mixed results, including worse survival rates upon supplementation with ROS inhibitors (Thyagarajan and Sahu 2018).

## 1.5 Hydroethidine based probes for ROS measurement

As GSH is tightly connected to ROS status, and the rewired metabolism of GSH in RCC has been proposed as a hallmark of RCC and can be exploited as a potential treatment strategy against RCC (Hakimi, Reznik et al. 2016, Kurschner, Zhang et al. 2017, Ahmad, Paffrath et al. 2019, Xiao, Clima et al. 2019, Xiao and Meierhofer 2019). Thus, the ability to assess ROS status is of great value, many different methods have been established that allow the direct or indirect measurement of redox states, the advantages and disadvantages of these methods were reviewed recently (Dikalov and Harrison 2014). One aim of this thesis was to develop a robust, rapid and quantitative LC-MS/MS-based method to measure  $O_2^-$  levels in cells.

The most commonly used fluorogenic probes for  $O_2^-$  detection, and the current “gold standard”, are hydroethidine (HE; or dihydroethidium) and mitochondrial-targeted hydroethidine (mito-HE, mitoSOX red) for intracellular and mitochondrial  $O_2^-$  detection, respectively (Zielonka, Hardy et al. 2009, Kalyanaraman, Dranka et al. 2014). Moreover, membrane-impermeable hydropropidone (HPr<sup>+</sup>) that can detect extracellular  $O_2^-$  was

## Introduction

recently developed (Michalski, Zielonka et al. 2013). These three structurally analogous fluorogenic probes react with  $O_2^-$  in a very similar way, wherein  $O_2^-$ -specific hydroxylated products (2-OH-E<sup>+</sup>, 2-OH-mito-E<sup>2+</sup>, and 2-OH-Pr<sup>2+</sup>) are formed as the main products (Figure 5). However, many other oxidants are present in cells, including redox metal ions, heme proteins, and one- or two-electron oxidants, which can give rise to fluorescent ethidium and analogs (E<sup>+</sup>, mito-E<sup>2+</sup>, and Pr<sup>2+</sup>) as well as weakly or non-fluorescent dimeric products (di-E<sup>+</sup>, di-mito-E<sup>2+</sup>, and di-Pr<sup>2+</sup>; Figure 5) (Kalyanaraman, Dranka et al. 2014). The use of fluorescence microscopy or other fluorescence-based methods with these probes should be avoided, considering that the fluorescent characteristics of  $O_2^-$ -derived marker products and other non-specific oxidized fluorescent products that form from these probes can have spectral overlap (Kalyanaraman, Dranka et al. 2014).

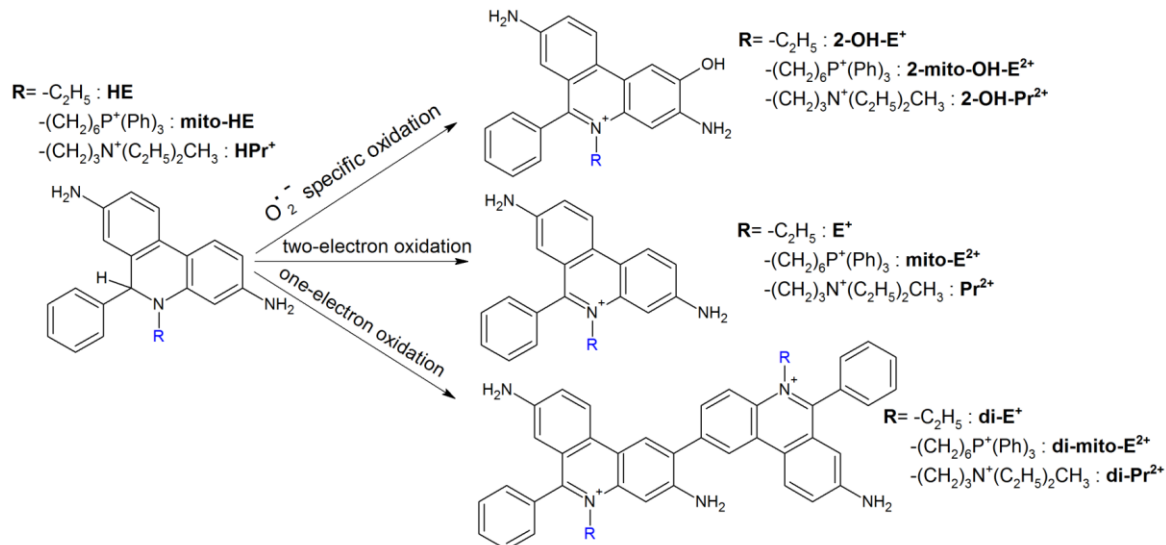


**Figure 5. Products formed from HE, mito-HE, and HPr+.**

Figure adapted from (Kalyanaraman, Hardy et al. 2017).

## 1.6 Mass spectrometry based metabolomics and proteomics

### 1.6.1 Mass spectrometry

Mass spectrometry (MS) is an analytical technique that can identify and quantify the chemicals by ionizing them into ions, sorting the ions according to their mass-to-charge ratio ( $m/z$ ), and then measuring the number of ions. Accordingly, a basic mass spectrometer usually consists of at least three parts: an ion source to ionize the chemical species, a mass analyzer to sort the ions based on their  $m/z$ , and a detector to measure the abundance of ions. Nowadays, a mass spectrometry instrument usually contains two or even more mass

analyzers to increase its ability to analyze chemical samples. Due to the differences in the mass analyzers, there are many different types of mass spectrometers. Here, triple quadrupole mass spectrometer (TQMS) and Orbitrap mass spectrometer (OMS), the two types of mass spectrometers used in this thesis, are introduced in more details.

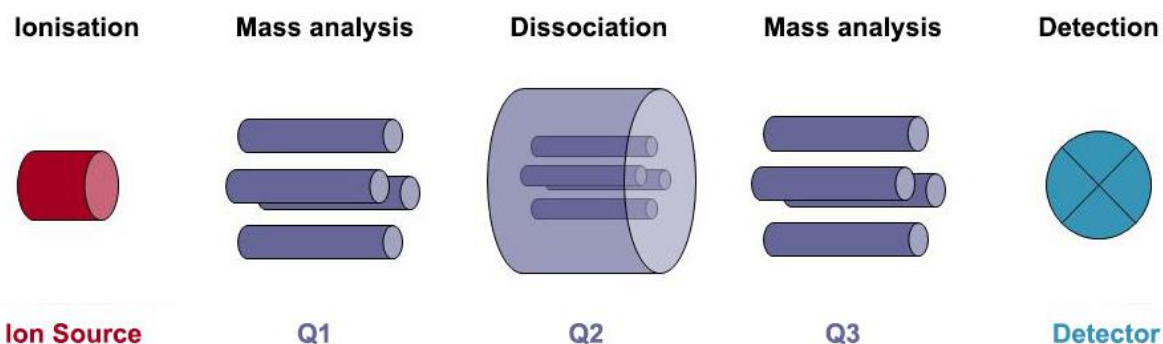


**Figure 6. Schematic representation of the triple quadrupole mass spectrometer.**

A typical triple quadrupole mass spectrometer (TQMS) consists of an ion source to ionize the chemicals, three quadrupoles to act as mass filters (Q1 and Q3) and a collision compartment (Q2), and a detector to determine the number of ions. Figure adapted from [https://www.biologie.hu-berlin.de/de/gruppenseiten/oekologie/meth/massspec/mass\\_sp](https://www.biologie.hu-berlin.de/de/gruppenseiten/oekologie/meth/massspec/mass_sp)

TQMS was firstly developed and constructed by James D. Morrison in 1974 at La Trobe University (Morrison 1991). It is a tandem mass spectrometer composed of three quadrupoles in which the first and third quadrupoles (Q1 and Q3) serve as mass filters and the second (Q2) acts as a collision cell for collision-induced dissociation (CID) (Figure 6). Both Q1 and Q3 contains four parallel, cylindrical metal rods and are controlled by direct current (DC) and radio-frequency (RF) potentials to select particular ions to pass through them (Dass 2006). The collision cell, Q2, however, can be quadrupole or replaced by hexapole or octopole in some instruments to improve efficiency (Dass 2006) and it is only controlled by RF potential to fragment ions but allows all ions to pass through (Dass 2006). Depending on the purpose of analysis, the TQMS can have at least four different scan modes (de Hoffmann 1996, Dass 2006, Domon and Aebersold 2006): Product ion scanning, for identifying ion transitions for quantification (Figure 7A). Precursor ion scanning, to select the ions with a particular functional group that fragmented in Q2 (Figure 7B). Neutral loss scanning, for identifying all the ions with the loss of a given neutral fragment (e.g. H<sub>2</sub>O)(Figure 7C). Multiple reaction monitoring (MRM) mode or selected reaction monitoring (SRM), to allow a distinct fragment ion from a certain parent ion to be detected (Figure 7D), MRM mode is used very widely in quantification with MS as it can quantify multiple ions by

## Introduction

setting Q1 and Q3 to more than a single mass (ion pairs or transition). Overall, TQMS is very robust, cheap, and simple to use, but it only offer low mass resolution and accuracy in its application.

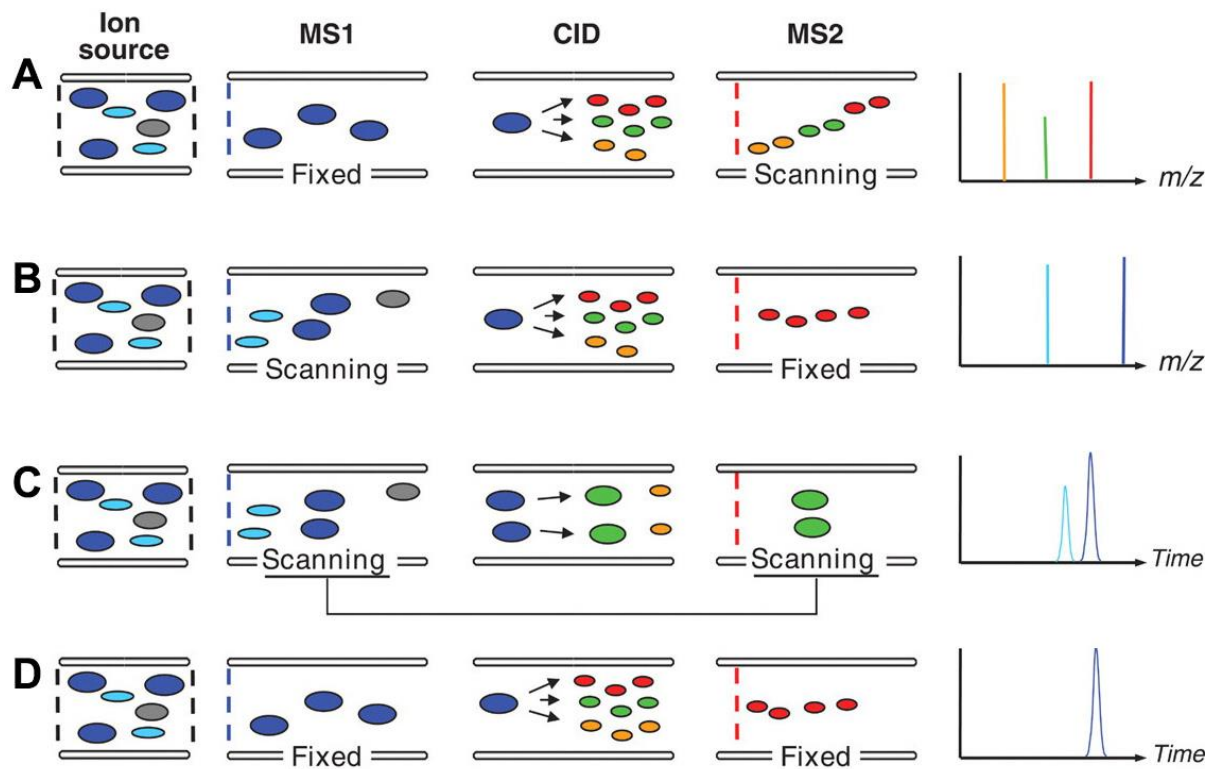


**Figure 7. Different scan modes of triple quadrupole mass spectrometer.**

The four different scan modes of triple quadrupole mass spectrometer: (A) Product ion scanning; (B) Precursor ion scanning; (C) Neutral loss scanning; (D) Multiple reaction monitoring (MRM) mode or selected reaction monitoring (SRM). Figure adapted from (Domon and Aebersold 2006).

Similar to TQMS, the OMS is also a tandem mass spectrometer system (Figure 8), but instead of triple quadrupole, it usually contains only two quadrupoles (can be hexapoles or octopoles) acting as the mass filter and collision cell, and another key component, the Orbitrap. The Orbitrap is an ion trap mass analyzer consisting of two outer barrel-like electrodes and a central spindle-like electrode, enabling it to act as both an analyzer and detector (Figure 8). The first Orbitrap was invented by Makarov at the end of the 1990s (Makarov 2000). After many years of technical improvement, Thermo Fisher Scientific introduced the first commercial Orbitrap analyzer as the core component of a hybrid LTQ OMS in 2005 (Makarov, Denisov et al. 2006, Makarov, Denisov et al. 2006). In the Orbitrap, the ions are trapped and detected by their image current, and then the detected image current is converted to a mass spectrum using the Fourier transform of the frequency signal

(Makarov 2000). The OMS has the advantage of high sensitivity and much higher resolution compare to TQMS due to the fact that each ion is trapped in the orbitrap and can be “counted” more than once (Makarov, Denisov et al. 2006, Makarov, Denisov et al. 2006).

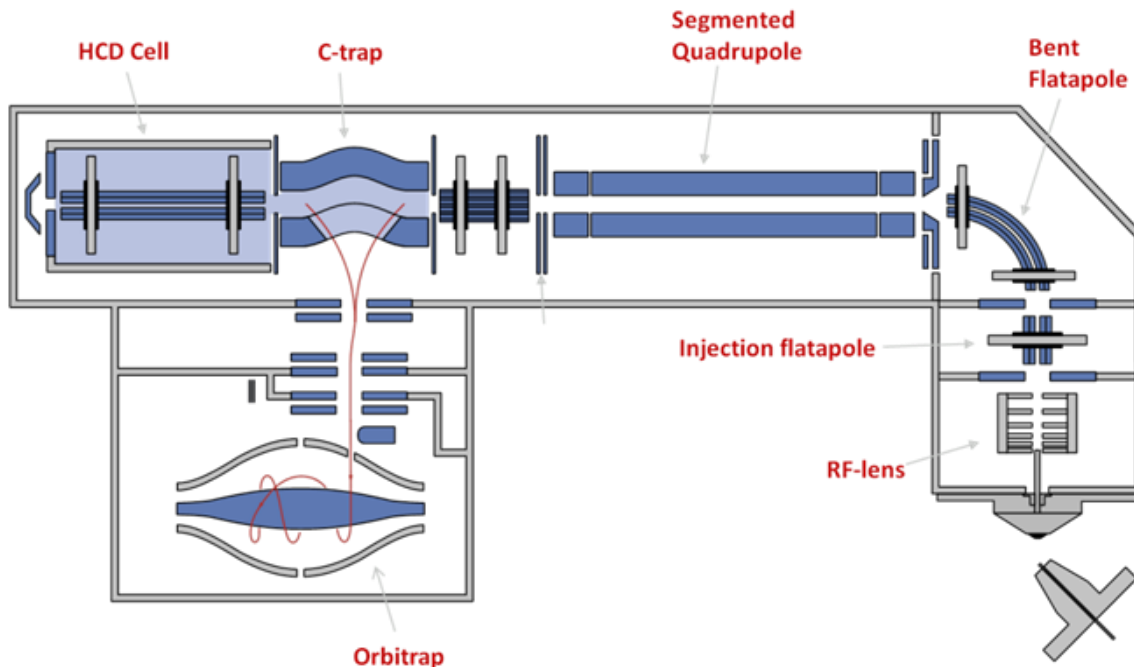


**Figure 8. The schematic of an orbitrap mass spectrometer.**

A Q-Exactive Plus Orbitrap mass spectrometer from Thermo Fisher Scientific. The ionized chemicals in the ion source are injected into the Orbitrap mass spectrometer, first go through the RF-lens, injection flatapole and bent flatapole to reach the segmented quadrupole, here, the ions can be selected. The (selected) ions are then injected to C-trap, from here, the ions can either be directly transferred into the Orbitrap for analysis (MS1 scan mode), or be further fragmented in the higher-energy collisional dissociation (HCD) cell and transferred back through the C-trap to the Orbitrap for analysis (MS2 scan mode). Figure from <https://planetorbitrap.com/q-exactive-plus>

### 1.6.2 Metabolomics

Metabolites are the small molecule substrates, which are educts, intermediates, and end products of metabolism, they have a multitude of functions, including energy conversion, signaling, stimulatory and inhibitory effects on the catalytic activity of enzymes, and epigenetic influence (Lu and Thompson 2012, Wollen and Thompson 2012). Metabolomics is defined as the systematic study of all chemical processes concerning metabolites by measuring the complete set of metabolites present within a biological system, namely, a cell, tissue, organ or organism, providing characteristic chemical fingerprints and revealing the functional readout of the physiological state of the studied system. The strategies of

## Introduction

metabolomics can be divided into two distinct approaches, untargeted and targeted metabolomics, both have their own inherent advantages and disadvantages. Untargeted metabolomics studies are usually employed to generate hypotheses, focus on acquiring data with information as many as possible, the raw data contain all ions within a certain mass range, then with software to annotate known and novel metabolites and review both known and unknown metabolic changes (Schrimepe-Rutledge, Codreanu et al. 2016). Because of the comprehensive and extensive mass spectrum information it contains, untargeted metabolomics raw data requires annotation by using *in silico* libraries or experimental investigation and subsequent identification using analytical chemistry (Roberts, Souza et al. 2012). It can be very challenging for using untargeted metabolomics approaches due to the time-consuming procedure of massive raw data generation and processing, difficulties in identifying unknown metabolites, and the bias towards detection of the high-abundance metabolites (Roberts, Souza et al. 2012). On the contrary, targeted metabolomics approaches are usually aimed at validating hypothesis by identifying and quantifying a limited number of known metabolites, which acquire raw data based on the preset ion mass information (usually MRM scanning mode) of known metabolites (Schrimepe-Rutledge, Codreanu et al. 2016). This approach is much faster, simpler and more robust compared to the untargeted metabolomics, as it doesn't need the comprehensive annotation of metabolites, the sample preparation can be optimized to reduce the amount of high-abundance molecules to avoid bias (Roberts, Souza et al. 2012). In addition, targeted metabolomics can be undertaken in a quantitative or semi-quantitative manner, whereas the untargeted metabolomics can only be semi-quantitative (Roberts, Souza et al. 2012, Schrimpe-Rutledge, Codreanu et al. 2016).

### 1.6.3 Proteomics

Similar to the definition of metabolomics, proteomics is the large-scale study of proteins in a biological system (Anderson and Anderson 1998). The word “proteome”, coined by Wilkins, *et al.* in 1994 (Wasinger, Cordwell et al. 1995), was used in his PhD thesis to describe the entire complement of proteins expressed by a genome, cell, tissue or organism. There are many methods to study the proteome, such as protein chips, reversed-phase protein microarrays, two-dimensional gel electrophoresis, and mass spectrometry based proteomics. Over the past decades, liquid chromatography coupled with mass spectrometry (LC-MS) has gained popularity due to its versatile ability to handle the complexities associated with the proteome (Aebersold and Mann 2003, Aebersold and Mann 2016).

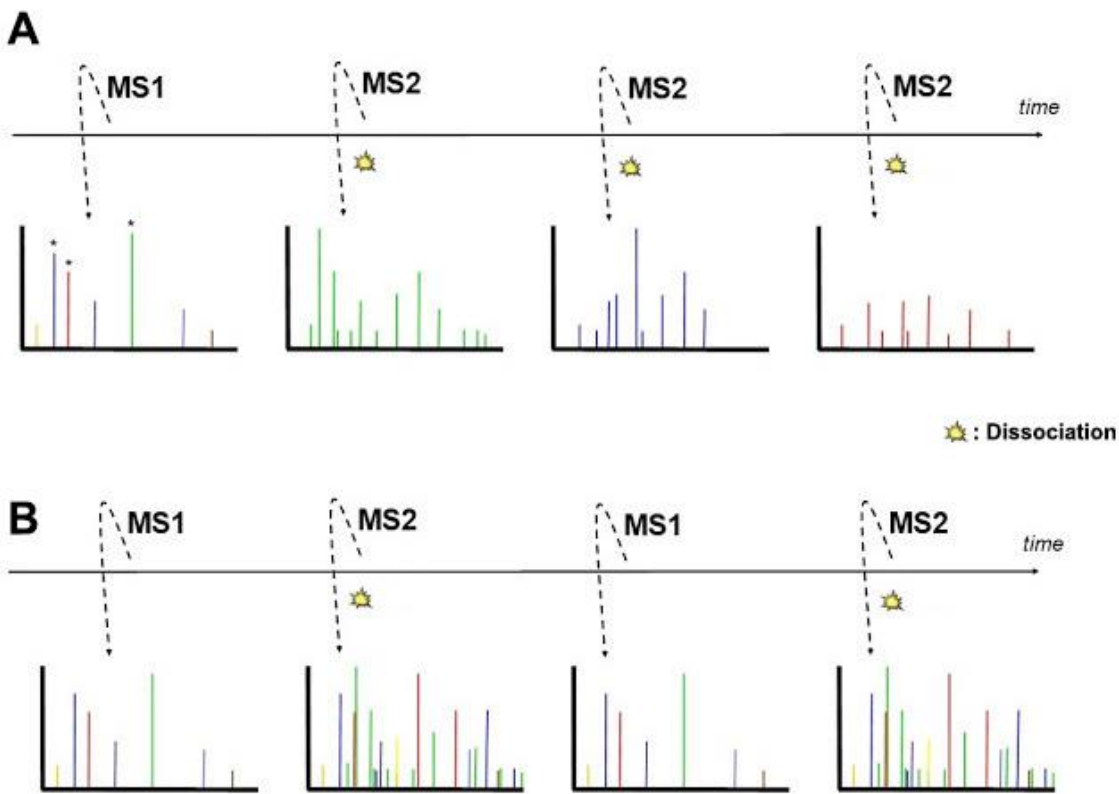


**Figure 9. An illustration of data-dependent and data-independent modes of acquisition.**

Two data acquisition strategies of mass spectrometry based proteomics: (A) data-dependent acquisition mode, (B) data-independent acquisition mode. Figure adapted from <http://ajscientific.blogspot.com/2018/04/data-dependent-versus-data-independent.html>

Two general strategies of MS-based proteomics experiments are data-dependent acquisition (DDA) and data-independent acquisition (DIA) methods (Figure 9). The DDA strategy, which has been very widely used for the last 20 years, is able to provide broad detection and quantification of thousands of proteins across various biological samples (Mann, Hendrickson et al. 2001, Bateman, Goulding et al. 2014). In recent years, the DIA strategy has gained more attention with significant technical improvement.

In the DDA strategy (Figure 9A), the MS instrument successively isolates the top N most abundant precursor ions in a full MS1 spectrum to sequentially acquire their MS2 spectra for peptide identification with a database search algorithm (Stahl, Swiderek et al. 1996, Mann, Hendrickson et al. 2001). But because of the performance limitation of MS in ion isolation for fragmentation and spectra acquisition, DDA strategy can result in losing MS2 spectra information of the low abundant precursor ions, which limits the dynamic range of the method and might cause reproducibility issue (Venable, Dong et al. 2004). The DIA strategy

## Introduction

(Figure 9B), on the other hand, was developed to overcome the limitation of DDA by continuously collecting MS2 spectra following a complete MS1 spectrum, so that all m/z value information at the MS1 and MS2 levels are acquired (Venable, Dong et al. 2004, Gillet, Navarro et al. 2012). As the MS2 spectra are collected to contain fragment ions information from multiple precursors in this strategy, it is usually very difficult to analyze these mass spectra. The Aebersold group developed a method in 2012, called “SWATH-MS”, short for Sequential Window Acquisition of All Theoretical Mass Spectra, to analyze the DIA data by using a predefined library as a reference, which contains the chromatographic and MS behavior of the peptides (Gillet, Navarro et al. 2012). This approach has been used to analyze protein samples, total cell lysates and tissue samples for quantification and post-translational modifications analysis, demonstrated with high reproducibility and accuracy (Guo, Kouvonen et al. 2015, Collins, Hunter et al. 2017, Rosenberger, Liu et al. 2017, Ludwig, Gillet et al. 2018).

### 1.7 Aim of this thesis

The main aim of this thesis is to characterize chRCC by systematic profiling of the chRCC tumors and adjacent healthy kidney tissues with MS-based proteomics and targeted metabolomics technologies as well as mitochondrial whole-exome sequencing. By integrative analysis of these omics data, I hope to reveal new molecular pathological mechanisms of this tumor. In this thesis, the proteome, metabolome data, and the mitochondrial mutations of nine chRCC cases were reported and analyzed. In addition, comparative analyses with the existing chRCC transcriptome data as well as the published omics data of RO (Kurschner, Zhang et al. 2017) were conducted to identify distinguishing markers of these two highly similar tumor types. Ultimately, the findings of this thesis will help in a more accurate diagnosis of this disease and will lead to the development of novel potential therapeutical treatments against chRCC.



## 2. Materials and methods

### 2.1 List of buffers

#### 2.1.1 Buffers for proteome profiling

##### Sodium deoxycholate (SDC) lysis buffer for tissue samples

- 1% (w/v) SDC
- 10 mM tris(2-carboxyl)phosphine (TCEP)
- 40 mM chloroacetamide (CAA)
- 100 mM Tris
- Adjust the pH to 8.5.

##### Guanidinium chloride (GdmCl) cell lysis buffer for cell samples

- 6M GdmCl
- 100 mM Tris-HCl
- 10 mM TCEP
- 40 mM CAA

#### 2.1.2 Buffers for enzymatic activity measurement

##### Sucrose homogenization buffer

- 20 mM Tris-HCl
- 40 mM KCl
- 2 mM ethylene glycol-bis( $\beta$ -aminoethyl ether)-N,N,N',N'-tetraacetic acid (EGTA)
- 250 mM sucrose
- Adjust the pH to 7.4, and add sucrose shortly before use.

##### PBS buffer (0.5 M, pH 7.5)

- Titrate 0.5 M  $K_2HPO_4$  buffer with 0.5 M  $KH_2PO_4$  buffer up to a pH of 7.5. Store at 4 °C for up to 2 months.

##### PBS buffer (0.1 M, pH 7.0)

- Titrate 0.1 M  $K_2HPO_4$  buffer with 0.1 M  $KH_2PO_4$  buffer up to a pH of 7.0. Store at 4 °C for up to 2 months.

### **Tris buffer with Triton X-100**

- 200 mM Tris
- 0.2% (v/v) Triton X-100
- Adjust the pH to 8.0 with HCl. Store at 4 °C for up to 2 months.

### **Reduced cytochrome c solution (1 mM)**

- 1 mM cytochrome c solution (oxidized status)
- In order to reduce the protein, add 5 µl of the 0.5 M dithiothreitol solution to 1 ml of 1 mM cytochrome c solution and mix gently, and wait for 15 minutes. The color of the solution should go from dark orange-red to pale purple-red. Measure the A<sub>550</sub>/A<sub>565</sub> ratio of an aliquot diluted 20-fold with 1× assay buffer (50 µl in 950 µl of 1× Assay Buffer). Use the 1× assay buffer to zero the spectrophotometer. The A<sub>550</sub>/A<sub>565</sub> ratio should be over 6.

### **Decylubiquinol solution (2.5 mM)**

- Add a few grains of sodium borohydride to 600 µl of 2.5 mM decylubiquinone solution in ethanol. Add 5-µl aliquots of 0.1 M HCl until the solution becomes colorless. Briefly spin the solution at 10,000g for 1 min and transfer the solution into a new 500-µl tube, avoiding any sodium borohydride crystals. Adjust the pH of the solution between 2 and 3 with 5-µl aliquots of 1 M HCl and keep the solution on ice protected from light.

Note: This solution should be freshly prepared. Caution: Sodium borohydride is highly toxic, avoid skin contact and inhalation.

### **4-Nitrophenyl N-acetyl-β-D-glucosaminide substrate solution (1 mg/ml)**

- 10 mg 4-Nitrophenyl N-acetyl-β-D-glucosaminide
- 10 ml of citrate buffer (0.09 M, pH 4.5)
- Mix the solution with rocking/shaking on a horizontal shaker at room temperature.

Note: The substrate does not easily dissolve in the buffer. It may take around 1 hour of shaking to completely dissolve the substrate. The use of a larger container (50 ml) may aid dissolution. The substrate solution should be stored on ice during the experiment. For longer storage of at least one month, store at -20 °C.

## Materials and methods

### 2.1.3 Buffers for western blot

#### Running buffer

- 25 mM Tris
- 192 mM glycine
- 0.1% (w/v) SDS
- Mix well until all the materials dissolved, adjust the pH to 7.6 before use.

#### Transfer buffer

- 25 mM Tris
- 192 mM glycine
- 20 % (v/v) methanol
- 0.1% (w/v) SDS
- Mix well until all the materials dissolved and adjust the pH to 8.3 before use.

#### TBST buffer

- 15 mM Tris-HCl
- 4.6 mM Tris
- 150 mM NaCl
- 0.1% (v/v) Tween 20
- Mix well until all the materials dissolved, adjust the pH to 7.6 before use.

#### Blocking buffer

- 5% (w/v) BSA in TBST buffer
- Mix well until all the materials dissolved.

## 2.2 Cell culture

The chromophobe RCC cell line UOK276 (Yang, Vocke et al. 2017) was provided by Dr. W. Marston Linehan from the National Cancer Institute, the United States of America. The UOK276 and the human kidney (HK-2, cortex/proximal tubule, ATCC CRL-2190) cell line were cultivated in Dulbecco's Modified Eagle Medium (DMEM; Life Technologies, New York, NY, USA) containing 4.5 g/L glucose, supplemented with 10% fetal bovine serum (FBS; Sigma-Aldrich, St. Louis, MO, USA) and 1% penicillin-streptomycin-neomycin (PSN; Invitrogen, Carlsbad, CA, USA) at 37 °C in a humidified atmosphere of 5% CO<sub>2</sub>.

For the proliferation assays, UOK276 and HK-2 cells were seeded in 96-well plates at a density of  $2 \times 10^4$  cells per well in complete medium. After 12 hours, cells were briefly rinsed and cultured in minimum essential medium (MEM; Thermo Fisher, Waltham, MA, USA) supplemented with 10% dialyzed FBS (Thermo Fisher), amino acid (AA; 0, 1, and 10% versus 100% relative to the AA level in MEM; Thermo Fisher), and bovine serum albumin (BSA; 0 and 2.5% total, Sigma-Aldrich) concentrations. The number of cells was determined with the cell counting kit 8 (Sigma-Aldrich) after 4 days.

### **2.3 Tissue dissection and verification of chRCC**

Nine pairs of chRCC and their non-malignant counterparts derived from nephrectomies at the Charité – Universitätsmedizin Berlin were collected in liquid nitrogen immediately after surgery and preserved at -80°C. The clinical characteristics of the tumors are reported in Table 2. From the collected tissue samples, histologic sections were stained with hematoxylin and eosin. The diagnosis of chRCC and the corresponding matched tumor-free kidney tissue was done according to the WHO classification criteria. Only cases with a clear diagnosis of chRCC were considered for the study.

**Table 2. Clinical and pathologic features of the chRCC cohort**

Case ID	Age at surgery	Gender	Pathologic T	Grade	Tumor Size (Max Dimension)	Nephrectomy
C1	49	Female	pT1a	2	28 mm	radical, left
C2	37	Female	pT2a	2	75 mm	radical, right
C3	42	Female	pT2a	2	98 mm	radical, left
C4	50	Male	pT3a	2	100 mm	radical, right
C5	71	Female	pT3a	3	70 mm	radical, right
C7	38	Female	pT1b	1	60 mm	partial, right
C8	58	Male	pT1b	1	65 mm	radical, left
C9	36	Female	pT2b	2	110 mm	radical, left
C10	46	Male	pT2a	0	74 mm	radical, right

### **2.4 Proteomics**

#### **2.4.1 Sample preparation for proteome profiling**

The tissue samples for proteomics were processed with iST 96X kits following the manufacturer's protocol (iST sample preparation kit 96X, PreOmics, Martinsried, Germany). Briefly, tissues were homogenized under denaturing conditions with a FastPrep (three times for 60 s,  $6.5 \text{ mx s}^{-1}$ ), followed by boiling at 95°C for 10 min. The lysates containing 40 µg protein were then digested by trypsin and Lys-C protease mixture at 37 °C overnight.

## Materials and methods

Subsequently, the peptides were purified with the cartridge and each sample was further separated using three fractions according to (Kulak, Pichler et al. 2014). A total of 10 µg of each fraction was analyzed by LC-MS for proteome profiling. All fractions were allocated to the corresponding replicate and analyzed jointly by the software tool MaxQuant (Cox and Mann 2008).

Proteomic profiling of the UOK276 cells was done as reported previously (Kurschner, Zhang et al. 2017) in biological triplicates. In the control group, the UOK276 cells were grown in 100% AA medium (relative to the AA level of MEM), in the treatment group, the medium was modified to contain only 1% AA (relative to the AA level of MEM), but supplied with 2.5 % BSA. The comparison proteomics was to investigate the global change of UOK276 cells on the proteome level when under nutrient-poor conditions.

### 2.4.2 LC-MS instrument settings and data analysis

LC-MS/MS was carried out by nanoflow reverse-phase liquid chromatography (Dionex Ultimate 3000, Thermo Fisher) coupled online to a Q-Exactive HF Orbitrap mass spectrometer (Thermo Fisher). Briefly, the LC separation was performed using a PicoFrit analytical column (75 µm ID × 55 cm long, 15 µm Tip ID (New Objectives, Woburn, MA) in-house packed with 3-µm C18 resin (Reprosil-AQ Pur, Dr. Maisch, Ammerbuch-Entringen, Germany). Peptides were eluted using a gradient from 3.8 to 40% solvent B in solvent A over 120 min at 266 nL per minute flow rate. Solvent A was 0.1 % formic acid and solvent B was 79.9% acetonitrile, 20% H<sub>2</sub>O, 0.1% formic acid. Nanoelectrospray was generated by applying 3.5 kV. A cycle of one full Fourier transformation scan mass spectrum (300–1750 m/z, resolution of 60,000 at m/z 200, AGC target 1e<sup>6</sup>) was followed by 16 data-dependent MS/MS scans (resolution of 30,000, AGC target 5e<sup>5</sup>) with a normalized collision energy of 27 eV. In order to avoid repeated sequencing of the same peptides, a dynamic exclusion window of 30 sec was used. In addition, only peptide charge states between two to eight were sequenced.

Raw MS data were processed with MaxQuant software (v1.6.0.1) (Cox and Mann 2008) and searched against the human proteome database UniProtKB with 70,941 entries, released in 01/2017. Parameters of MaxQuant database searching were: A false discovery rate (FDR) of 0.01 for proteins and peptides, a minimum peptide length of 7 amino acids, a mass tolerance of 4.5 ppm for precursor and 20 ppm for fragment ions were required. A maximum of two missed cleavages was allowed for the tryptic digest. Cysteine carbamidomethylation was set as a fixed modification, while N-terminal acetylation and methionine oxidation were

set as variable modifications. MaxQuant processed output files can be found in Supplemental Table S1, showing peptide and protein identification, accession numbers, % sequence coverage of the protein, q-values, and LFQ intensities. Contaminants, as well as proteins identified by site modification and proteins derived from the reversed part of the decoy database, were strictly excluded from further analysis.

#### **2.4.3 Gene set enrichment analysis**

For comprehensive proteome data analyses, gene set enrichment analysis (GSEA, v3.0) (Subramanian, Tamayo et al. 2005) was applied in order to see, if *a priori* defined sets of proteins show statistically significant, concordant differences between chRCC and kidney tissues. Only proteins with valid values in at least six of nine samples in at least one group with replacing missing values from the normal distribution for the other group were used (Supplemental Table S2). GSEA default settings were applied, except that the minimum size exclusion was set to 5 and KEGG v5.2 was used as a gene set database. The cut-off for significantly regulated pathways was set to a p-value  $\leq 0.01$  and FDR  $\leq 0.15$ .

### **2.5 Metabolomics**

#### **2.5.1 Metabolites extraction and reconstitution**

About 30 mg of 10 unrelated and N<sub>2</sub> shock froze chRCC and corresponding healthy kidney tissues were used for metabolite profiling. Metabolite extraction and tandem LC-MS measurements were done as previously reported (Meierhofer, Halbach et al. 2016, Kurschner, Zhang et al. 2017). In brief, methyl-tert-butyl ester (MTBE, Sigma-Aldrich), methanol, ammonium acetate, and water were used for metabolite extraction. Each cut tissue was homogenized first in 1.5 ml of methanol plus 0.2 ml of ammonium acetate, then 15  $\mu$ l of in-house internal standard mix (containing 30 pmol/L <sup>13</sup>C labeled glutamine, uracil, arginine, proline, valine, and unlabeled chloramphenicol), 5 ml of MTBE and 1.25 ml of LC-grade water were sequentially added into each replicate and incubated at room temperature (RT) for 1 hour at 1000 rpm in a thermal mixer, and then centrifuged for 10 minutes at 1,000 g at 4°C to achieve phase separation. The upper organic phase and lower aqueous phase were transferred and divided into three equal aliquots, and combined into three new tubes, so all the tubes contain an equal amount of organic and aqueous phases. The extracted metabolites in tubes were then air-dried in a SpeedVac and stored at -80°C before reconstitution. (All the debris from the interlayer and pellets were carefully avoided and kept at -80°C for DNA isolation.)

## Materials and methods

The three dried metabolite aliquots were reconstituted in 50 µl of H<sub>2</sub>O, methanol, and 68% acetonitrile in methanol, respectively. For the metabolites re-dissolved in 68% acetonitrile in methanol, 1.5 µl of Avanti Sph/Cer mix standard (Avanti, 25 µM stock, Alabaster, AL, USA) was added. All the reconstituted samples were sonicated twice in the ice-cold water bath for 5 minutes to ensure complete dissolve of the metabolites. After sonication, the samples were centrifuged at 18,000 g for 10 minutes and the 5 µl of the supernatant was injected into LC-MS/MS for measurement.

### 2.5.2 Metabolome profiling by targeted LC-MS

The subsequent separation was performed on an LC instrument (1290 series UHPLC; Agilent, Santa Clara, CA, USA), online coupled to a triple quadrupole hybrid ion trap mass spectrometer QTrap 6500 (Sciex, Foster City, CA, USA), as reported previously (Gielisch and Meierhofer 2015). Transition settings for multiple reaction monitoring (MRM) are provided in Supplemental Table S4. The metabolite identification was based on three levels: (i) the correct retention time, (ii) up to three MRM's and (iii) a matching MRM ion ratio of tuned pure metabolites as a reference (Gielisch and Meierhofer 2015). Relative quantification was performed using MultiQuantTM software v.2.1.1 (Sciex). The integration setting was a peak splitting factor of 2 and all peaks were reviewed manually. Only the average peak area of the first transition was used for calculations. Normalization was done according to used amounts of tissues and subsequently by internal standards, as indicated in Supplemental Table S4.

## 2.6 Analysis of TCGA chRCC RNA-seq data

TCGA (ID: KICH) RNA-seq data were obtained from UCSC Xena (Goldman, Craft et al. 2019) (<https://xenabrowser.net/>). Accurate transcript quantification of chRCC (n=66) and controls (n=25) was based on the RNA-Seq by Expectation Maximization (RSEM) method (Li and Dewey 2011).

## 2.7 Whole exome sequencing and mitochondrial bioinformatics analysis

DNA was isolated from the remaining pellets after metabolite extraction with a DNA purification kit according to the manufacturer's protocol (QIAamp DNA Mini Kit for Tissues, Qiagen, Hilden, Germany). In brief, the pellets were lysed by proteinase K and the RNA was removed by RNase, the RNA-free genomic DNA was then purified and eluted on QIAamp Mini spin columns for library preparation. The library preparation was performed according

to Agilent's SureSelect protocol (SureSelectXT Human All Exon V5, protocol version B4 August 2015) for Illumina paired-end sequencing, as reported previously (Kurschner, Zhang et al. 2017). The fastq files were used as input for the MToolBox pipeline (Calabrese, Simone et al. 2014), in order to extract mitochondrial DNA sequences and quantify each variant allele heteroplasmy, as done previously (Kurschner, Zhang et al. 2017).

## 2.8 Measurement of the enzyme activities

### 2.8.1 Sample preparation for enzyme activity measurement

Sample preparation for spectrophotometric assay enzyme activity was done as reported previously (Gielisch and Meierhofer 2015). In brief, approximately 5 mg of the tumor and healthy kidney tissues were homogenized in sucrose homogenization buffer and centrifuged at 600 g at 4 °C for 10 min. The protein concentrations of supernatants were further determined with a bicinchoninic acid (BCA) assay (Thermo Fisher). For complex I, II, and V, 4 µg protein of each sample was used for the enzymatic activity measurement; for complex III, IV, and citrate synthase, 2 µg protein was used. Rotenone (10 µM), malonic acid (5 mM), antimycin A (5 µg/ml), potassium cyanide (500 µM), and oligomycin (5 µg/ml) served as specific inhibitors for complex I to V, respectively. The enzymatic activities of the hexosaminidases A and B were assayed as previously described by using 4-nitrophenyl N-acetyl-β-D-glucosaminide as an artificial substrate (Shibata and Yagi 1996). 4 µg protein for the tissue samples and 1.5 µg for cell samples were used for the hexosaminidases A and B assay. Heat inactivation of hexosaminidase B was performed by pre-incubation of samples for 3 h at 48 °C (Grabowski, Kruse et al. 1984). The detailed protocols for individual enzyme activity measurement were listed as follows:

### 2.8.2 Enzymatic activity measurement of Complex I

- Prepare the buffers to detect the complex I activity (for 70 samples):

#### Complex I buffer (14 ml):

9.8 ml H<sub>2</sub>O

1.4 ml PBS (0.5 M, pH 7.5)

840 µl 50 mg/ml BSA solution

420 µl 10 mM KCN solution

140 µl 10 mM NADH solution

Mix the above solution evenly and well in a 15 ml Falcon tube, put on ice before use;

420 µl 2 mM ubiquinone Q<sub>1</sub> solution

## Materials and methods

700 µl 0.2 mM rotenone solution

- Add 10 µl of tissue homogenate to the well of a 96-well plate, for each well, add 200 µl complex I buffer, incubate at 37 °C and read the absorbance at 340 nm for 5 min;
- Start the reaction by adding 6 µl of 2 mM ubiquinone Q<sub>1</sub> solution, monitor the absorbance at 340 nm for 5 min.
- Stop the reaction by adding 10 µl 0.2 mM rotenone solution, monitor the absorbance at 340 nm for another 5 min.
- To calculate the enzymatic activity of complex I, the values of the Δ change of absorbance per minute after rotenone addition was subtracted from values of the Δ change of absorbance per minute total, the equation of calculating the enzymatic activity:

$$\text{Activity}_{\text{complex I}} (\text{nmol/min/mg}) = \frac{[\Delta A_{340}(\text{without rotenone}) - \Delta A_{340}(\text{with rotenone})] \times 1000}{\epsilon (\text{mM}^{-1} \text{cm}^{-1}) \times \text{time(min)} \times \text{protein amount(mg)}}$$

The extinction coefficient ( $\epsilon$ ) for NADH at 340 nm is 6.2 mM<sup>-1</sup> cm<sup>-1</sup> (Spinazzi, Casarin et al. 2012).

### 2.8.3 Enzymatic activity measurement of Complex II

- Prepare the buffers to detect the complex II activity (for 70 samples):

#### Complex II buffer (14 ml):

9.87 ml H<sub>2</sub>O

700 µl PBS (0.5 M, pH 7.5)

280 µl 50mg/ml BSA solution

420 µl 10 mM KCN solution

700 µl 400 mM succinate solution

2.03 ml 0.015% (w/v) 2, 6-dichlorophenolindophenol (DCPIP) sodium solution

Mix the above solution evenly and well in a 15 ml Falcon tube, put on ice before use;

280 µl 2.5 mM decylubiquinone solution

700 µl 0.1 M malonic acid solution

- Add 10 µl of tissue homogenate to the well of a 96-well plate, for each well, add 200 µl complex II buffer, incubate at 37 °C and read the absorbance at 600 nm for 5 min;
- Start the reaction by adding 4 µl of 2.5 mM decylubiquinone solution, monitor the absorbance at 600 nm for 5 min.
- Stop the reaction by adding 10 µl 0.1 M malonic acid solution, monitor the absorbance at 600 nm for another 5 min.

- To calculate the enzymatic activity of complex II, the values of the  $\Delta$  change of absorbance per minute after malonic acid addition was subtracted from values of the  $\Delta$  change of absorbance per minute total, the equation of calculating the enzymatic activity:

$$\text{Activity}_{\text{complex II}} \text{ (nmol/min/mg)} = \frac{[\Delta A_{600}(\text{without malonic acid}) - \Delta A_{600}(\text{with malonic acid})] \times 1000}{\varepsilon (\text{mM}^{-1} \text{cm}^{-1}) \times \text{time(min)} \times \text{protein amount(mg)}}$$

The extinction coefficient ( $\varepsilon$ ) for DCPIP at 600 nm is  $19.1 \text{ mM}^{-1} \text{ cm}^{-1}$  (Spinazzi, Casarin et al. 2012).

#### 2.8.4 Enzymatic activity measurement of Complex III

- Prepare the buffers to detect the complex III activity (for 70 samples):

##### **Complex III buffer (14 ml):**

11.13 ml H<sub>2</sub>O

750 µl PBS (0.5 M, pH 7.5)

1050 µl 1 mM oxidized cytochrome C solution

700 µl 10 mM KCN solution

280 µl 5 mM EDTA solution

140 µl 2.5% (w/v) Tween-20 solution

Mix the above solution evenly and well in a 15 ml Falcon tube, put on ice before use;

560 µl 2.5 mM decylubiquinol solution

700 µl 0.1 mg/ml antimycin A solution

- Add 10 µl of tissue homogenate to the well of a 96-well plate, for each well, add 200 µl complex III buffer, incubate at 37 °C and read the absorbance at 550 nm for 5 min;
- Start the reaction by adding 8 µl of 2.5 mM decylubiquinol solution, monitor the absorbance at 550 nm for 5 min.
- Stop the reaction by adding 10 µl of 0.1mg/ml antimycin A solution, monitor the absorbance at 550 nm for another 5 min.
- To calculate the enzymatic activity of complex III, the values of the  $\Delta$  change of absorbance per minute after antimycin A was added was subtracted from values of the  $\Delta$  change of absorbance per minute total, the equation of calculating the enzymatic activity:

$$\text{Activity}_{\text{complex III}} \text{ (nmol/min/mg)} = \frac{[\Delta A_{550}(\text{without antimycin A}) - \Delta A_{550}(\text{with antimycin A})] \times 1000}{\varepsilon (\text{mM}^{-1} \text{cm}^{-1}) \times \text{time(min)} \times \text{protein amount(mg)}}$$

## Materials and methods

The extinction coefficient ( $\epsilon$ ) for reduced cytochrome C at 550 nm is  $18.5 \text{ mM}^{-1} \text{ cm}^{-1}$  (Spinazzi, Casarin et al. 2012).

### 2.8.5 Enzymatic activity measurement of Complex IV

- Prepare the buffers to detect the complex IV activity (for 70 samples):

#### Complex IV buffer (14 ml):

6.16 ml H<sub>2</sub>O

7 ml PBS (0.1 M, pH 7.0)

840 µl 1mM reduced cytochrome C solution

Mix the above solution evenly and well in a 15 ml Falcon tube, put on ice before use;

420 µl 10 mM KCN solution

- Add 10 µl of tissue homogenate to the well of a 96-well plate, for each well, add 200 µl complex IV buffer, incubate at 37 °C and read the absorbance at 550 nm for 5 min;
- Stop the reaction by adding 6 µl of 10 mM KCN solution, monitor the absorbance at 550 nm for another 5 min.
- To calculate the enzymatic activity of complex IV, the values of the  $\Delta$  change of absorbance per minute after KCN addition was subtracted from values of the  $\Delta$  change of absorbance per minute total, the equation of calculating the enzymatic activity:

$$\text{Activity}_{\text{complex IV}} (\text{nmol/min/mg}) = \frac{[\Delta A_{550(\text{without KCN})} - \Delta A_{550(\text{with KCN})}] \times 1000}{\epsilon (\text{mM}^{-1} \text{cm}^{-1}) \times \text{time(min)} \times \text{protein amount(mg)}}$$

The extinction coefficient ( $\epsilon$ ) for reduced cytochrome C at 550 nm is  $18.5 \text{ mM}^{-1} \text{ cm}^{-1}$

(Spinazzi, Casarin et al. 2012).

### 2.8.6 Enzymatic activity measurement of Complex V

- Prepare the buffers to detect the complex V activity (for 70 samples):

#### Complex V buffer (14 ml):

5.8 µl lactate dehydrogenase (final concentration 4 U/ml);

17.5 µl pyruvate kinase (final concentration 4 U/ml)

280 µl 10 mM NADH solution;

140 µl 200 mM phosphoenolpyruvic acid solution;

140 µl 100 mM ATP solution;

280 µl 50mg/ml BSA solution;

14 µl 0.1 mg/ml antimycin A solution;

140 µl 300 µM carbonyl cyanide 4-(trifluoromethoxy)phenylhydrazone solution;  
Then add Tris (40 mM, pH 8.0) with 5 mM MgCl<sub>2</sub> and 10 mM KCl to a final volume of 14 mL, mix the above solution evenly and well in a 15 ml Falcon tube, put at 37 °C 3 min before use;

700 µl 0.1 mg/ml oligomycin solution

- Add 10 µl of tissue homogenate to the well of a 96-well plate, for each well, add 200 µl complex V buffer, incubate at 37 °C and read the absorbance at 340 nm for 5 min;
- Stop the reaction by adding 10 µl of 0.1 mg/ml oligomycin solution, monitor the absorbance at 340 nm for another 5 min.
- To calculate the enzymatic activity of complex V, the values of the Δ change of absorbance per minute after oligomycin addition was subtracted from values of the Δ change of absorbance per minute total, the equation of calculating the enzymatic activity:

$$\text{Activity}_{\text{complex V}} (\text{nmol/min/mg}) = \frac{[\Delta A_{340}(\text{without oligomycin}) - \Delta A_{340}(\text{with oligomycin})] \times 1000}{\varepsilon (\text{mM}^{-1} \text{cm}^{-1}) \times \text{time(min)} \times \text{protein amount(mg)}}$$

The extinction coefficient ( $\varepsilon$ ) for NADH at 340 nm is 6.2 mM<sup>-1</sup> cm<sup>-1</sup> (Spinazzi, Casarin et al. 2012).

### 2.8.7 Enzymatic activity measurement of citrate synthase

- Prepare the buffers to detect the citrate synthase activity (for 70 samples):

**Citrate synthase buffer (14 ml):**

5.18 ml H<sub>2</sub>O

7 ml Tris buffer (200 mM, pH 8.0) with 0.2% (v/v) Triton X-100

1.4 ml 1 mM 5,5'-dithiobis(2-nitrobenzoic acid) (DTNB) solution

420 µl 10 mM acetyl CoA solution

Mix the above solution evenly and well in a 15 ml Falcon tube, put on ice before use;

700 µl 10 mM oxaloacetic acid solution

- Add 10 µl of tissue homogenate to the well of a 96-well plate, for each well, add 200 µl citrate synthase buffer, incubate at 37 °C and read the absorbance at 412 nm for 5 min;
- Start the reaction by adding 10 µl of 10 mM oxaloacetic acid solution, monitor the absorbance at 412 nm for 5 min.

## Materials and methods

- To calculate the enzymatic activity of citrate synthase, the values of the  $\Delta$  change of absorbance per minute after oxaloacetic acid addition was used, the equation of calculating the enzymatic activity:

$$\text{Activity}_{\text{citrate synthase}} \text{ (nmol/min/mg)} = \frac{\Delta A_{412} \times 1000}{\epsilon(mM^{-1}cm^{-1}) \times \text{time(min)} \times \text{protein amount(mg)}}$$

The extinction coefficient ( $\epsilon$ ) for DTNB at 412 nm was  $13.6 \text{ mM}^{-1} \text{ cm}^{-1}$  (Ellman 1958).

### 2.8.8 Enzymatic activity measurement of hexosaminidase A and B

- Equilibrate all the solutions to  $37^\circ\text{C}$  by incubating for several minutes.
- Set the spectrophotometry plate reader at 400 nm.
- Add  $10 \mu\text{l}$  sample and then  $90 \mu\text{l}$  of  $1 \text{ mg/ml}$  4-nitrophenyl N-acetyl- $\beta$ -D-glucosaminide substrate solution to the 96-well plates and mix using a horizontal shaker or by pipetting, measure the absorption at 400 nm immediately at time 0.
- Incubate the plate for 5-10 minutes at  $37^\circ\text{C}$ . If one suspects that the total beta-hexosaminidase activity of the test sample may be low, the incubation time can be extended up to 30 minutes. (The tissue samples were incubated for 20 minutes, cell samples 30 minutes)
- Stop the reactions by adding  $200 \mu\text{l}$  of  $400 \text{ mM}$  sodium carbonate buffer to each well, and then measure the absorption at 400 nm.
- Calculate the total enzyme activity with the following equation:

$$\text{Activity}_{\text{total}} \text{ (nmol/min/mg)} = \frac{\Delta A_{400} \times 1000}{\epsilon(mM^{-1}cm^{-1}) \times \text{time(min)} \times \text{protein amount(mg)}}$$

The extinction coefficient ( $\epsilon$ ) for 4-nitrophenoxide at 400 nm was  $18.6 \text{ mM}^{-1} \text{ cm}^{-1}$  (Shibata and Yagi 1996).

- After pre-incubating the samples for 3 hours at  $48^\circ\text{C}$  (Grabowski, Kruse et al. 1984) to inactivate hexosaminidase B, measure the hexosaminidase A activity by following the same protocol as the total enzyme activity measurement.
- Calculate the hexosaminidase B activity with the following equation:

$$\text{Activity}_{\text{hexosaminidase B}} = \text{Activity}_{\text{total}} - \text{Activity}_{\text{hexosaminidase A}}$$

### 2.9 Determination of free and total GSH in plasma and urine

(This part was done by the colleagues from Charité - Universitätsmedizin Berlin.)

Since the increased GSH level is a hallmark in RO and chRCC tissues, I wondered, if this was also reflected in plasma and urine to establish a non-invasive metabolic marker. Therefore, plasma- (6 RO, 6 ccRCC, 12 pRCC, 6 chRCC, and 6 healthy) and urine

specimens (8 RO, 20 ccRCC, 19 pRCC, 7 chRCC, and 20 healthy) were investigated. Free and total GSH was measured using a glutathione fluorescent detection kit according to the manufacturer's protocol (Invitrogen).

## **2.10 The ethidium bromide treated UOK276 cells as an mtDNA depletion cell model**

The UOK276 cells cultured in normal medium (DMEM supplemented with 10% FBS and 1% PSN) were seeded into T75 flask in triplicates. 24 hours after plating cells, the medium was supplemented with 100 ng/ml ethidium bromide (EtBr) to induce mtDNA depletion. The cells were then seeded into 6-well plates, on day 0, 2, 5, 8, 13, 19, the treated cells were collected and frozen immediately at -80°C for the measurement of GSH level, mtDNA, RNA and protein correlation.

### **2.10.1 GSH extraction in ethidium bromide treated cells**

The EtBr treated cells in 6-well plates were took out from -80°C, immediately, 1 ml ice-cold methanol/chloroform (9/1, v/v) mix solution was added to each well to extract GSH from the cells. Then the 6-well plates were incubated on ice for 5 minutes, and the cells were scraped off by cell scraper and collected into a new 1.5 ml tube. The collected samples were then centrifuged at 10, 000 g for 10 minutes at 4°C, the precipitated pellets were kept for DNA isolation, and the supernatants were air-dried in speed-Vac and then re-dissolved by adding 85 µl 80% acetonitrile with 3 µM chloramphenicol (as internal standard), 20 µl re-dissolved sample was injected into the LC-MS system for analysis.

### **2.10.2 Relative quantification of mtDNA content by qPCR**

#### **2.10.2.1 DNA isolation**

The remaining pellets after GSH extraction were used for genomic DNA isolation. The DNA isolation was done by using a QIAamp DNA micro kit according to the manufacturer's protocol (QIAamp DNA Micro Kit, Qiagen). The purified DNA was quantified by using the NanoDrop 1000 spectrophotometer (Thermo Fisher).

#### **2.10.2.2 Confirmation of the p<sup>0</sup> status by qPCR**

The depletion of mtDNA in EtBr treated cells was verified by qPCR. Here, a 399-bp mtDNA product that spans the region of nt 3153 – nt 3551 (Primer: 5' TTCACAAAGCGCCTCCCCGT and 5' GCGATGGTGAGAGCTAAGGTCGGG) and a

## Materials and methods

238-bp nuclear DNA product that spans the region of exon 5 (nt 55953445 – nt 55953207) of the gene USMG5 (Primer: 5'AGTGTCTTAAGAGTAAAGCTGGCCACA and 5' TTGCCTTGTTGCATTTCTACAG) were analyzed. QPCR for the nuclear DNA and mtDNA products were performed with 10 ng and 0.5 ng of genomic DNA as template, respectively, 0.4  $\mu$ M of each primer and the GoTaq qPCR Master Mix (Promega, Madison, WI, USA) were used, detailed reaction mix preparation is listed as in Table 3 (20  $\mu$ l per reaction).

**Table 3. qPCR reaction mix asssembling**

Component	Volume ( $\mu$ l)	Final Concentration
GoTaq qPCR Master Mix (2X)	10	1X
Forward Primer (10 mM)	0.8	400nM
Reverse Primer (10 mM)	0.8	400nM
CXR reference dye	0.2	
Nuclease-Free Water	8.2	

The thermal cycling conditions for both nuclear and mtDNA qPCR were listed in Table 4 and run in a 7900HT real-time PCR system (Applied Biosystems, Foster City, CA, USA).

**Table 4. qPCR thermal cycling conditions**

Step	Cycles	Temperature (°C)	Time
Initial polymerase activation	1	95	10 minutes
Denaturation	1	95	15 seconds
Annealing and elongation	40	60	60 seconds

### 2.10.3 Reverse transcription-quantitative PCR (RT-qPCR)

#### 2.10.3.1 RNA and protein isolation with TRIzol reagent

The RNA and protein in the EtBr treated cells were simultaneously isolated from the same sample by TRIzol reagent (Sigma-Aldrich). The isolation process with TRIzol was performed according to the instruction of the manufacturer with some minor modifications. The detailed protocol was shown as follows: The EtBr treated cells in 6-well plates were dissolved in 1 ml TRIzol solution per well, lysed by repeated pipetting, then transferred to a new 2 ml tube and incubated for 10 min. For phase separation, 200  $\mu$ l of chloroform was added, the samples were covered tightly, shaken vigorously for 15 seconds, and incubated for 5 min at RT, followed by centrifugation at 18,000 g for 15 min at 4 °C. After phase separation, the upper RNA containing phase was mixed with 500  $\mu$ l of ice-cold isopropanol, incubated for 10 min at RT, and centrifuged for 20 min at 18,000 g at 4 °C. The lower phase was kept for protein

extraction. The obtained RNA pellet was washed twice using 1 mL of 75% (v/v) ethanol, vortexed and then centrifuged at 18,000 g for 5 minutes at 4 °C, the RNA pellet was air-dried for 10 min at RT, and resuspended in 60 µl of H<sub>2</sub>O. The purified RNA was quantified by using the NanoDrop 1000 spectrophotometer (Thermo Fisher).

For protein extraction, 1.5 ml of ice-cold isopropanol was added to the remaining lower phase, and the samples were incubated overnight at -20 °C to precipitate the proteins. The solution was then centrifuged for 15 min at 18,000 g at 4 °C. The protein pellet was washed twice by the addition of 1 ml 0.3 M guanidinium chloride in 95% (v/v) ethanol, incubation for 10 min at RT, and subsequent centrifugation for 5 min at 10,000 g at 4 °C. The pellet was washed a second time with 1 ml of ethanol and air-dried for 20 min at RT, dissolved in 100 µl of 1% SDS and 100 µl 8 M urea in 100 mM Tris-HCl (pH 8.0) solution. The isolated protein was quantified by the BCA assay (Thermo Fisher).

#### **2.10.3.2 Mitochondrial transcripts quantification by RT-qPCR**

Four mitochondrial transcripts, MT-ND5, NDUFS1, UQCRC2, SDHB, were quantified by RT-qPCR, the SLC1A4 transcript was used as a loading control. Five primer pairs were designed by Primer-BLAST (Ye, Coulouris et al. 2012), synthesized by Eurofins Genomics (Ebersberg, Germany) and listed in Table 5. All the primer pairs were designed to be separated by at least one intron on the corresponding genomic DNA, except for MT-ND5.

RT-qPCR of the four transcripts was performed with 100 ng RNA template, 0.2 µM of each primer and the GoTaq 1-Step RT-qPCR System (Promega) was used. Detailed reaction mix preparation is listed as in Table 6 (20 µl per reaction). The thermal cycling conditions for all the RT-qPCR reactions were identical as in Table 7 and run a 7900HT real-time PCR system (Applied Biosystems).

**Table 5. Primer sequences used to amplify mitochondrial transcripts**

Target	Primer sequence (5'->3') F: forward, R: reversed	Product length	Total intron size	Melting temperature (T <sub>m</sub> , °C)
MT-ND5	F: CCGGAAGCCTATT CGCAGGA R: ACAGCGAGGGCTGTGAGTTT	103 bp	--	F: 62.03 R: 62.04
NDUFS1	F: TGCTGAAGCCCTGGTAGCTC R: TGCCTCTTCCACACCAGCAA	151 bp	616 bp	F: 61.90 R: 61.99
SDHB	F: GACGGGCTCTACGAGTGCAT R: TGATGGTGTGGCAGCGGTAT	199 bp	1242 bp	F: 62.01 R: 61.91
UQCRC2	F: AACCACCCATTGCTCGTC R: TCCCTTGTGCGGTACACT	117 bp	968 bp	F: 61.81 R: 61.98
SLC1A4	F: AGCAGCCATCTCCAGTGTGT R: GGTCATGAGTAGGCAGCCAA	191 bp	279 bp	F: 62.00 R: 62.13

## Materials and methods

**Table 6. RT-qPCR reaction mix assembling**

<b>Component</b>	<b>Volume (µl)</b>	<b>Final Concentration</b>
GoTaq qPCR Master Mix (2X)	10	1X
GoScript RT Mix for 1-Step RT-qPCR (50X)	0.4	1X
Forward Primer (100 µM)	0.04	200nM
Reverse Primer (100 µM)	0.04	200nM
CXR reference dye	0.33	
Nuclease-Free Water	9.19	

**Table 7. RT-qPCR thermal cycling conditions**

<b>Step</b>	<b>Cycles</b>	<b>Temperature (°C)</b>	<b>Time</b>
Initial reverse transcription	1	37.5	15 minutes
Reverse transcriptase inactivation and polymerase activation	1	95	10 minutes
Denaturation	1	95	10 seconds
Annealing and data collection	40	60	30 seconds
Elongation	40	72	30 seconds

### 2.10.4 Western blot

As described above, the protein of the EtBr treated cells was isolated following the RNA extraction with the TRIzol reagent (Sigma-Aldrich). Four mitochondrial complexes subunits, three encoded by the nuclear DNA, NDUFS1, SDHB, UQCRC2, and one encoded by the mtDNA, MT-ND5, were quantified by western blotting. In brief, the western blotting was performed with the Bio-Rad systems (Hercules, CA, USA) following the manufacturer's instructions. First, the isolated protein was diluted with 4X Laemmli buffer to the desired concentration, then boiled at 95°C for 10 minutes. Then, 15 µl of each protein samples (containing 2.8 µg protein) were loaded to a 4-15% precast Mini-PROTEAN TGX gel (Bio-Rad), and run at constant 100 V voltage for about 1 hour in 1X running buffer with a Mini-PROTEAN electrophoresis system (Bio-Rad). The separated proteins in the gel were then transferred to a polyvinylidene fluoride membrane in an ice-chilled transfer buffer by a Mini Trans-Blot system (Bio-Rad) at a consistent 350 mA current for about 1 hour. The resulting membrane was blocked in 5% BSA in TBST buffer for 1 hour at RT and then incubated in the corresponding primary antibody (Table 8) at 4°C overnight. After 5 times wash with TBST buffer to remove the residue primary antibodies, the membrane was incubated in the secondary antibody at RT for 1 hour. Then the horseradish peroxidase substrate for enhanced chemiluminescence was directly applied to the membrane and the images were captured by using the Fusion SL imaging system (Vilber Lourmat, Eberhardzell, Germany).

**Table 8. Used primary antibodies for the detection of mitochondrial proteins**

Antibodies	Manufacturer	Catalogue No.
Anti-MT-ND5 rabbit polyclonal antibody	Thermo Fisher	PA5-39277
Anti-NDUFS1 rabbit polyclonal antibody	Proteintech	12444-1-AP
Anti-SDHB rabbit polyclonal antibody	Sigma	HPA002868
Anti-UQCRC2 rabbit polyclonal antibody	Sigma	HPA007998

## 2.11 Stable isotopic tracer to quantify the endocytosis in chRCC cells

The chromophobe RCC cells UOK276 were initially cultured in normal DMEM (Life Technologies) supplemented with 10% dialyzed FBS (Thermo Fisher) and 1% PSN (Invitrogen) at 37 °C in a humidified atmosphere of 5% CO<sub>2</sub>. Then the medium was modified to EBSS medium containing <sup>13</sup>C<sup>15</sup>N labeled amino acid (<sup>13</sup>C<sup>15</sup>N-AA; Cambridge Isotope Laboratories, Tewksbury, MA, USA) at the same concentrations of DMEM, 10% dialyzed FBS and 1% PSN. UOK276 Cells were grown for ten doublings in the <sup>13</sup>C<sup>15</sup>N-AA medium to ensure the full labeling of the intercellular proteins and free AAs. After ten doublings, cells were seeded at low cell density in the 6-well plate and switched to 2mL of 1% <sup>13</sup>C<sup>15</sup>N-AA medium supplemented with 2.5% BSA. After 5 hours, the medium was removed and collected to a new 1.5 ml tube, after being washed twice with ice-cold PBS, the cells in each well were added 300 µl of 0.1% triton X100 in PBS and then collected by using a scraper, the cell lysate was sonicated for one minute, all the medium and cell lysate were centrifuged at 1,000 g for 10 min at 4 °C. After centrifuging, 50 µl of supernatant was taken into a new 1.5 ml tube, 150 µl methanol and 10 µl IS (3 µM chloramphenicol) were add and vortexed for 10 min with the Thermomixer (Thermo Fisher) at 1400 rpm, then centrifuged for 10 min at 18,000 g at 4°C, 20 µl of supernatant per run was injected to the LC-MS/MS for analysis. To study the inhibition effect of the endocytosis by the PLCG pathway inhibitors, the cells were treated for 5 hours with different inhibitors, and then the total amino acids in cells and medium were extracted following the above-described protocol and injected to the LC-MS/MS for relative quantification.

## 2.12 ROS measurement method development

Hydroethidine (HE, D1168) and mito-hydroethidine (mito-HE, M36008) were purchased from Invitrogen. Hydropropidine (HPr<sup>+</sup>) was a kind gift from Prof. Jacek Zielonka, Medical College of Wisconsin.

## Materials and methods

### 2.12.1 Synthesis of oxidation products derived from HE, mito-HE, and HPr<sup>+</sup>

The synthesis of oxidation products was done as previously described (Zielonka, Hardy et al. 2009). In brief, 2-OH-E<sup>+</sup> and 2-hydroxy-mito-ethidium (2-OH-mito-E<sup>2+</sup>) were synthesized by oxidizing HE and mito-HE with potassium nitrosodisulfonate (NDS). E<sup>+</sup> and mito-ethidium (mito-E<sup>2+</sup>) were synthesized by reacting HE and mito-HE with chloranil, diethidium (di-E<sup>+</sup>) and di-mito-ethidium (di-mito-E<sup>2+</sup>) and reacting HE and mito-HE with potassium ferricyanide. 2-hydroxypropidium (2-OH-Pr<sup>2+</sup>), propidium (Pr<sup>2+</sup>), and dipropidium (di-Pr<sup>2+</sup>) were derived from HPr<sup>+</sup> and synthesized using a procedure similar to that used to synthesize corresponding products from HE (Michalski, Zielonka et al. 2013).

### 2.12.2 Generation of MRM methods for fluorogenic probes and derived oxidation products and LC-MS/MS conditions

The educts and oxidation products of the three probes were tuned individually to identify and optimize specific transitions for the QTrap 6500 mass spectrometer (Sciex). About 100 ng/µL of all compounds were dissolved in methanol and a constant flow of 7 µL/min was used. The automatic optimization procedure in the analyst software (v.1.6.2) was used. The ten most intense fragment masses per compound were optimized for collision energy, declustering potential, and the collision cell exit potential (Table 9).

**Table 9. MRM transitions and MS parameters of the fluorogenic probes.**

Compound	Q1 mass (Da)	Q3 mass (Da)	RT (min)	DP (V)	CE (V)	CXP (V)	MRM ion ratio
HE	316.2	210.1	6.75	76	43	24	1
HE	316.2	287.1	6.75	76	29	28	0.71
HE	316.2	271.1	6.75	76	41	14	0.16
2-OH-E <sup>+</sup>	330.2	301.1	4.95	101	37	8	1
2-OH-E <sup>+</sup>	330.2	300.1	4.95	101	55	28	0.93
2-OH-E <sup>+</sup>	330.2	255.1	4.95	101	69	12	0.84
E <sup>+</sup>	314.1	284.1	5.15	1	51	24	1
E <sup>+</sup>	314.1	286.1	5.15	1	39	16	0.80
E <sup>+</sup>	314.1	285.1	5.15	1	37	18	0.69
di-E <sup>+</sup>	313.2	285.1	5.22	141	35	26	1
di-E <sup>+</sup>	313.2	284.1	5.22	141	41	26	0.77
di-E <sup>+</sup>	313.2	299.1	5.22	141	31	10	0.56

*Continued on the next page*

*Continued from the previous page*

Compound	Q1 mass (Da)	Q3 mass (Da)	RT (min)	DP (V)	CE (V)	CXP (V)	MRM ion ratio
mito-HE	316.7	278.1	7.49	1	19	32	1
mito-HE	316.7	209.1	7.49	1	43	22	0.28
mito-HE	316.7	183.1	7.49	1	77	16	0.14
2-OH-mito-E <sup>2+</sup>	323.7	300.1	5.53	111	41	14	1
2-OH-mito-E <sup>2+</sup>	323.7	262.1	5.53	111	33	24	0.72
2-OH-mito-E <sup>2+</sup>	323.7	289.1	5.53	111	37	8	0.54
mito-E <sup>2+</sup>	316.1	285.1	5.64	96	31	18	1
mito-E <sup>2+</sup>	316.1	262.1	5.64	96	31	18	0.80
mito-E <sup>2+</sup>	316.1	289.1	5.64	96	37	14	0.61
di-mito-E <sup>2+</sup>	316.1	285.1	5.63	111	31	26	1
di-mito-E <sup>2+</sup>	316.1	262.1	5.63	111	33	22	0.84
di-mito-E <sup>2+</sup>	316.1	345.1	5.63	111	31	26	0.72
HPr <sup>+</sup>	415.3	272.1	4.53	60	49	16	1
HPr <sup>+</sup>	415.3	328.1	4.53	60	25	10	0.25
HPr <sup>+</sup>	415.3	300.1	4.53	60	31	20	0.80
2-OH-Pr <sup>2+</sup>	215.1	266.1	4.42	60	25	24	1.00
2-OH-Pr <sup>2+</sup>	215.1	300.1	4.42	60	23	26	0.75
2-OH-Pr <sup>2+</sup>	215.1	72.0	4.42	60	25	10	0.63
Pr <sup>2+</sup>	207.2	72.0	4.37	60	23	8	1
Pr <sup>2+</sup>	207.2	250.0	4.37	60	25	24	0.64
Pr <sup>2+</sup>	207.2	163.5	4.37	60	21	16	0.40
di-Pr <sup>2+</sup>	413.1	326.1	4.35	111	21	26	1
di-Pr <sup>2+</sup>	413.1	331.1	4.35	111	21	18	0.02
di-Pr <sup>2+</sup>	413.1	213.1	4.35	111	37	20	0.00
IS	323.1	275.1	5.00	50	20	14	1.00
IS	323.1	165.0	5.00	50	37	11	0.52
IS	323.1	83.0	5.00	60	95	9	0.23

IS, internal standard chloramphenicol; RT, retention time; DP, declustering potential; CE, collision energy; CXP, collision cell exit potential; MRM ion ratio, peak areas of all transitions were divided by the highest peak area per compound.

Three different LC columns and several different buffer conditions were used to identify the highest peak areas, optimal peak shapes, and retention times, as described previously (Gielisch and Meierhofer 2015). Finally, a ReproSil-PUR C18-AQ (1.9 µm, 120 Å, 150 x

## Materials and methods

2 mm ID; Dr. Maisch; Ammerbuch, Germany) with the following buffer and run conditions were selected for metabolite separation: A1: LC-MS grade water; 0.1% formic acid; B1: LC-MS grade acetonitrile; 0.1% formic acid. Gradients and flow conditions were as follows: the compounds were separated by a linear increase of B1 from 20% to 95% in 8 min and maintained at 95% B1 for 1 min. The concentration of B1 was then reduced to 20% in 1 min, and this level was maintained until minute 10. All optimized MRM transitions and retention times are shown in Table 9.

Fragmentation patterns of the probes and O<sub>2</sub><sup>-</sup>-specific products were recorded by a Q Exactive HF mass spectrometer (Thermo Fisher) with a high resolution of 60,000. The fragment mass identity was verified using ACD Spectrus Processor 2017.2.1 software. Assigned fragment masses differed by less than 0.001 Da from theoretically calculated masses and assignments are shown in Figure 26.

### **2.12.3 Sample preparation for fluorogenic probe stability tests and metabolite extraction**

The stability of all three fluorogenic probes was tested in Hank's solution (Thermo Fisher) to evaluate autoxidation rates under cell-free conditions. Each probe (2 µM) was incubated in 50 µL Hank's solution for 0, 10, 30, 60, and 150 min under the following three conditions in triplicate: 25°C with light, 25°C without light, and 37°C without light. 200 µL acetonitrile and 20 µL of 1 mM internal standard (chloramphenicol) were added, vortexed (800 rpm) for 5 min at room temperature and centrifuged at 8,000 g for 5 min at 4°C to extract the probes. 20 µL of each supernatant was analyzed by LC-MS/MS to evaluate the autoxidation rates.

### **2.12.4 Metabolite extraction and determination of ROS status in a cell line**

For proof of principle, ROS signatures were induced or scavenged by chemical treatments to detect compartment-specific signals for HE, mito-HE, and HPr<sup>+</sup> using the established LC-MS/MS method. HepG2 cells were treated with two chemical ROS stimuli, H<sub>2</sub>O<sub>2</sub> (100 µM) and rotenone (1 µM) for 2 hours, as well as with the ROS scavenger N-acetyl-cysteine (NAC, 1 mM) for 20 hours. HepG2 cells were cultivated in DMEM (Life Technologies) containing 4.5 g/L glucose, supplemented with 10% FBS (Silantes, Munich, Germany), 1% PSN (Invitrogen), at 37 °C in a humidified atmosphere of 5% CO<sub>2</sub>. Cells were split into 6-well plates (9 cm<sup>2</sup>) and grown to full confluence. After treatment, cells were incubated with either 2 µM HE, mito-HE, or HPr<sup>+</sup> for 30 min at 37 °C in biological triplicates.

Cells were washed with ice-cold phosphate-buffered saline twice and immediately lysed in 200 µL ice-cold phosphate-buffered saline containing 0.1% Triton X-100. The cell

suspensions were transferred into 1.5-ml black tubes to avoid light exposure and placed on ice for further disruption by shear forces induced by 10 repeated injections through a 26G cannula. The homogenates were centrifuged for 5 min at 600 g at 4°C. Supernatants (50 µL) were mixed with 200 µL acetonitrile and 20 µL 1 mM internal standard (chloramphenicol) and placed on a shaker (800 rpm) to allow protein precipitation for 5 min at 4°C. The protein precipitate was pelleted by centrifugation at 20,000 g for 10 min at 4 °C, and the resulting supernatant was used for LC-MS/MS analysis.

#### **2.12.5 LC-MS/MS settings for ROS probes and oxidative products quantification**

The supernatant (20 µL) was injected and compounds were separated on an LC instrument (1290 series UHPLC; Agilent), coupled online to a triple quadrupole hybrid ion trap mass spectrometer QTrap 6500 (Sciex). All transitions and compound-specific settings are shown in Table 9. Data acquisition was performed with an ion spray voltage of 5.5 kV in the positive mode for the electrospray ionization source, N<sup>2</sup> as the collision gas was set to medium, the curtain gas was at 30 psi, the ion source gas 1 and 2 was at 50 and 70 psi, respectively, and the interface heater temperature was set to 350 °C.

### **2.13 Data evaluation and Statistical Rationale**

The metabolite identification in all experiments was based on three levels: (i) the correct retention time, (ii) three transitions, (iii) and matching MRM ion ratios of tuned pure metabolites as described previously (Gielisch and Meierhofer 2015). Peak integration was performed using MultiQuant™ software v.2.1.1 (Sciex). All peaks were reviewed manually and adjusted if necessary. The peak area of the first transition per metabolite was used for subsequent calculations. An internal standard was used to normalize all LC-MS/MS runs for instrumental variations.

For the proteome and metabolome data sets, a two-sample t-test was performed. Multiple test correction was done by Benjamini-Hochberg with an FDR of 0.05 by using Perseus (v1.6.0.2) (Tyanova, Temu et al. 2016). Significantly regulated proteins and metabolites were marked by a plus sign in the corresponding Supplemental Tables S2 and S3. The Mann–Whitney *U* test was used to determine whether GSH levels from independent urine and plasma samples have the same distribution; the *p*-value significance cut-off was ≤ 0.01.

## Materials and methods

### 2.14 Data availability

The datasets generated in the current study are available as supplementary files and in the following repositories:

The WES raw files can be accessed via <https://www.ncbi.nlm.nih.gov/sra> with the accession number: PRJNA413158.

Proteomics raw data have been deposited to the ProteomeXchange Consortium via the Pride partner repository (Vizcaino, Cote et al. 2013) with the dataset identifier PXD010391.

Metabolomics data have been deposited in the publically available repository PeptideAtlas with the identifier PASS01250 and can be downloaded via <http://www.peptideatlas.org/PASS/PASS01250>.

Mass spectrometry data of the ROS measurement method development have been deposited into the publicly accessible repository PeptideAtlas under the identifier PASS01157.



## Results

### 3. Results

To comprehensively understand the characteristics of chRCC, two systematic omics approaches, mass spectrometry-based proteome, and metabolome profiling in nine chRCC and adjacent healthy kidney tissues were employed (Figure 10). In order to verify the correct diagnosis of all the chRCC cases, copy number variations (CNV) were retrieved from the whole-exome sequencing (WES) data (Xiao, Clima et al. 2019), the typical monosomies of chromosomes 1, 2, 6, 10, 13, 17, and 21 were identified in all cases (Figure 11), conforming to previous reports (Brunelli, Eble et al. 2005, Haake, Weyandt et al. 2016, Casuscelli, Weinhold et al. 2017).

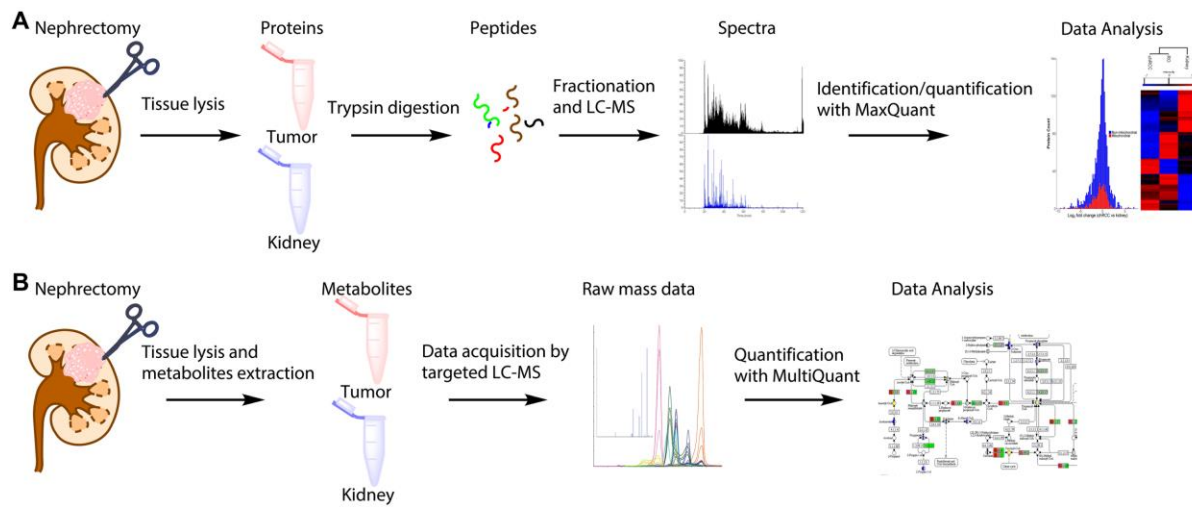


**Figure 10. The proteome and metabolome profiling workflow of chRCC.**

(A) The proteome workflow involves tissue lysis of the tumor and kidney samples, followed by protein digestion with trypsin, peptide fractionation, analysis on the LC-MS and label-free quantification. (B) The metabolomics workflow involves tissue lysis of the tumor and kidney samples, metabolite extraction, followed by data acquisition by a targeted LC-MS approach and relative quantification of the peaks.

#### 3.1 Proteome profiling of chRCC

A total of 26,839 peptides and 3,575 proteins were identified in chRCC samples and adjacent healthy kidney tissues from ten patients, both at a false discovery rate (FDR) of 1%. 56.9% (2,034) of these proteins were quantified in at least six out of nine samples. Between different samples, the values of Pearson correlation coefficient ranged from ranging from 0.659 to 0.921 in chRCC and 0.770 to 0.955 in kidney tissues. (Figure 12A). A principal component analysis (PCA) of the proteome data revealed that the first component separated between the chRCC specimen and kidney tissues, but with some outliers (C4,

K9; Figure 12B). These results indicate a higher variability within tumor samples, most likely due to the differences in micro-environmental conditions or the heterogeneity of the tumors. A t-test with Benjamini-Hochberg (BH) correction ( $FDR < 0.05$ ) for multiple testing was performed to identify significantly altered proteins between chRCC and controls. Altogether 983 significantly regulated proteins were identified, 390 proteins were significantly up- and 593 were down-regulated in chRCC (Figure 12C, Supplemental Table S2). Among these significantly changed proteins, fructose-1,6-bisphosphatase (FBP1), which was shown to oppose clear cell RCC (ccRCC) progression (Li, Qiu et al. 2014), decreased more than 28-fold in the tumor. Phospholipase C gamma 2 (PLCG2), was over 74-fold increased in chRCC, these high transcript expression levels had been considered as a potential biomarker for chRCC (Durinck, Stawiski et al. 2015). Thus, the proteomic analysis can verify known molecular signatures of RCC and serve as a source for subsequent computational analyses.

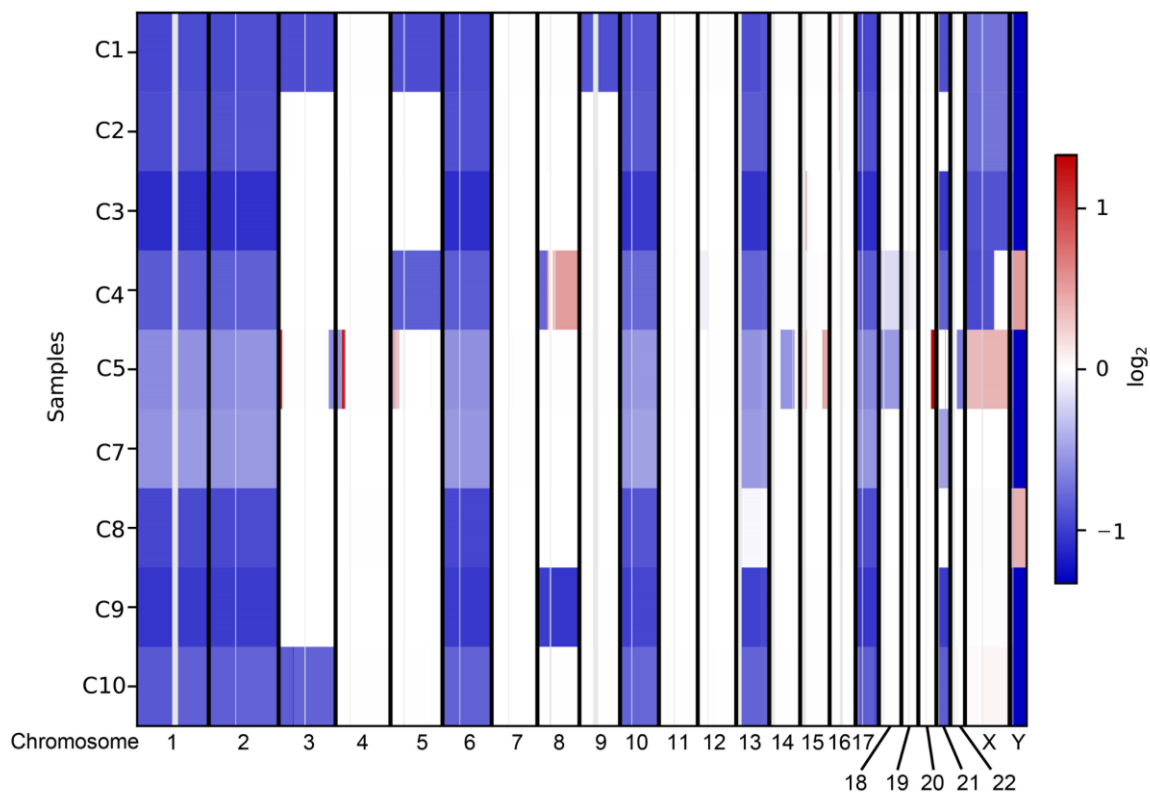


**Figure 11. Exome-based copy number variation analysis in chRCC.**

chRCC specific monosomies of chromosomes 1, 2, 6, 10, 13, 17, and frequently of 21 were identified in all cases.

## Results

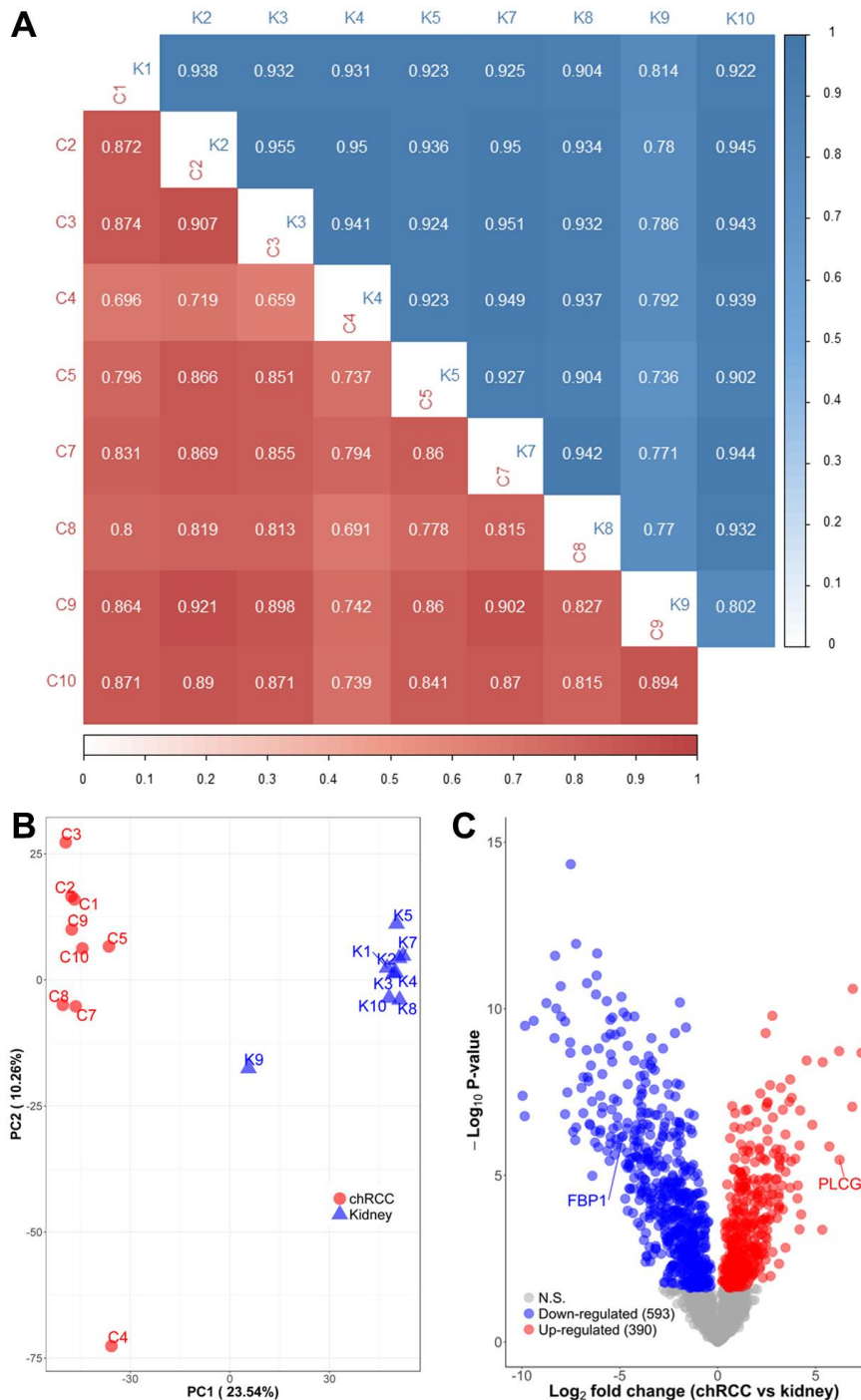


**Figure 12. The proteomic analysis of chRCC**

(A) Pearson correlation within the chRCC samples and kidney tissues. (B) A principal component analysis (PCA) of the proteome data revealed some outliers. (C) A volcano plot of log<sub>2</sub> abundance ratios of chRCC versus kidney tissues ( $n = 9$ ) against the -log<sub>10</sub> (p-value) of the proteome. Altogether 390 proteins were significantly up-regulated and are shown in red; 593 proteins were significantly down-regulated, as shown in blue. N.S., not significant.

A gene set enrichment analysis (GSEA) (Subramanian, Tamayo et al. 2005) was employed to assess whether an *a priori* defined set of proteins show statistically significant, concordant differences between chRCC and healthy kidney tissues. GSEA revealed several significantly ( $p \leq 0.01$  and FDR  $\leq 0.05$ ) regulated Kyoto Encyclopedia of Genes and Genomes (KEGG) pathways in chRCC versus healthy tissues (Figure 13, Table 10, Table 11). The up-regulated pathways included the proteasome, ubiquitin-mediated proteolysis, the lysosome, and phagocytosis, in chRCC compared with normal tissue (Figure 13, Table 10). In contrast, pathways involved in energy supply chains and nutrition homeostases, such as lipid metabolism, GSH metabolism, the peroxisome, glycolysis and gluconeogenesis, and amino acid metabolism pathways were significantly down-regulated in chRCC (Figure 13, Table 11).

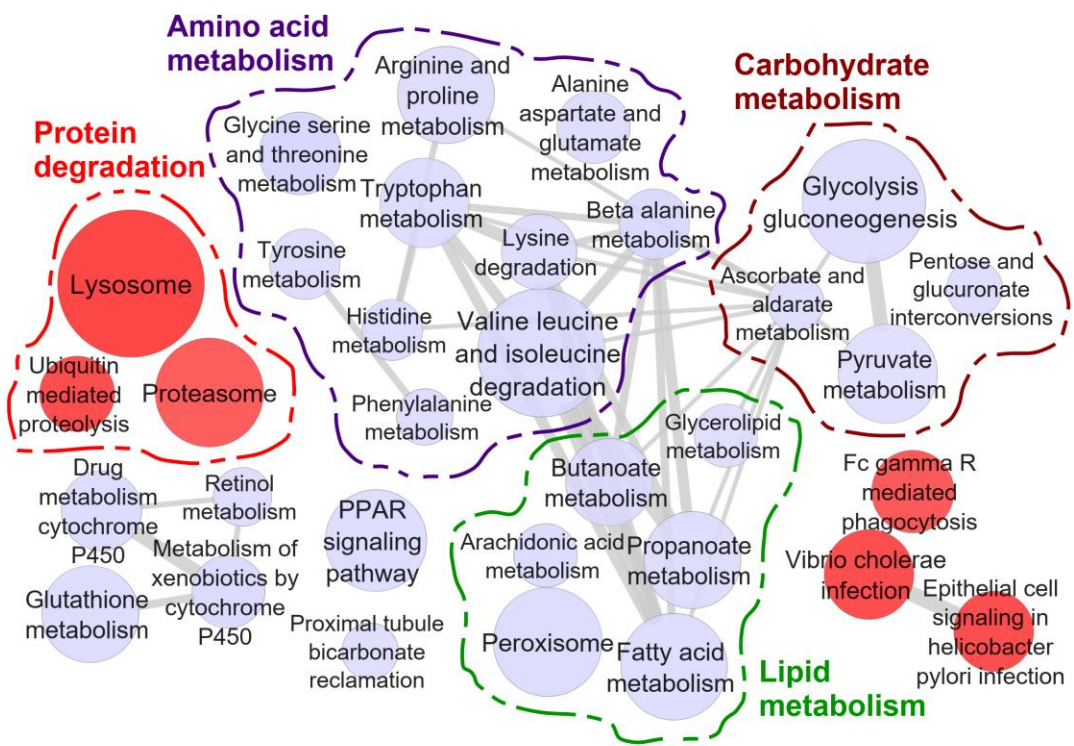


**Figure 13. Gene set enrichment analysis of the proteome revealed regulated pathways in chRCC.**

Protein pathway analysis of chRCC versus kidney controls. Indicated are significantly ( $p \leq 0.01$  and FDR  $\leq 0.15$ ) enriched (red) and decreased (blue) KEGG pathways in chRCC. Grey lines connect overlapping pathways. Similar pathways are circled by a dotted line, such as decreased amino acid-, lipid-, carbohydrate metabolism, and increased protein degradation.

## Results

**Table 10. Gene set enrichment analysis of the chRCC proteome, listed are significantly upregulated pathways in chRCC.**

KEGG pathway	size	p-value	q-value
Lysosome	48	0.00	0.01
Vibrio cholerae infection	24	0.00	0.01
Ubiquitin mediated proteolysis	18	0.00	0.01
FC gamma r mediated phagocytosis	21	0.00	0.02
Proteasome	32	0.00	0.02
Epithelial cell signaling in helicobacter pylori infection	20	0.00	0.01

**Table 11. Gene set enrichment analysis of the chRCC proteome, listed are significantly downregulated pathways in chRCC.**

KEGG pathway	size	p-value	q-value
Glycine serine and threonine metabolism	21	0.00	0.00
Beta alanine metabolism	16	0.00	0.00
Metabolism of xenobiotics by cytochrome P450	17	0.00	0.00
Valine leucine and isoleucine degradation	40	0.00	0.00
Peroxisome	32	0.00	0.00
Drug metabolism cytochrome P450	20	0.00	0.00
PPAR signaling pathway	29	0.00	0.00
Arachidonic acid metabolism	13	0.00	0.00
Tryptophan metabolism	24	0.00	0.00
Glutathione metabolism	27	0.00	0.00
Histidine metabolism	12	0.00	0.00
Fatty acid metabolism	31	0.00	0.00
Phenylalanine metabolism	10	0.01	0.01
Tyrosine metabolism	16	0.00	0.01
Ascorbate and aldarate metabolism	10	0.00	0.01
Pentose and glucuronate interconversions	10	0.01	0.01
Glycolysis gluconeogenesis	38	0.00	0.01
Butanoate metabolism	23	0.00	0.01
Alanine aspartate and glutamate metabolism	17	0.01	0.01
Lysine degradation	18	0.00	0.01
Retinol metabolism	11	0.00	0.02
Arginine and proline metabolism	27	0.01	0.02
Propanoate metabolism	27	0.01	0.02
Proximal tubule bicarbonate reclamation	10	0.01	0.02
Glycerolipid metabolism	13	0.03	0.04
Pyruvate metabolism	28	0.02	0.05

### 3.2 Metabolome profiling of chRCC

Metabolite identification was based on three very strict criteria to exclude false-positive result, (i) the correct retention time, (ii) up to three MRM s, and (iii) a matching MRM ion peak ratio of tuned pure metabolites as a reference (Gielisch and Meierhofer 2015). Targeted metabolome profiling, targeting a panel of 366 metabolites, was performed in chRCC. 144 metabolites were identified and relatively quantified (Figure 14, Supplemental Table S3). A statistical analysis using a two-sample t-test with the BH (FDR of 0.05) correction for multiple testing revealed 28 significantly ( $p$ -value  $<0.01$ ) regulated metabolites (19 down-, 9 up-regulated) in chRCC versus kidney tissues (Figure 14). The top three significantly up-regulated metabolites are all related to GSH metabolism (including both oxidized and reduced GSH, the GSH precursor gamma-glutamylcysteine; Figure 14, Supplemental Table S3), consistent with a previous study performed in chRCC (Priolo, Khabibullin et al. 2018). Interestingly, a similar pattern was also reported in other RCC subtypes, including ccRCC (Hakimi, Reznik et al. 2016), pRCC (Al Ahmad, Paffrath et al. 2019), and RO (Kurschner, Zhang et al. 2017, Gopal, Calvo et al. 2018), thus the up-regulation of GSH has been proposed as a hallmark of kidney cancer and can be exploited as a specific treatment strategy (Xiao and Meierhofer 2019).

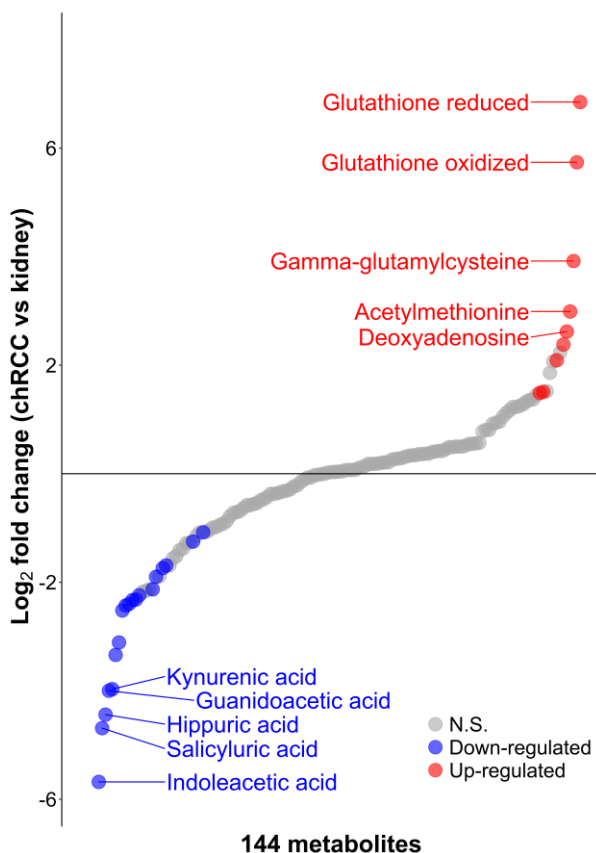


**Figure 14. Quantified metabolites by targeted metabolome profiling of chRCC.**

The distribution of fold changes of 144 metabolites in this cohort ( $n=9$ ) of chRCC versus kidney tissues. Significantly (FDR  $<0.01$ ) up-regulated and down-regulated metabolites are shown in red and blue, respectively. N.S., not significant.

## Results

### 3.3 Proteomic analysis reveals the downregulation of OXPHOS in chRCC

The loss of CI and consequently the compensatory increase of the other OXPHOS complexes are the main molecular hallmarks of RO (Simonnet, Demont et al. 2003, Mayr, Meierhofer et al. 2008, Kurschner, Zhang et al. 2017, Gopal, Calvo et al. 2018) The proteome data were used to explore, whether chRCC also has similar impaired mitochondrial features. A general decrease of subunits involved in all OXPHOS complexes was observed in chRCC relative to the normal kidney, predominantly affecting CI subunits (Figure 15A). The average  $\log_2$  fold change ( $\log_2 FC$ , chRCC VS kidney) was -1.79 for CI, -1.05 for CII, -0.91 for CIV, -0.57 for CV, and only CIII was unchanged (-0.03) (Figure 15A). A comparison with the proteome data of RO (Kurschner, Zhang et al. 2017) revealed that only CI subunits were similarly downregulated in both tumors, whereas the protein abundance of all other OXPHOS complexes was increased in RO, but decreased in chRCC (Figure 15B). It is worth noting that the mitochondrial mass accumulation, a histological hallmark of RO, was consistently reflected by an allocation analysis of the proteome data, as the mitochondrial proteins show an obvious shift towards the upregulation direction (Figure 15D). This result further confirmed the complete loss of CI in RO, considering that the accumulated mitochondrial mass should lead to an increase of all the constituting mitochondrial proteins. However, the allocation analysis of the chRCC proteome did not show any remarkable shift of the mitochondrial proteins (Figure 15C), which indicates the chRCC cases in this cohort did not have the mitochondrial accumulation feature, thus the downregulation of OXPHOS did not result from the alteration of mitochondrial amount in chRCC relative to normal kidney.

The proteomic analysis of chRCC and comparison with RO revealed a significant diminishment of CI in both tumors, whereas an opposite regulation of the other OXPHOS complexes, upregulated in RO, but downregulated in chRCC. Such distinct regulation of OXPHOS has the potential to be developed as a diagnostic marker for distinguishing chRCC and RO.

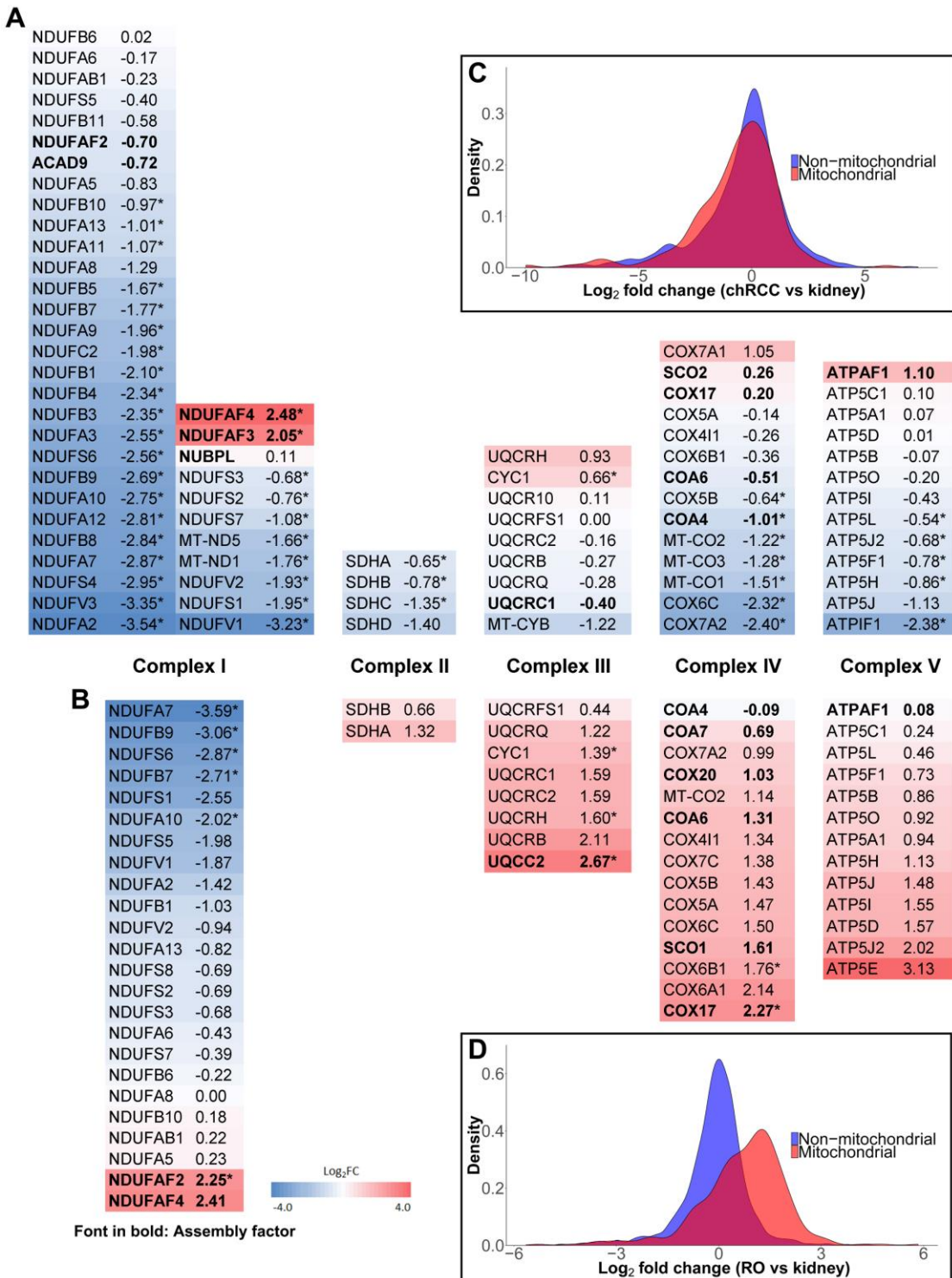


**Figure 15. Distinct regulation of the OXPHOS complexes in chRCC and RO.**

Comparison of protein abundance ratios ( $\log_2$ ) of all OXPHOS subunits between (A) chRCC and (B) RO samples versus healthy controls. Displayed are the five OXPHOS complexes, including all quantified subunits and assembly factors and the corresponding  $\log_2$  fold changes between chRCC

## Results

and RO (Kurschner, Zhang et al. 2017) versus adjacent healthy kidney samples, respectively. The color gradient of the subunits reflects a low (blue) or high (red) abundance of this protein in the tumor. The abundances of CI subunits were the most decreased in chRCC and RO, whereas all other OXPHOS complexes were increased in RO, but generally showing a low abundance in chRCC. Assembly factors (fond in bold), not part of the final complex, were increased in both tumor types. The symbol \* indicates significantly (FDR  $\leq 0.05$ ) regulated proteins. (C) The density plot shows the density of mitochondrial and non-mitochondrial protein counts versus the  $\log_2$  fold changes of proteins comparing chRCC versus kidney samples. (D) The density plot shows the density of mitochondrial and non-mitochondrial proteins versus the  $\log_2$  fold changes of proteins comparing RO versus kidney samples. Proteins located in mitochondria are indicated in red (Human Mito Carta, 1158 entries (Calvo, Clauser et al. 2016), whereas non-mitochondrial proteins are shown in blue.

### 3.4 ChRCC display a discrepancy between the abundance of genes coding for- and the proteins involved in the respiratory chain

Contrary to the decreased abundance of proteins involved in OXPHOS complexes identified by proteome profiling, the transcriptome analysis of chRCC (KICH data set from TCGA) found high expression patterns associated with the electron transport chain genes (Davis, Ricketts et al. 2014, Ricketts, De Cubas et al. 2018). A gene set enrichment analysis (GSEA) (Subramanian, Tamayo et al. 2005) of all quantified proteins showed a negative enrichment score (-0.36) of the KEGG pathway “oxidative phosphorylation” (Figure 16A), but a positive enrichment score (0.47) when analyzing with the transcriptome data (Figure 16B). Therefore, a correlation analysis of the proteome and transcriptome data was performed and a high overall correlation between the proteins and transcripts with a Pearson’s correlation coefficient of 0.671 was found (Figure 16C). However, the protein abundances of OXPHOS subunits were identified to have a poor correlation with their corresponding RNA expression with a Pearson correlation coefficient of 0.196 (Figure 16C).

To validate the biological significance of the contradictory regulation between the transcriptome and proteome, the enzymatic activities of all respiratory chain complexes and citrate synthase (CS) were measured and the activities were compared for chRCC and the adjacent matching healthy tissues. This analysis revealed a significant reduction in the enzyme activities of CI, CII, CIV, and CV in chRCC, whereas CIII was unchanged and the activity of the TCA cycle enzyme CS was significantly increased (Figure 16D-I).

Thus, the enzymatic activities of the respiratory chain reflect the abundance of protein rather than the expression of RNA transcripts. The TCA cycle, which is involved in many different metabolic pathways, seems to be regulated by a different mechanism since CS was

significantly increased in chRCC. Nevertheless, the abundance of “energy carriers”, such as NAD<sup>+</sup>, NADH, NADP, ATP, and ADP was unchanged (Supplemental Table S3).

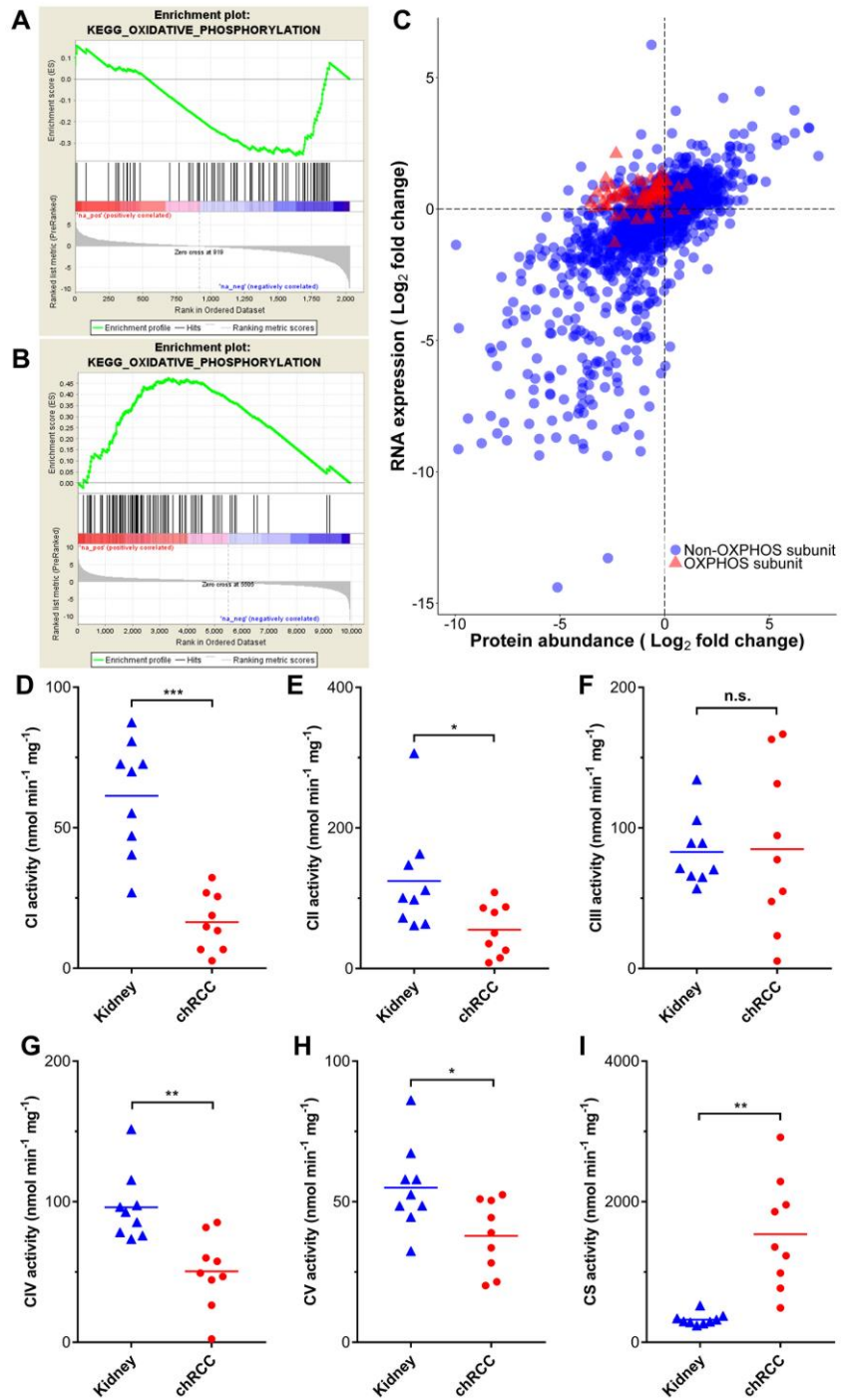


**Figure 16. Comparison of the RNA expression versus the protein abundance between chRCC and kidney controls.**

A pathway analysis (GSEA) shows the down-regulation of OXPHOS on the proteome level (this study) (A) and an up-regulation on the transcript level (TCGA data, B). (C) Plotted are all non-

## Results

OXPHOS transcripts versus proteins as log<sub>2</sub> fold changes (blue dots) and specific entities involved in OXPHOS (red triangles), which display the discrepancy between the expression of transcripts and protein abundance. RNA data were retrieved from TCGA. (D to H) Enzyme activities (nmol/min/mg protein, n = 9) of the OXPHOS complexes in chRCC were compared with kidney controls. (D) Complex I (CI), (E) Complex II (CII), (F) Complex III (CIII), (G) Complex IV (CIV), (H) Complex V (CV), and (I) citrate synthase (CS). P-values in (D-I) are \*P < 0.05, \*\*P < 0.01, and \*\*\*P < 0.001 by paired t-test. n.s., not significant.

### 3.5 ChRCC are characterized by an increased level of GSH and reduced protein abundance of GSH degrading enzymes

Reactive oxygen species (ROS), acting as a double-edged sword in cancer cells, are mainly produced within the respiratory chain in a cell, predominantly by CI and CIII (Chen, Vazquez et al. 2003, Li, Ragheb et al. 2003). The main intercellular ROS scavenger GSH and its related metabolites boosted in RO as an adaptive event following the loss of CI (Kurschner, Zhang et al. 2017, Gopal, Calvo et al. 2018). Similarly, the top three increased metabolites in chRCC were all involved in GSH metabolism, including GSH (115-fold), glutathione disulfide (GSSG, 54-fold), and  $\gamma$ -glutamylcysteine (15-fold; Figure 17A-C, Supplemental Table S3). Case-specific GSH/GSSG ratios were found to be increased in all chRCC samples, except for case 4 (Figure 17D). This indicates a reduced oxidative stress burden in most chRCC cases, created by at least a hundredfold higher GSH and GSSG levels in chRCC compared with the kidney. In contrast to the significantly increased GSH-related metabolites, the GSH metabolism pathway was found significantly (p ≤ 0.005) reduced by the GSEA analysis of the chRCC proteome data (Figure 13, Table 11). This was mainly due to decreased levels (average 42-fold) of GSH degrading and conjugating enzymes, such as GGT1, GGT5, GSTM2, GSTM3, GSTA1, ANPEP as well as GPX3 (Figure 17E), which catalyzes the reduction of hydrogen peroxide. However, the two key enzymes involved in GSH synthesis (GSS, GCLC) were not significantly changed, other GSH related enzymes, the GSH peroxidases (GPX1, GPX4), the GSH S-transferases (GSTO1, GSTP1), and the GSH reductase (GSR), all remained unchanged or insignificantly increased at a neglected level (Figure 17E). Therefore, the boosted level of GSH-related metabolites in chRCC is due to significantly reduced abundance levels of proteins involved in GSH degradation, rather than an increased GSH synthesis rate.

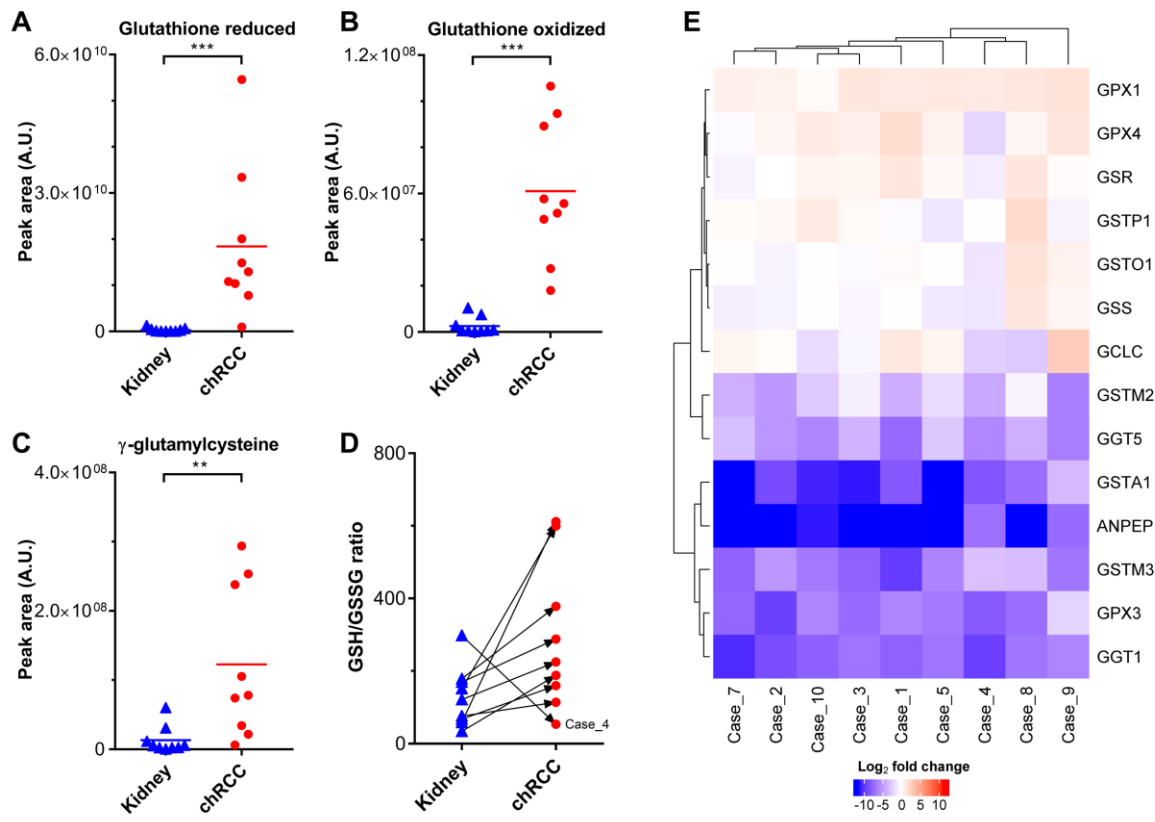


**Figure 17. The level of glutathione boosted in ChRCC.**

Relative abundances of metabolites involved in the glutathione metabolism are shown for normal kidney samples and chRCC. (A) Reduced glutathione, (B) Oxidized glutathione, and (C)  $\gamma$ -glutamylcysteine. (D) GSH/GSSG ratio was calculated with the relative signal intensities. (E) Heatmap of all the quantified proteins involved in glutathione metabolism in chRCC, the color gradient of the proteins indicates a low (blue) or high (red) log<sub>2</sub> fold change of this protein in chRCC versus normal kidney tissues. P-values in (A) to (C) are \*\*P < 0.01, and \*\*\*P < 0.001 by two-tailed Student's t-test. A.U., arbitrary units.

In a pilot study, the free and total GSH levels in plasma and urine of ccRCC, pRCC, chRCC, and RO specimens were further analyzed to elucidate whether GSH can be used as a non-invasive diagnostic marker. The results clearly indicated that free (Figure 18 A, C) and total (Figure 18 B, D) GSH did not show significantly different levels in these tumors and thus cannot serve as a non-invasive metabolic marker to distinguish between renal tumor types and healthy individuals in urine and plasma.

## Results

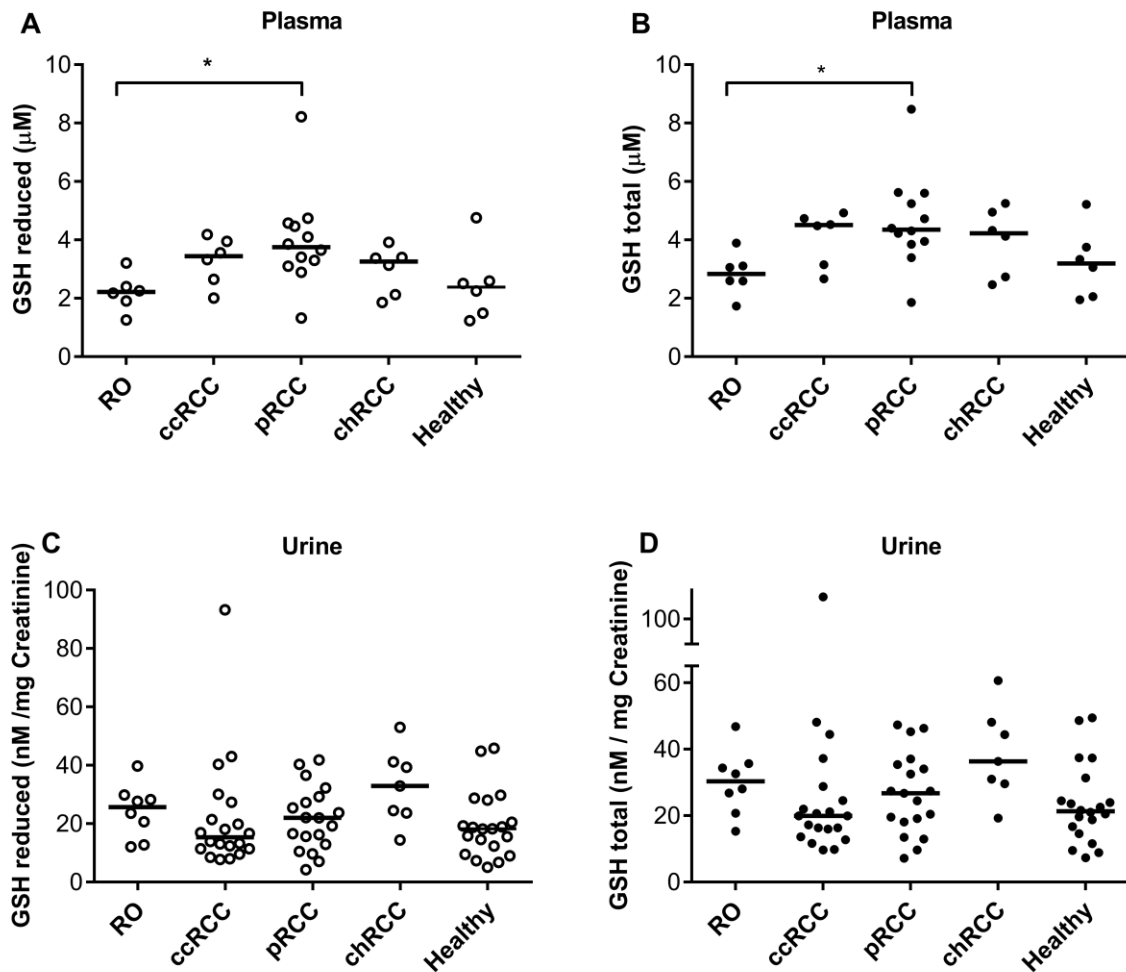


**Figure 18. Glutathione levels in plasma and urine cannot be used as a marker to distinguish RCCs from controls.**

The free and total GSH levels in plasma (A, B; 6 RO, 6 ccRCC, 12 pRCC, 6 chRCC, and 6 healthy) and urine specimens (C, D; 8 RO, 20 ccRCC, 19 pRCC, 7 chRCC, and 20 healthy) specimens were measured. Urine samples were normalized to creatinine.  $P$ -values are \* $P < 0.01$  by Mann–Whitney U test.

### 3.6 The decrease of mtDNA content other than CI mutations may lead to a malfunction of OXPHOS in chRCC

To examine whether mtDNA mutations are the main cause of the OXPHOS dysfunction in chRCC, as observed in RO (Simonnet, Demont et al. 2003, Gasparre, Hervouet et al. 2008, Mayr, Meierhofer et al. 2008, Kurschner, Zhang et al. 2017, Gopal, Calvo et al. 2018), I investigated the assembly of mitochondrial whole-exome sequencing (WES) reads to

identify somatic and germline mtDNA mutations in chRCC by pairwise comparison of tumor and healthy tissues. Adequate coverage (>99.9%) and quality for reliable mtDNA reconstruction and variant calling were found (Supplemental Table S5). Five somatic non-synonymous events were identified with a high disease score (>0.7), which are potentially pathogenic (Figure 19A, Supplemental Table S5), with four events involving CI genes from four cases and one event involving CIV. Case 4, the only case with a lower GSH/GSSG ratio, harbored the somatic mutation in *MT-ND5* (>60% heteroplasmy), this mutation might lead to inactivation of the associated protein based on the previous functional studies in RO (Simonnet, Demont et al. 2003, Gasparre, Hervouet et al. 2008, Mayr, Meierhofer et al. 2008, Kurschner, Zhang et al. 2017, Gopal, Calvo et al. 2018). Considering the other events were present at very low heteroplasmic rate (2 events below 30% and the other 2 around 5%) (Figure 19A, Supplemental Table S5), and the other chRCC cases did not present any non-synonymous CI mutations (Supplemental Table S5), this result suggests that there might be other mechanisms leading to the dysfunctional OXPHOS complexes and boosted GSH level besides the loss-of-function mutations in CI in RO and some chRCC cases.

The  $\rho^0$  cells, which are cells entirely depleted of mtDNA, showed a severe reduction of all proteins involved in the respiratory chain (Aretz, Hardt et al. 2016). Furthermore, lower mtDNA copy was observed in chRCC previously (Meierhofer, Mayr et al. 2004), thus a decrease in mtDNA copy might be directly related to the abundance decrease of OXPHOS subunits. Therefore, to access the mtDNA copy number in chRCC, the mtDNA reads between chRCC and controls were compared, as the read depth in a specific region of the genome is roughly proportional to the copy number of the DNA region. Indeed, a significant decrease (3-fold) of mtDNA read depth in chRCC relative to the normal kidney was identified (Figure 19B), indicating lower mtDNA content in chRCC compared with normal kidney. Based on these results, I proposed that the downregulation of the OXPHOS might be caused by the decreased mtDNA copy aside from CI mutations.

## Results

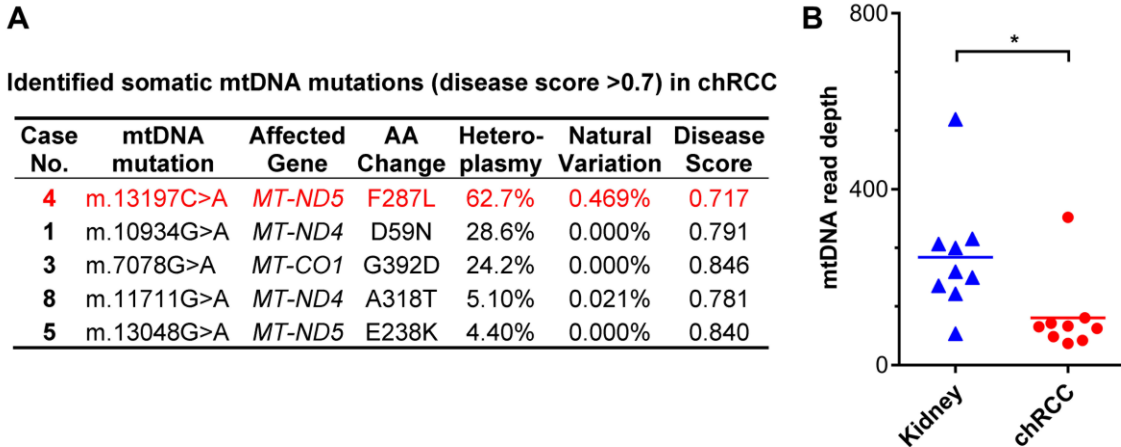


**Figure 19. Identified somatic mtDNA mutations and mtDNA copy number evaluation in chRCC.**

(A) Somatic mtDNA mutations with a high disease score (>0.7) were only found in five tumors, only the MT-ND5 mutation in case 4 has a relevant heteroplasmy rate. (B) The significantly decreased mtDNA read depth indicates a lower mtDNA copy number in chRCC compared to normal kidney (n = 9). P-values in (B): \*P < 0.05 by paired t-test.

### 3.7 A low mtDNA content causes the downregulation of OXPHOS subunits and elevation of GSH levels

To investigate the influence of mtDNA content on the OXPHOS complexes, the well-characterized chRCC cell line UOK276 (Yang, Vocke et al. 2017) was chronically exposed to a low dose of ethidium bromide (EtBr, 100 ng/ml) for 19 days to deplete the mtDNA (Yang, Vocke et al. 2017). During this process, the EtBr treated cells were carefully monitored and samples were collected on days 0, 2, 5, 8, 13, and 19 for the later analysis.

As expected, the mtDNA content in EtBr treated cells decreased dramatically within 5 days and reached p<sup>0</sup> status (mtDNA completely depleted) in 13 days (Figure 20A), demonstrating a successful p<sup>0</sup> cell line generation. Meanwhile, four OXPHOS subunits, MT-ND5 (CI, mtDNA-encoded), NDUFS1 (CI, nuclear-encoded), SDHB (CII), and UQCRC2 (CIII), representing different OXPHOS complexes and including both mtDNA and nuclear DNA coded subunits, were all downregulated in a time-dependent manner, and showed almost undetectable signals after 13 days (Figure 20B), indicating a direct correlation between the mtDNA depletion and the decrease of proteins involved in the respiratory chain. Metabolome profiling was applied to address the question, whether the GSH levels would also correlate to the mtDNA depletion series in the EtBr treated cells. Indeed, the GSH

levels increased remarkably throughout the mtDNA depleting process, reaching its plateau already on day 13 (Figure 20C). Interestingly, the corresponding transcripts of the four quantified OXPHOS subunits showed different expression patterns, divided into two categories. The nuclear-encoded transcripts NDUFS1, SDHB, and UQCRC2 showed a decreased expression in 8 days for NDUFS1 and in 13 days for the latter two but then started to increase after reaching their lowest levels (Figure 20D), not correlating to their protein levels (Figure 20B). Distinguishably, the mtDNA-encoded transcript MT-ND5, dropped strikingly in just 2 days without resurgence afterward (Figure 20D), matching consistently to its protein abundance (Figure 20B).

In conclusion, these results indicate that the decrease of the mtDNA content is the main cause of the OXPHOS impairment in chRCC. This leads to GSH elevation and a poor correlation between the proteins and transcripts of nuclear-encoded OXPHOS subunits, whereas the mtDNA-encoded subunit correlates nicely.

## Results

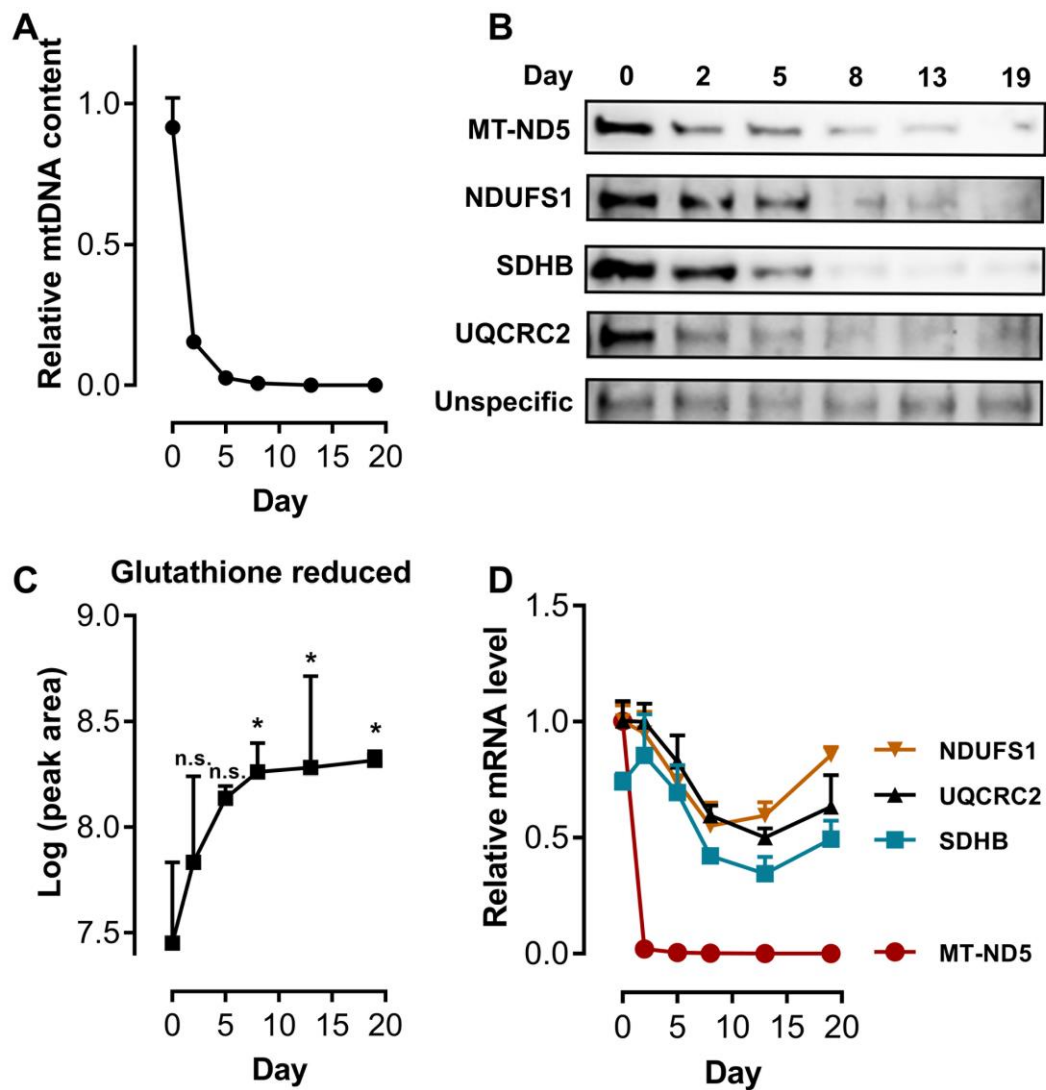


**Figure 20. Correlation between the mtDNA content with proteins and transcripts for the respiratory chain and glutathione levels.**

(A) The mtDNA content monitored over time during ethidium bromide (EtBr) treatment (100 ng/ml) in the chRCC cell line UOK276. These cells were used for all subsequent analyses. (B) Western blot analysis of the mitochondrial and nuclear-encoded OXPHOS subunits MT-ND5, NDUFS1, SDHB, and UQCRC2, showed a time-dependent abundance decrease. (C) The GSH level in chRCC cells increased and anti-correlated with the simultaneous decrease in the mtDNA content over time. (D) The nuclear DNA-encoded transcripts, NDUFS1, SDHB, and UQCRC2, initially decreased but started to increase after reaching their lowest points. The mtDNA-encoded transcript MT-ND5 dropped strikingly within 2 days, paralleling the level of mtDNA content without increasing again afterward. P-values in (C) are \*P < 0.05 by two-tailed Student's t-test. n.s., not significant.

### **3.8 Gluconeogenesis was completely stalled in chRCC**

The KEGG pathway “glycolysis and gluconeogenesis” was significantly reduced in chRCC (Figure 13, Table 11). This pathway describes two opposing metabolic functions: the generation of pyruvate from glucose and vice versa. Thus, a more detailed view of each metabolic pathway showed that the abundance of all glycolytic enzymes were either unchanged or slightly increased, whereas all enzymes solely involved in gluconeogenesis were greatly reduced in chRCC, such as PC (124-fold), PCK1 (96-fold), PCK2 (996-fold), ALDOB (922-fold), and FBP1 (29-fold; Figure 21A). The two aldolase isoforms A and C, which were increased in chRCC, have a high affinity for fructose-1,6-bisphosphate (F-1,6-BP) to foster glycolysis, whereas the highly diminished isoform B has a low affinity for F-1,6-BP and hence converts the back-reaction from glyceraldehyde-3-phosphate to F-1,6-BP (Penhoet, Rajkumar et al. 1966). Furthermore, the decreased PC, which is the main entry point for pyruvate to the TCA cycle, shows that the tumor relies on lactate fermentation, also indicated by significantly increased LDHA (3-fold) levels in chRCC. These are therefore the most relevant metabolic changes observed in the tumor and can be regarded as a hallmark of chRCC. A comparison with gene expression data, extracted from The Cancer Genome Atlas (TCGA) database (Davis, Ricketts et al. 2014), showed similar results, a significant depletion of transcripts coding for proteins involved in gluconeogenesis (Figure 21B-F).

## Results

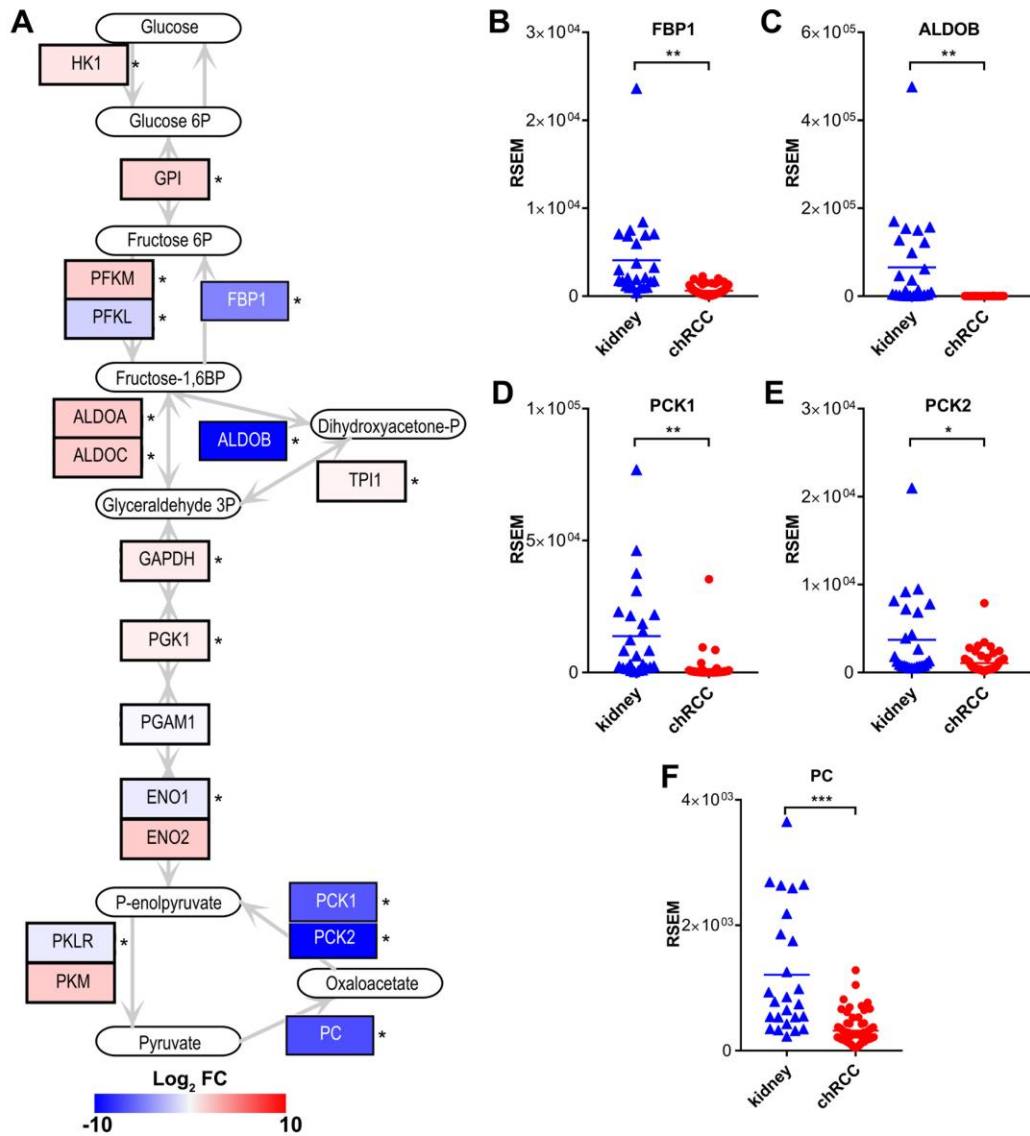


**Figure 21. Stalled gluconeogenetic pathway in chRCC.**

(A) Protein abundances of the metabolic pathways glycolysis and gluconeogenesis in chRCC. Log<sub>2</sub> fold changes are displayed between chRCC and kidney tissues, up-regulated proteins are shown in red and down-regulated proteins in blue. The symbol \* indicates significantly regulated proteins. (B-F) Transcript expression (TCGA) of gluconeogenic genes between chRCC (n= 66) and controls (n=25). (B) FBP1, fructose-1,6-bisphosphatase 1. (C) ALDOB, fructose-bisphosphate aldolase B. (D) PCK1, phosphoenolpyruvate carboxykinase, cytosolic. (E) PCK2, phosphoenolpyruvate carboxykinase, mitochondrial. (F) PC, pyruvate carboxylase. The data in (B-F) were calculated by RNA-Seq by Expectation Maximization (RSEM); \*P < 0.05, \*\*P < 0.01, \*\*\*P < 0.001 by a two-tailed student's t-test.

### **3.9 ChRCC feature a depletion of amino acid intermediates and pathways involved in amino acid metabolism**

On the proteome level, nine distinct pathways involved in amino acid metabolism were significantly down-regulated in chRCC (Figure 13 and Table 11). In total, 86 out of 101 proteins involved in amino acid metabolism showed a decreased abundance (average 22-fold). Altogether 15 proteins even decreased in abundance by over 40-fold (PHGDH, PSAT1, MAOB, DMGDH, SHMT1, BHMT, GATM, EHHADH, DPYS, ABAT, FTCD, DDC, ALDH4A1, ASS1, and AGMAT), indicating a major metabolic change (Figure 22A). In addition, five pathways associated with fatty acid metabolism were significantly down-regulated (Figure 13, Table 11), including fatty acid metabolism and the peroxisome, the main organelle for fatty acid oxidation.

The abundances of amino acid intermediates were found to be among the highest depleted metabolites in chRCC, matching the decreased protein abundances of amino acid pathways. These included guanidoacetic acid (intermediate of multiple amino acids, glycine, serine, threonine, arginine, and proline), kynurenic acid (tryptophan intermediate), indoleacetic acid (tryptophan intermediate), ureidopropionic acid (beta-alanine intermediate), hippuric acid (glycine intermediate), salicyluric acid (glycine intermediate) and acetylglutamine (glutamine intermediate), which were the most decreased metabolites in chRCC (Figure 22B-G, Supplemental Table S3). Interestingly, the level of glycine was not significantly decreased, but all of the other amino acids were either unchanged or slightly, but not significantly increased (Supplemental Table S3).

These data indicate a substantial change in the supply of nutrition in chRCC. The amino acid levels are within the normal range, but they originate from external sources through incorporation, rather than by the synthesis of classical precursors.

## Results

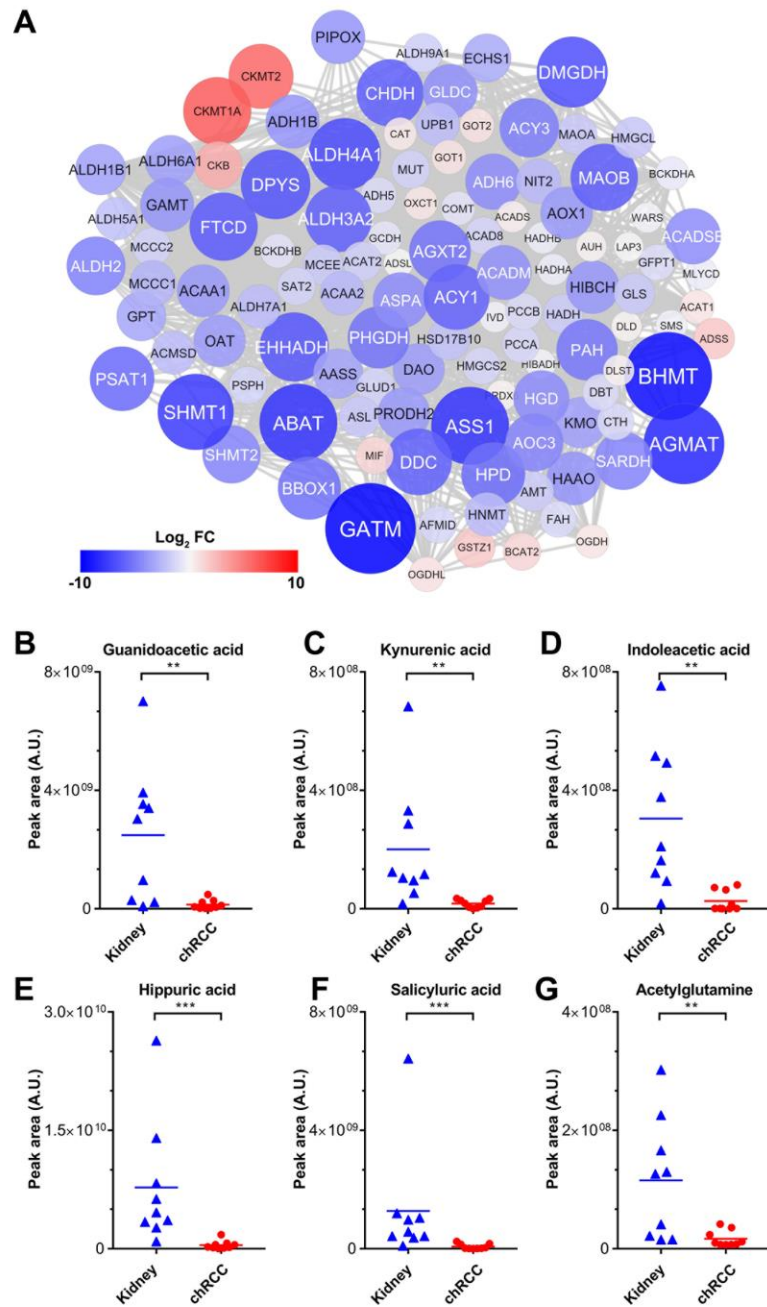


**Figure 22. Regulation of amino acid metabolism in chRCC.**

(A) A protein-protein interaction network was created to elucidate the regulation of the entire amino acid metabolism in chRCC. The colors of the nodes correspond to the protein expression fold change comparing chRCC versus healthy kidney tissues; red indicates higher expression and blue lower expression in chRCC. The size of the nodes corresponds to the absolute protein expression fold-change. (B-G) The relative abundance of six selected amino acid intermediates is shown for kidney tissues and chRCC. (B) Guanidoacetic acid. (C) Kynurenic acid. (D) Indoleacetic acid. (E) Hippuric

acid. (F) Salicyluric acid. (G) Acetylglutamine. P-values in (B) to (G) are: \*\*P < 0.001, \*\*\*P < 5e-4 by two-tailed Student's t-test. A.U., arbitrary units.

### **3.10 ChRCC cells feed on extracellular macromolecules via endocytosis**

Pathways related to amino acid metabolism were significantly downregulated in chRCC (Figure 13, Figure 22), whereas all detected amino acid levels were unchanged (Supplemental Table S3). Thus, I hypothesized that chRCC cells could preferentially internalize and catabolize external macromolecules as a source of amino acids. Indeed, a pathway related to endocytosis (Fc gamma R mediated phagocytosis) and three protein degradation pathways (lysosome, ubiquitin-mediated proteolysis, and proteasome) were significantly up-regulated in chRCC (Figure 13, Table 10). In particular, the two lysosome markers, LAMP1 and LAMP2, were up-regulated by 3 and 7-fold, respectively (Supplemental Table S2). Activated lysosomes indicate that the recycling of macromolecules and maintaining an acidic tumor microenvironment favors the viability and progression of chRCC. These metabolic changes indicate that extracellular biomass recruitment and protein degradation is the preferred way of gaining mass and nutrition in chRCC.

To further investigate, whether increased abundances of lysosomal proteins correlate with increased enzymatic activities in chRCC, the activities of two lysosomal enzymes were measured, hexosaminidase A and B. These enzymes are involved in the breakdown of gangliosides and were both found to be significantly increased in chRCC (Figure 23A-B).

Next, I asked, whether the supplementation of a macromolecule indeed enhances the growth rate of chRCC cells and whether this is mirrored by the alteration of protein abundances in endocytosis pathways. Therefore, the proliferation of the chRCC-derived cell line UOK276 (Yang, Vocke et al. 2017) and normal kidney cells (HK-2) under different amino acid and bovine serum albumin (BSA) concentrations were evaluated. Overall, both UOK276 and HK-2 cells grew significantly faster under all amino acid concentrations when supplemented with 2.5% BSA, only the UOK276 cells grew equally well when feeding with 10% amino acids (Figure 23C-D). UOK276 cells proliferated normally under a low amino acid concentration of 1% and the addition of 2.5% BSA, whereas HK-2 cells significantly reduced the growth rate. This result suggests that UOK276 cells have a higher potential to utilize BSA to compensate for the amino acid depletion. Proteome profiling between UOK276 cells supplemented with 1% amino acids and with the addition of 2.5% BSA versus a complete medium revealed a significant increase of the pathways endocytosis (transferrin

## Results

endocytosis and recycling, Reactome) and the lysosome (KEGG) (Figure 23E, Supplemental Table S6). Enzymatic activity measurement of the lysosomal hexosaminidases A and B of UOK276 cells between the before mentioned conditions further confirmed that external macromolecules triggered the internalization and the degradation pathways to break down macromolecules enzymatically via endocytosis (Figure 23F-G), which indicates the adaption of chRCC cells to nutrient-poor conditions. Hence, the experiments performed in the chRCC derived UOK276 cell line validated the observations gained for the chRCC tissues.

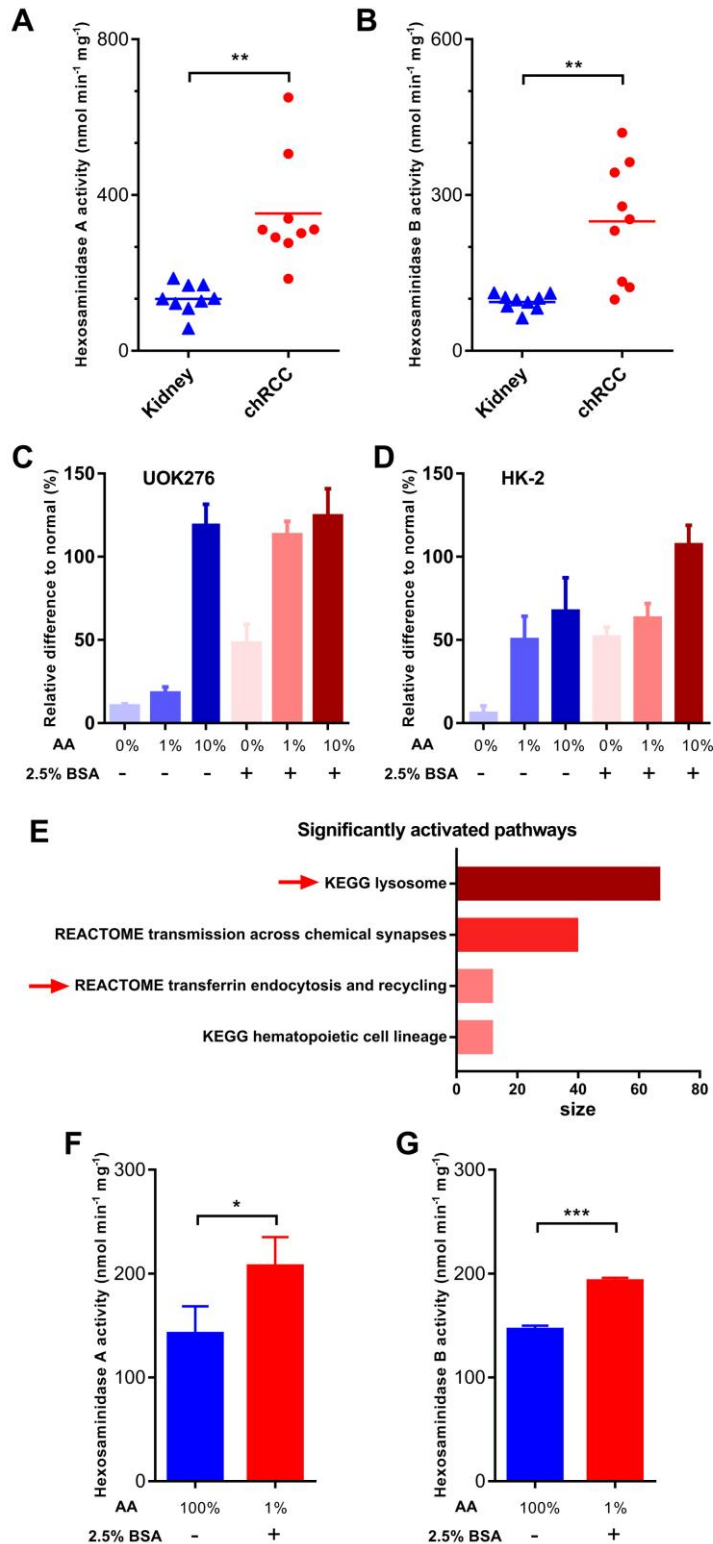


**Figure 23. ChRCC cells activated endocytosis when amino acids were depleted.**

(A-B) Enzymatic activities ( $\text{nmol/min/mg protein}$ ,  $n = 9$ ) of the hexosaminidase A (A) and B (B) in chRCC compared with kidney controls. (C-D) Relative cell numbers of UOK276 cells (C) and HK-2

## Results

cells (D) under different amino acid (AA) and bovine serum albumin (BSA) concentrations normalized to complete medium. (E) A pathway analysis (GSEA) of the proteome shows the up-regulation of the lysosome and endocytosis in UOK276 cells in 1% amino acid and 2.5% BSA versus a complete medium, enriched pathway cutoff,  $p < 0.01$ , FDR  $< 0.25$ . (F-G) Enzymatic activities (nmol/min/mg protein,  $n = 3$ ) of the hexosaminidase A (F) and B (G) in UOK276 cells in complete medium without supplementation of BSA and 1% amino acids with 2.5% BSA. The data in (C-D) and (F-G) are expressed as means  $\pm$  SD, p-values in (A-B) are: \*\* $P < 0.01$ , by paired t-test; P-values in (F-G) are: \* $P < 0.01$ , \*\* $P < 0.01$ , two-tailed Student's t-test.

### **3.11 Pharmaceutical inhibition of the PLCG/IP3/Ca<sup>2+</sup>/PKC pathway suppresses the endocytosis in chRCC**

Phosphatidylinositol phospholipase C gamma 2 (PLCG2) is a membrane protein which catalyzes the conversion of phosphatidylinositol 4,5-bisphosphate (PIP2) to inositol 1,4,5-trisphosphate (IP3) and diacylglycerol (DAG), IP3 further activate the IP3 receptor on the endoplasmic reticulum to release Ca<sup>2+</sup>, which further activate protein kinase C (PKC). The protein and RNA abundance of PLCG2 were found to be highly significantly upregulated in chRCC, relative to normal kidney tissues (Figure 24A). To investigate the role of PLCG2 and its downstream effector IP3/Ca<sup>2+</sup>/PKC pathway in endocytosis, I developed an LC-MS method by using isotope tracers (Figure 24B). First, cells are cultured for multiple generations in medium containing uniformly <sup>13</sup>C and <sup>15</sup>N-labeled amino acids (<sup>13</sup>C<sup>15</sup>N-AA) to completely label all the intracellular amino acids and proteins. Then, cells are switched to <sup>13</sup>C<sup>15</sup>N-AA medium supplemented with 2.5% unlabeled BSA. At this point, unlabeled BSA is then internalized and degraded in cells, unlabeled amino acids are released or stayed intracellularly for protein synthesis. By measuring the amount of the unlabeled essential amino acids within the medium and cells, it is possible to access the endocytosis level under different conditions or in different cell lines. Using this method, EIPA (a widely used endocytosis inhibitor), U73122 (a general inhibitor of PLCG), and 2-APB (an IP3R antagonist) were first applied to UOK276 cells, as shown in Figure 24C, leucine, and lysine, the two most abundant essential AAs in BSA, were both significantly decreased in the inhibitors treated cells, all the other essential AAs were also showed the same trends (Figure 25A). In addition, the abundance of leucine and lysine was also significantly deduced in UOK276 cells when using BAPTA-AM (a cell membrane-permeable Ca<sup>2+</sup> chelator) and bisindolylmaleimide I (a PKC inhibitor) (Figure 24D), the same decreases were observed in the other essential AAs (Figure 25B). Taken together, these results suggest that the PLCG/IP3/Ca<sup>2+</sup>/PKC pathway can regulate activation of endocytosis in chRCC cells.

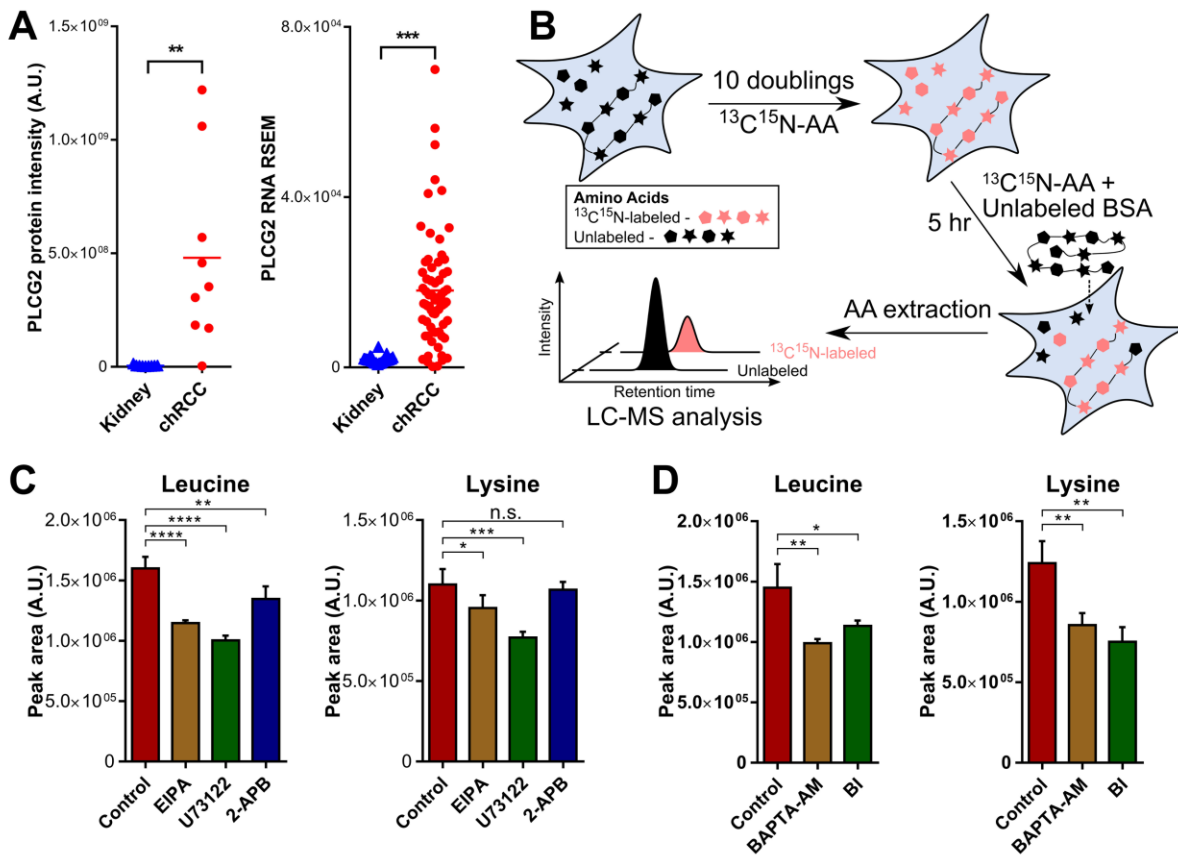


**Figure 24. Chemical inhibition of the PLCG pathway decreases the endocytosis of protein in chRCC cells.**

(A) Protein intensity and RNA RSEM plot show that the protein intensity and RNA abundance of PLCG2 are significantly increased in chRCC relative to normal kidneys. (B) The diagram of using isotope tracers to quantify protein scavenging by endocytosis with mass spectrometry. (C) The peak area plots of leucine and lysine after applying 10  $\mu\text{M}$  EIPA, 30  $\mu\text{M}$  U73122 and 100  $\mu\text{M}$  2-APB. (D) The peak area plots of leucine and lysine after applying 30  $\mu\text{M}$  BAPTA-AM and 3  $\mu\text{M}$  Bisindolylmaleimide I. P-values are: \*P < 0.05, \*\*P < 0.01, and \*\*\*P < 0.001 by two-tailed Student's t-test. A.U., arbitrary units.

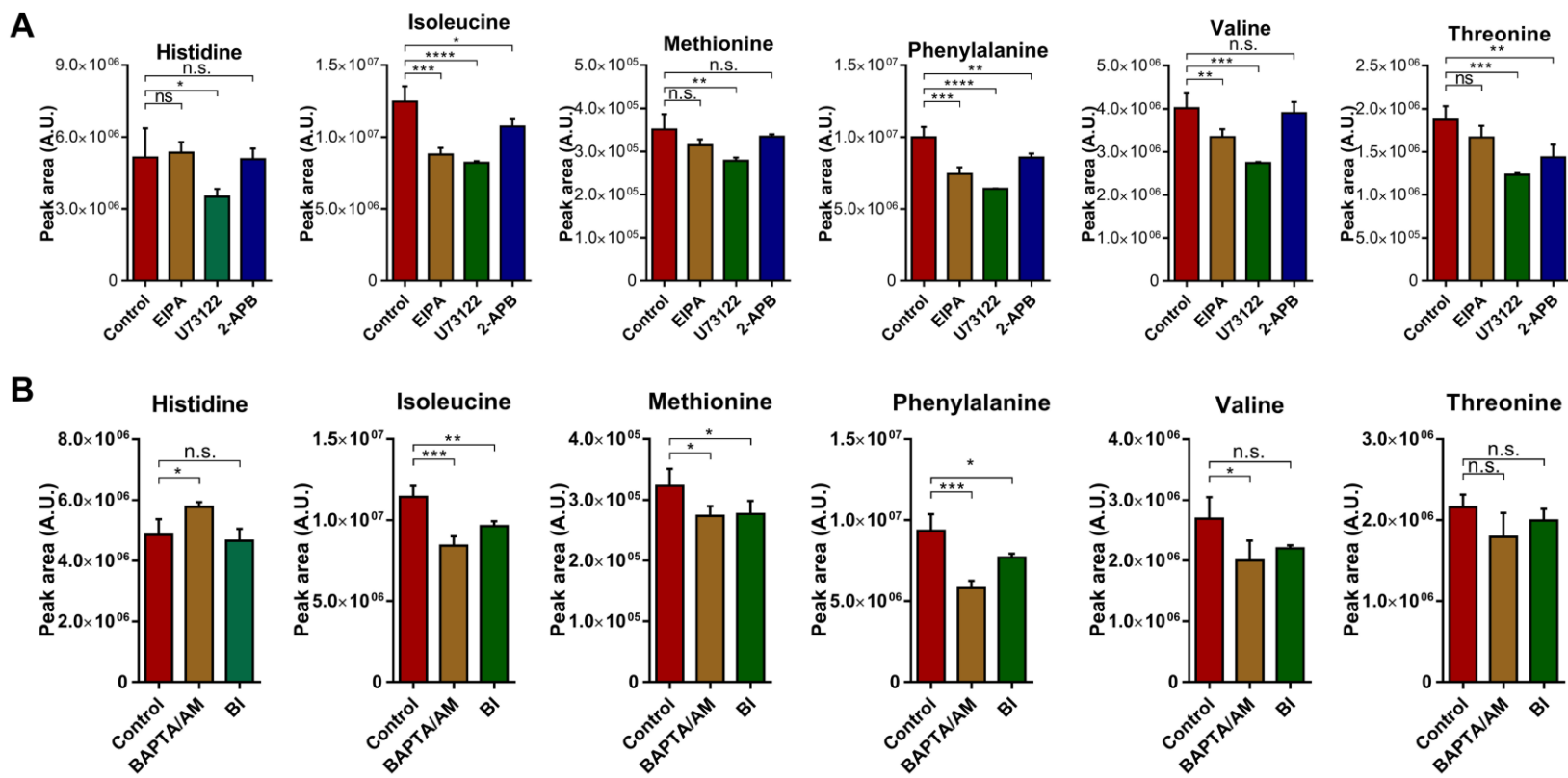


**Figure 25. Other unlabeled essential amino acids also decrease after chemical inhibition of the PLCG pathway.**

(A) The peak area plots of other unlabeled essential amino acids after applying 10  $\mu$ M EIPA, 30  $\mu$ M U73122 and 100  $\mu$ M 2-APB. (B) The peak area plots of other unlabeled essential amino acids after applying 30  $\mu$ M BAPTA-AM and 3  $\mu$ M Bisindolylmaleimide I. P-values are: \*P < 0.05, \*\*P < 0.01, and \*\*\*P < 0.001 by two-tailed Student's t-test. A.U., arbitrary units. n.s., not significant.

### **3.12 The hydroethidine-based probes for ROS measurement have high autoxidation rates**

#### **3.12.1 Establishment of an MRM-based method to monitor HE, mito-HE, HPr<sup>+</sup>, and their oxidation products**

To identify and quantify relative differences in the three fluorogenic probes and their oxidation products in cell culture systems, a targeted LC-MS/MS approach, based on multiple reaction monitoring (MRM) was developed. The mass spectrometry parameters for specific transitions of all monitored compounds were individually identified, optimized and the three best transitions per metabolite were selected for the final method. The identity of fragments was verified by high-resolution mass spectrometry (Figure 26). To increase the robustness of the LC-MS/MS method, the correct retention time of all peaks, the peak shapes, and the ion ratios were monitored. The ion ratios were calculated by dividing all transitions by the largest peak area per compound and the values must match the ratios calculated for the pure probes (Gielisch and Meierhofer 2015). All selected transitions, including internal standards, were thus combined in a single LC-MS/MS method operating in the positive ionization mode (Figure 27A, Table 9). Transitions for the three fluorogenic compounds and their O<sup>·2-</sup> specific products were additionally displayed individually (Figure 27B-G).

## Results

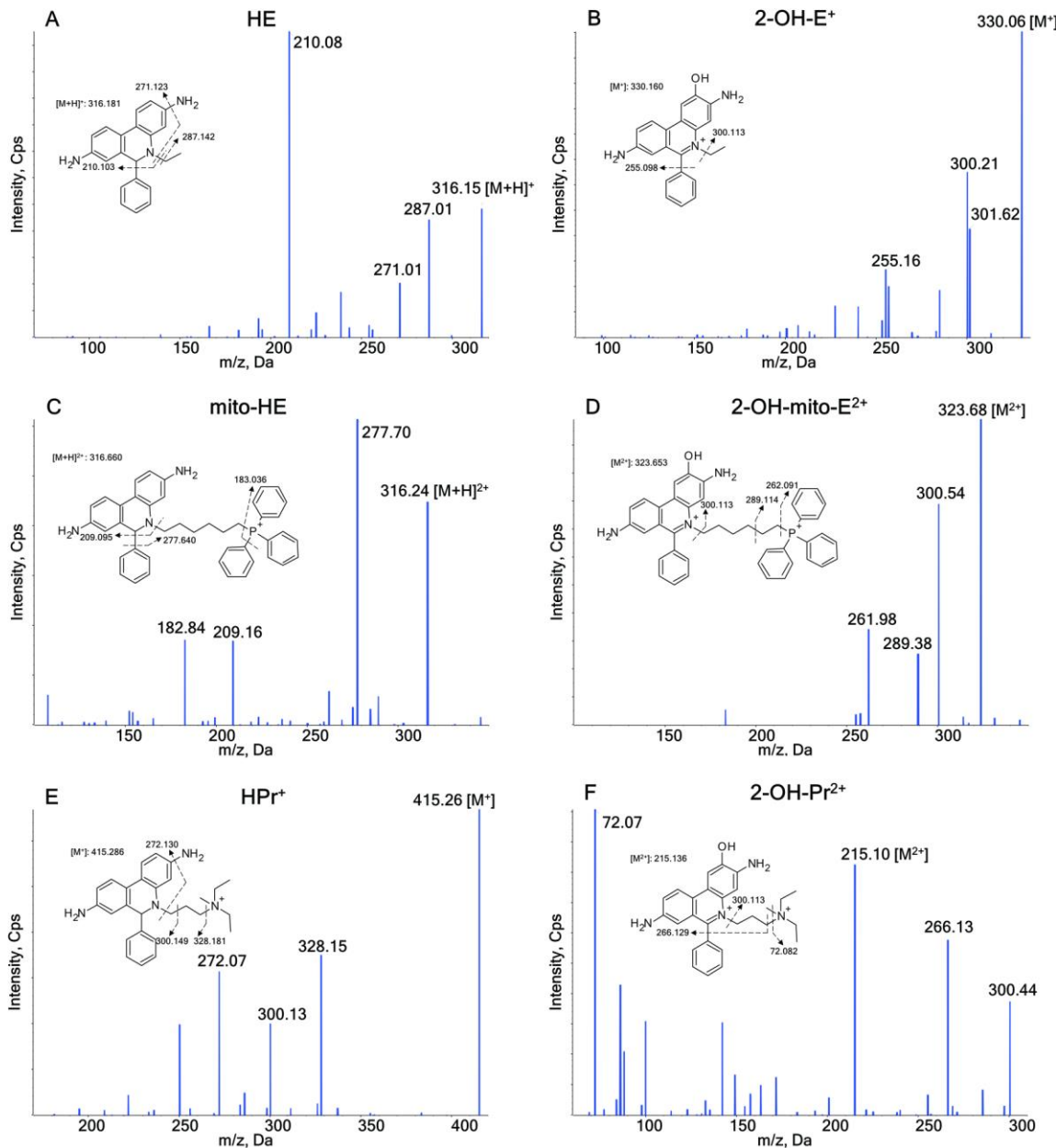


**Figure 26. Specific fragment spectra (MS<sup>2</sup>) obtained for hydroethidine probes and its O<sub>2</sub><sup>·-</sup> specific oxidized product.**

(A) HE, (B) its O<sub>2</sub><sup>·-</sup> specific oxidized product 2-OH-E<sup>+</sup>, (C) mito-HE and (D) 2-OH-mito-E<sup>2+</sup>, (E) HPr<sup>+</sup> and (F) 2-OH-Pr<sup>2+</sup>. Only the three indicated transitions per compound were included in the final MRM method that featured high intensities, unique transitions, and no matrix effects. Precursor ions are indicated by  $[M+H]$ . Structures and predicted fragments for all probes are shown. Cps, counts per second.

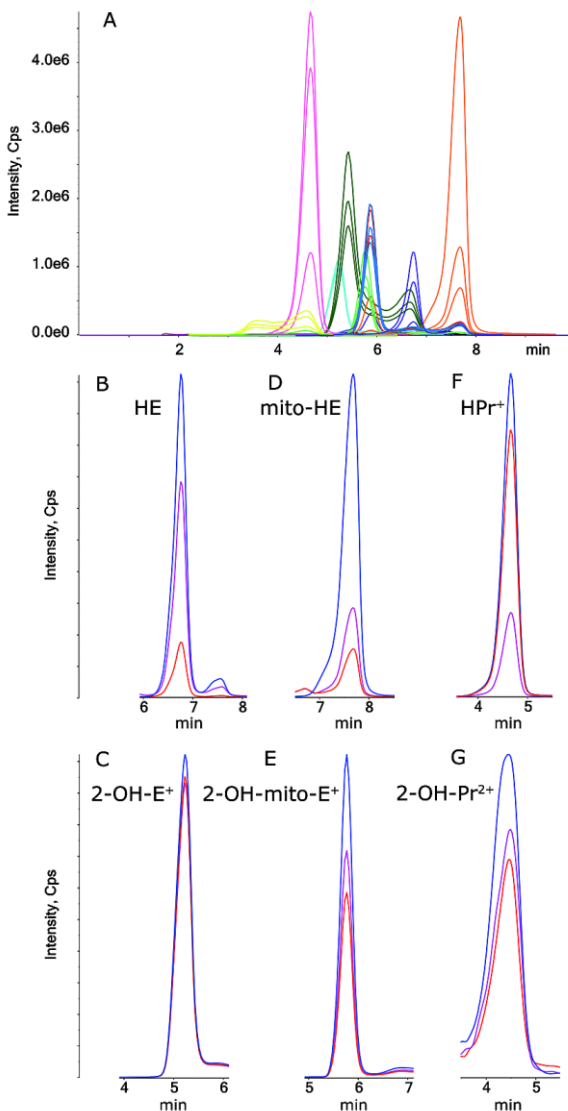


**Figure 27. MRM transitions of three fluorogenic probes and their oxidation products, separated on a reverse-phase C18 column.**

(A) All transitions were monitored in a single 10 minute LC-MS/MS run; transitions of the most important compounds are displayed individually as: (B) HE, (C) 2-OH-E<sup>+</sup>, (D) mito-HE, (E) 2-OH-mito-E<sup>2+</sup>, (F) HPr<sup>+</sup> and (G) 2-OH-HPr<sup>2+</sup>.

### 3.12.2 Fluorogenic probe stability is a significant concern

A mass spectrometry approach overcomes spectral overlap issues in fluorescence-based methods, as it relies on the exact masses of specific transitions. Given the natural tendency of the probes to undergo autoxidation, the probe stability was firstly monitored. Several time series using different light and temperature conditions were performed to monitor the stability of educts and oxidation products in a cell-free environment. Regardless of the

## Results

conditions, rapid autoxidation rates were observed in all experiments, which translated to an increase in the levels of  $\text{O}^{2-}$ -specific products (Figure 28). A 150% increase within 60 minutes was observed for the  $\text{O}^{2-}$ -specific products from all three probes under the “25 °C without light” condition at this time point (Figure 28A-C). Under standard laboratory light conditions, levels of the  $\text{O}^{2-}$ -specific products increased by over 200% and after 2 hours to more than 300% above initial values (Figure 28D-F). Light conditions had a larger impact on  $\text{O}^{2-}$ -specific products relative to that seen for temperature increases to 37 °C (Figure 28G-I). In contrast, the internal standard showed a standard deviation of 5.5 % within all experiments, indicating normal variations of the LC-MS/MS runs and in turn robust measurement conditions.

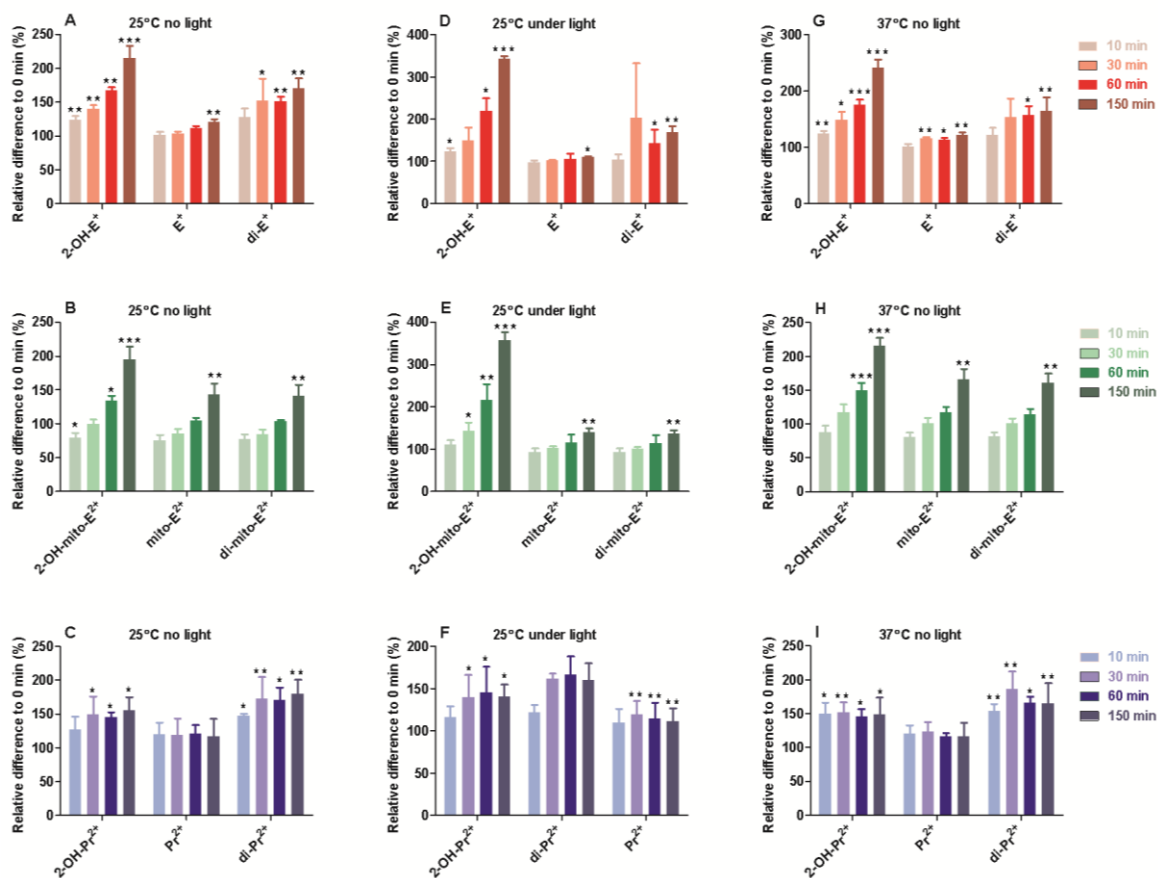


**Figure 28. Stability tests for fluorogenic probes.**

Probes were incubated in Hank's solution under (A, B, C) 25 °C without light, (D,E, F) 25 °C with light, and (G,H,I) 37 °C without light. Results are based on three biological experiments (\*p < 0.05; \*\*p < 0.01; \*\*\*p < 0.001; two tailed unpaired t-test with 0 min group). Error bars, mean ± S.D.

### 3.12.3 Effects of strong ROS stimulations in cells were smaller than those for autoxidation

HepG<sub>2</sub> cells were treated with strong ROS inducers, such as rotenone and H<sub>2</sub>O<sub>2</sub>, as well as the ROS quencher N-acetyl-cysteine (NAC) (Li, Ragheb et al. 2003, Zmijewski, Banerjee et al. 2010), to identify maximum effects in a cell system. I asked whether or not these chemical treatments show stronger ROS signals than the autoxidation rates of the probes themselves.

Upon treatment with NAC, levels of all oxidation products did not change significantly, except for Pr<sup>2+</sup>. Indeed, the fold-changes of these oxidation products were slightly reduced for HE and HPr<sup>+</sup> and unchanged for mito-HE (Figure 29A). After incubating the cells with H<sub>2</sub>O<sub>2</sub>, levels of O<sup>·2-</sup>-specific products were unchanged for mito-HE compared to controls and even reduced for HE and HPr<sup>+</sup> (Figure 29B). Rotenone treatment was associated with insignificant reductions in O<sup>·2-</sup> specific products for HE and HPr<sup>+</sup>, and only 2-OH-mito-E<sup>2+</sup> showed a significant increase of 50%. This result was perhaps predictable, given that mitochondria are sites of electron leakage (Figure 29C). All harsh treatments did not induce significant changes in the amounts of O<sup>·2-</sup> specific products, most likely because the cell culture medium already induced a high oxidation rate of the three probes, which then diminished cell-specific changes.

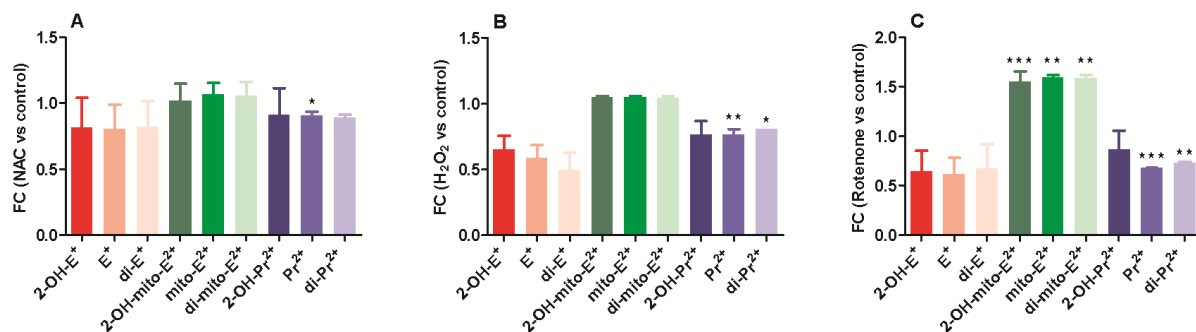


**Figure 29. ROS determination of fluorogenic probes after ROS stimulation with chemicals.**

Treatments of (A) 1 mM NAC for 20 hours, (B) 100 µM H<sub>2</sub>O<sub>2</sub> for 2 hours, and (C) 1 µM rotenone for 2 hours in HepG2 cells. NAC, N-acetyl-cysteine; FC, fold change. Results are based on three biological experiments (\*p < 0.05; \*\*p < 0.01; \*\*\*p < 0.001; two tailed unpaired t-test with control group). Error bars, mean ± S.D.

Together these results indicate that the autoxidation effects of the three probes were high upon incubation at 25 °C or 37 °C, especially under standard room light conditions. This autoxidation can compete with experimentally-induced ROS changes to diminish or perhaps

## Results

obscure the true ROS status in the presence of harsh treatments with H<sub>2</sub>O<sub>2</sub>, rotenone, or NAC.



## 4. Discussion

The first description of chRCC as a new kidney cancer entity by Thoenes et al. (Thoenes, Storkel et al. 1985) was over 30 years ago. Yet, the understanding of this rare tumor type is still limited due to its rarity. Recently, two studies, comprising roughly a hundred cases (Davis, Ricketts et al. 2014, Ricketts, De Cubas et al. 2018), were undertaken to understand the genetic cause of chRCC. In contrast, proteome and metabolome profiling data from this malign tumor are still sparse (Valera, Li-Ning et al. 2010, Schaeffeler, Buttner et al. 2018). To fill this gap, this thesis employs and integrates proteomics, transcriptomics (from TCGA), and metabolomics approaches as well as mitochondrial WES to gain insights into the mtDNA mutation landscape and to elucidate pathological alterations between chRCC and adjacent kidney tissues. In addition, these results were compared with the RO data from the previous study (Kurschner, Zhang et al. 2017) to identify molecular differences between these two highly similar tumor entities for the discovery of potential diagnostic markers.

### 4.1 The decreased mtDNA content is the main cause of dysregulation of OXPHOS in chRCC

The Warburg effect describes that cancer cells consume high amounts of glucose and have high lactate production, even under aerobic conditions (Warburg 1956). Thus, high glycolytic activity in company with reduced OXPHOS is found in many cancers. This phenomenon was also observed in this chRCC cohort, as chRCC was showed to have an enhanced glycolysis pathway, combining with the downregulated OXPHOS found in this study. Previously, a significant reduction in all mitochondrial enzyme activity as well as in the mtDNA content were found in ccRCC and pRCC (Meierhofer, Mayr et al. 2004), but at this specific point, I see a clear difference to benign RO, where only CI subunits and its enzyme activity were significantly diminished, while all other complexes and enzyme activities were significantly increased (Kurschner, Zhang et al. 2017).

The most strikingly increased set of metabolites in chRCC were those involved in GSH metabolism (GSH, GSSG, and  $\gamma$ -glutamyl-cysteine.). This finding is very similar to previous studies in chRCC (Priolo, Khabibullin et al. 2018, Xiao, Clima et al. 2019), pRCC (Al Ahmad, Paffrath et al. 2019), RO (Kurschner, Zhang et al. 2017, Gopal, Calvo et al. 2018), and in ccRCC (Wettersten, Hakimi et al. 2015, Hakimi, Reznik et al. 2016). Since GSH is an important ROS scavenger (Circu and Aw 2008), the increased GSH level and GSH/GSSG ratio in chRCC can thus be considered as the main strategy for the tumor to overcome ROS stress originating from a dysregulated OXPHOS. Similar to RO, enzymes involved in

glutathione synthesis were unchanged, but enzymes involved in glutathione degradation were significantly reduced in chRCC.

How closely protein abundance corresponds to the transcript level is a fundamental question. A discrepancy between increased transcript expression and reduced protein abundances of the OXPHOS has been observed not only in this chRCC cohort but also in RO (Kurschner, Zhang et al. 2017). This anti-correlation indicates that different levels of molecular information are necessary to evaluate and understand a pathogenic mechanism. Thus, the enzymatic activities of the OXPHOS in chRCC and RO (Mayr, Meierhofer et al. 2008) matched to protein abundances rather than to the transcript levels. A study analyzing  $\rho^0$  cells (cells without mtDNA), showed that the abundance of nuclear-encoded proteins of the respiratory chain was significantly reduced (Aretz, Hardt et al. 2016). This indicates that the observed discrepancy between proteins and transcripts of OXPHOS in chRCC is mainly caused by the reduced mtDNA content in chRCC. This has been further validated by monitoring the mtDNA depletion and the abundance of respiratory subunits in a chRCC derived cell line over time. A discrepancy between the mtDNA content and nuclear-encoded OXPHOS subunits was observed, only mtDNA-encoded transcripts almost entirely disappeared, whereas nuclear-encoded were kept stable when the cells reached the  $\rho^0$  status. In addition, the GSH level anti-correlated with the mtDNA decrease, indicating that defective respiration causes ROS stress, which is compensated by increasing the main ROS scavenger GSH.

The mitochondrial genomes in RO and thyroid cancers have been shown to have a particularly enriched mutation load (Gasparre, Hervouet et al. 2008, Mayr, Meierhofer et al. 2008, Grandhi, Bosworth et al. 2017). Although diverse potentially pathogenic mtDNA mutations with mostly low heteroplasmy loads (except case 4 mutated in *MT-ND5* gene with >60% heteroplasmy) were identified, I conclude that these low heteroplasmic mtDNA mutation most likely do not have any substantial influence to the phenotype of chRCC, as these cases did not present different regulations of the OXPHOS and showed the same overall proteome. Even though all chRCC cases had similarly increased levels of GSH and its related metabolites, case 4 did show a declined GSH/GSSG ratio in chRCC relative to the normal kidney, opposite to all the other cases. This result indicates higher oxidative stress within the *MT-ND5* mutated case. This unique phenomenon might be caused by the inclined conversion from GSH to GSSG since excessive ROS is produced when CI is deficient because of the *MT-ND5* mutations (Mayr, Meierhofer et al. 2008, Leman, Gueguen et al. 2015, Gopal, Calvo et al. 2018, Ni, Hagras et al. 2019). It seems that the CI mutation

## Discussion

in case 4 along with a decreased mtDNA content specially produced more ROS than the other cases.

A histopathological differentiation of benign RO from malignant chRCC is still difficult, even using multiple immunohistochemistry markers (Ng, Morais et al. 2016). There are also case reports on rare hybrid tumors (Noguchi, Nagashima et al. 1995), including oncocytic content (Pote, Vieillefond et al. 2013) and the rare genetic disorder Brit-Hogg-Dube (BHD) syndrome (Vera-Badillo, Conde et al. 2012), where the coexistence of RO and chRCC was shown. The accumulated microvesicles in the cytoplasm are a key histological feature in chRCC, may originate from defective mitochondriogenesis, but this feature is also not diagnostic, as they can also be found in RO and eosinophilic variants of ccRCC (Tickoo, Lee et al. 2000). Consequently, the abundance signature of OXPHOS complexes can be used to unambiguously distinguish these two tumor species.

### 4.2 ChRCC features metabolic reprogramming

The metabolic reprogramming is a very important hallmark of cancer (Hanahan and Weinberg 2011), chRCC was revealed to have substantial reprogramming of the central metabolic pathways. The energy-consuming process gluconeogenesis was entirely stalled, most likely to circumvent limited nutritional supplies. This seems to be a general mechanism in kidney cancer since similar observations were also reported in RO (Kurschner, Zhang et al. 2017) and at the transcript level for pRCC (Cancer Genome Atlas Research, Linehan et al. 2016) and ccRCC (Li, Qiu et al. 2014). The down-regulation of FBP1, a key player in gluconeogenesis, was further linked to ccRCC progression and was shown to inhibit nuclear hypoxia inducible factor function (Li, Qiu et al. 2014). This further stimulates the metabolic switch by up-regulating the glycolytic target genes upon its loss in the tumor. The effect of increasing glycolytic enzymes was also seen in the chRCC proteome data. Of equal importance is the uptake of glutamine and glucose to sustain tumor growth, which was shown to be significantly lower in chRCC compared with ccRCC and pRCC (Nakajima, Nozaki et al. 2017). This could be the consequence of a low microvessel density observed in chRCC compared with ccRCC tumors (Jinzaki, Tanimoto et al. 2000). Hence, chRCC seems to be poorly supported by classical nutrition supply chains.

Contrary to the observed abundance decrease of gluconeogenic proteins in chRCC, the over-expression of gluconeogenic genes and proteins are frequently found in other tumor species. Specifically, increased ALDOB expression was found to favor cancer cell proliferation and metastasis in multiple cancers, such as colon cancer (Bu, Chen et al.

2018), rectal cancer (Tian, Hsieh et al. 2017), and colorectal adenocarcinoma (Li, Li et al. 2017). This might be one reason for the low metastatic potential (Volpe, Novara et al. 2012) and the high survival rate observed in the chRCC patients (Amin, Amin et al. 2002, Przybycin, Cronin et al. 2011).

Besides the dramatic reduction in enzymes involved in gluconeogenesis and the OXPHOS, a decrease in the proteins of the fatty acid and amino acid synthesis pathways was identified in chRCC. One might wonder how this tumor could sustain viability and growth with the downregulation of so many key metabolic pathways. However, the actual level of amino acids and metabolites, which can be regarded as essential “energy carriers”, such as FAD, NADPH, ADP, cyclic AMP, and NAD<sup>+</sup> were indeed unchanged, indicating a sufficient amount of building blocks and nutrients in chRCC. Only amino acid intermediates were decreased in chRCC, reflecting a lower activity of pathways involved in amino acid metabolism. In contrast, increased amino acid metabolism was frequently found in other cancer types to promote proliferation and metastasis, such as glycine and serine metabolism in breast cancer (Jain, Nilsson et al. 2012) and serine biosynthesis in multiple cancers (Gromova, Gromov et al. 2015, Jia, Zhang et al. 2016).

I thus hypothesize that chRCC use other ways than those discussed to acquire nutrition. In addition to all of the decreased pathways involved in energy metabolism, the vascular ATPases were showed to be increased in chRCC, the lysosome and the proteasome were found to be significantly enriched. These results are clues for an alternative nutritional supply in chRCC. The modulation of the microenvironment by the acidity of vascular ATPases, to acidify and hydrolyze macromolecules to fuel biomass production (Dettmer, Hong-Hermesdorf et al. 2006, Repnik, Cesen et al. 2013, Davidson and Vander Heiden 2017), might be one advantage for chRCC survival and viability. The lysosomes and proteasomes are involved in the cell recycling machinery by contributing and delivering new biomass via endocytosis, phagocytosis, and autophagy. The downregulations of pathways involved in amino acid metabolism paralleled with an increased abundance of the vascular ATPases, lysosome, proteasome, ubiquitin-mediated proteolysis, and endocytosis suggest a main adaptive mechanism to gain nutrition in chRCC, as a response to poor classical nutrition supply chains.

PLCG2 was one of the highest increased significant proteins identified by proteome profiling and its corresponding transcript was also found to be highly upregulated in chRCC relative to the healthy kidney tissues (Davis, Ricketts et al. 2014). PLCG2 functions as a membrane enzyme catalyzing the conversion of PIP2 to IP3 and DAG, which further activates PKC

## Discussion

directly or through stimulating the  $\text{Ca}^{2+}$  release from the endoplasmic reticulum. During pharmaceutical inhibition of the PLCG2/IP3/ $\text{Ca}^{2+}$ /PKC pathway, a significant decrease of the endocytosis of macromolecules was found in the chRCC cell line. Furthermore, endocytosis was reported to suppress cancer cell blebbing and invasion by increasing the cell membrane tension and thus reduced the likelihood of mechanical invasion to the surrounding tissue (Holst, Vidal-Quadras et al. 2017). This finding further matches the low rate (1.3%) of metastatic chRCC cases (Volpe, Novara et al. 2012).

### **4.3 ROS measurement with the hydroethidine-based probes should be interpreted with caution**

At present, fluorescence- and HPLC-based approaches are frequently used with hydroethidine-based probes such as HE, mito-HE or  $\text{HPr}^+$  to assess the ROS status in cells (Robinson, Janes et al. 2006, Zielonka, Hardy et al. 2009, Kalyanaraman, Dranka et al. 2014). However, such probes have several drawbacks in fluorescence or HPLC applications, particularly because of spectral overlap in fluorescence assays and low specificity in HPLC methods. In this project, a new LC-MS/MS method was developed that can simultaneously detect and quantify these three fluorogenic probes and their corresponding oxidation products. This method resulted in a rapid, sensitive and specific LC-MS/MS method to elucidate the ROS status in a cell system with spatial resolution. Three specific transitions for each of the educts and oxidized products as well as the ion ratios between the transitions and the correct retention time were monitored to ensure high selectivity. This method eliminates problematic fluorescence spectral overlap that is typical of fluorescence-based techniques and the low specificity associated with the use of only HPLC-based methods. However, the results indicated that these hydroethidine-based probes were intrinsically prone to oxidation. Incubation at 25 °C or 37 °C in the stability test led to rapid probe autoxidation, which could complicate the results obtained when these probes are used for ROS detection. Accordingly, the harsh conditions used for ROS induction and inhibition treatments generated results for the oxidized fluorophores that lacked significance and reproducibility. Hence, subtle changes in ROS levels that can occur in biological systems and that can be used to achieve new insights into redox homeostasis may not be detectable.

In addition to the instability of hydroethidine-based probes, other inherent characteristics can impede ROS detection, including complex chemical reactions, intercalation with DNA, and interference with heme-containing enzymes (Dikalov and Harrison 2014). Heme proteins,

such as hemoglobin and myoglobin, can react with HE and form fluorescent products. These chemical reactions can produce many other oxidation products that can compete with radical specific products and may influence the amount of detectable  $\text{O}^{\cdot 2-}$ -specific products. In addition, the formation of  $\text{O}^{\cdot 2-}$ -specific products could be influenced by peroxidase reactions that can interfere with  $\text{O}^{\cdot 2-}$  quantification (Dikalov and Harrison 2014). Meanwhile, mito-HE can be translocated to other intracellular organelles that have a higher negative membrane potential (Kalyanaraman, Dranka et al. 2014).

This targeted LC-MS/MS method allows the selective identification and quantification of the fluorogenic compounds HE, mito-HE, and HPr and their respective  $\text{O}^{\cdot 2-}$ -specific products. However, a high autoxidation rate was also detected for the probes alone in Hank's solution. These findings suggest that, despite the many recent methodological improvements in ROS quantification, direct measurements of ROS levels based on hydroethidine probes may be inaccurate due to artifactual effects of autoxidation. Experiments performed using these probes should thus be interpreted with caution, and autoxidation rates should be monitored.

## 5. Conclusion

In this thesis, three omics approaches, including proteomics, metabolomics, and mitochondrial whole-exome sequencing, were employed to characterize chRCC. Based on the integrative analyses of these omics data, I conclude that chRCC is a tumor type with a rewired metabolism, indicated by the down-regulation of key metabolic pathways, including OXPHOS, gluconeogenesis, glutathione metabolism, and all pathways associated with amino acid metabolism. Unlike RO, the decrease of mtDNA content rather than CI mutations is the main cause of dysfunctional OXPHOS in chRCC. In addition, chRCC depends on extracellular macromolecules as an amino acid source by activating endocytosis, which is mediated by PLCG2/IP3/Ca<sup>2+</sup>/PKC pathway. What's more, I find that using hydroethidine probes to measure ROS level is inaccurate due to artifacts caused by autoxidation.

This work provides novel insights into the rewiring of metabolic pathways in chRCC, discovers the distinct regulation of the OXPHOS as a potential diagnostic marker to distinguish chRCC from RO, and identifies PLCG2 as a potential therapeutic target to treat chRCC. In addition, the ROS measurements based on hydroethidine probes should be interpreted with caution.



## References

Aebersold, R. and M. Mann (2003). "Mass spectrometry-based proteomics." Nature **422**(6928): 198-207. <http://doi.org/10.1038/nature01511>

Aebersold, R. and M. Mann (2016). "Mass-spectrometric exploration of proteome structure and function." Nature **537**(7620): 347-355. <http://doi.org/10.1038/nature19949>

Ahmad, A. A., V. Paffrath, R. Clima, J. F. Busch, A. Rabien, E. Kilic, S. Villegas, B. Timmermann, M. Attimonelli, K. Jung and D. Meierhofer (2019). "Papillary Renal Cell Carcinomas Rewire Glutathione Metabolism and Are Deficient in Both Anabolic Glucose Synthesis and Oxidative Phosphorylation." Cancers **11**(9): 1298. <http://doi.org/10.3390/cancers11091298>

Al Ahmad, A., V. Paffrath, R. Clima, J. F. Busch, A. Rabien, E. Kilic, S. Villegas, B. Timmermann, M. Attimonelli, K. Jung and D. Meierhofer (2019). "Papillary Renal Cell Carcinomas Rewire Glutathione Metabolism and Are Deficient in Both Anabolic Glucose Synthesis and Oxidative Phosphorylation." Cancers (Basel) **11**(9): <http://doi.org/10.3390/cancers11091298>

Amin, M. B., M. B. Amin, P. Tamboli, J. Javidan, H. Stricker, M. de-Peralta Venturina, A. Deshpande and M. Menon (2002). "Prognostic impact of histologic subtyping of adult renal epithelial neoplasms: an experience of 405 cases." Am J Surg Pathol **26**(3): 281-291. <http://doi.org/10.1097/00000478-200203000-00001>

Anderson, N. L. and N. G. Anderson (1998). "Proteome and proteomics: new technologies, new concepts, and new words." ELECTROPHORESIS **19**(11): 1853-1861. <http://doi.org/10.1002/elps.1150191103>

Aretz, I., C. Hardt, I. Wittig and D. Meierhofer (2016). "An Impaired Respiratory Electron Chain Triggers Down-regulation of the Energy Metabolism and De-ubiquitination of Solute Carrier Amino Acid Transporters." Mol Cell Proteomics **15**(5): 1526-1538. <http://doi.org/10.1074/mcp.M115.053181>

Awasthi, Y. C., G. Misra, D. K. Rassin and S. K. Srivastava (1983). "Detoxification of xenobiotics by glutathione S-transferases in erythrocytes: the transport of the conjugate of

glutathione and 1-chloro-2,4-dinitrobenzene." Br J Haematol **55**(3): 419-425.  
<http://doi.org/10.1111/j.1365-2141.1983.tb02156.x>

Baba, M., L. S. Schmidt and W. M. Linehan (2017). Hereditary Renal Cell Carcinoma. Renal Cell Carcinoma: Molecular Features and Treatment Updates. M. Oya. Tokyo, Springer Japan: 19-82. [http://doi.org/10.1007/978-4-431-55531-5\\_2](http://doi.org/10.1007/978-4-431-55531-5_2)

Bateman, N. W., S. P. Goulding, N. J. Shulman, A. K. Gadok, K. K. Szumlinski, M. J. MacCoss and C. C. Wu (2014). "Maximizing peptide identification events in proteomic workflows using data-dependent acquisition (DDA)." Mol Cell Proteomics **13**(1): 329-338.  
<http://doi.org/10.1074/mcp.M112.026500>

Benusiglio, P. R., S. Giraud, S. Deveaux, A. Mejean, J. M. Correas, D. Joly, M. O. Timsit, S. Ferlicot, V. Verkarre, C. Abadie, D. Chauveau, D. Leroux, M. F. Avril, J. F. Cordier, S. Richard and N. French National Cancer Institute Inherited Predisposition to Kidney Cancer (2014). "Renal cell tumour characteristics in patients with the Birt-Hogg-Dube cancer susceptibility syndrome: a retrospective, multicentre study." Orphanet J Rare Dis **9**(1): 163.  
<http://doi.org/10.1186/s13023-014-0163-z>

Bray, F., J. Ferlay, I. Soerjomataram, R. L. Siegel, L. A. Torre and A. Jemal (2018). "Global cancer statistics 2018: GLOBOCAN estimates of incidence and mortality worldwide for 36 cancers in 185 countries." CA Cancer J Clin **68**(6): 394-424.  
<http://doi.org/10.3322/caac.21492>

Brunelli, M., J. N. Eble, S. Zhang, G. Martignoni, B. Delahunt and L. Cheng (2005). "Eosinophilic and classic chromophobe renal cell carcinomas have similar frequent losses of multiple chromosomes from among chromosomes 1, 2, 6, 10, and 17, and this pattern of genetic abnormality is not present in renal oncocytoma." Mod Pathol **18**(2): 161-169.  
<http://doi.org/10.1038/modpathol.3800286>

Bu, P., K. Y. Chen, K. Xiang, C. Johnson, S. B. Crown, N. Rakhilin, Y. Ai, L. Wang, R. Xi, I. Astapova, Y. Han, J. Li, B. B. Barth, M. Lu, Z. Gao, R. Mines, L. Zhang, M. Herman, D. Hsu, G. F. Zhang and X. Shen (2018). "Aldolase B-Mediated Fructose Metabolism Drives Metabolic Reprogramming of Colon Cancer Liver Metastasis." Cell Metab **27**(6): 1249-1262 e1244. <http://doi.org/10.1016/j.cmet.2018.04.003>

## References

Calabrese, C., D. Simone, M. A. Diroma, M. Santorsola, C. Gutta, G. Gasparre, E. Picardi, G. Pesole and M. Attimonelli (2014). "MToolBox: a highly automated pipeline for heteroplasmy annotation and prioritization analysis of human mitochondrial variants in high-throughput sequencing." *Bioinformatics* **30**(21): 3115-3117.

<http://doi.org/10.1093/bioinformatics/btu483>

Calvo, S. E., K. R. Clauser and V. K. Mootha (2016). "MitoCarta2.0: an updated inventory of mammalian mitochondrial proteins." *Nucleic Acids Res* **44**(D1): D1251-1257.

<http://doi.org/10.1093/nar/gkv1003>

Cancer Genome Atlas Research, N. (2013). "Comprehensive molecular characterization of clear cell renal cell carcinoma." *Nature* **499**(7456): 43-49. <http://doi.org/10.1038/nature12222>

Cancer Genome Atlas Research, N., W. M. Linehan, P. T. Spellman, C. J. Ricketts, C. J. Creighton, S. S. Fei, C. Davis, D. A. Wheeler, B. A. Murray, L. Schmidt, C. D. Vocke, M. Peto, A. A. Al Mamun, E. Shinbrot, A. Sethi, S. Brooks, W. K. Rathmell, A. N. Brooks, K. A. Hoadley, A. G. Robertson, D. Brooks, R. Bowlby, S. Sadeghi, H. Shen, D. J. Weisenberger, M. Bootwalla, S. B. Baylin, P. W. Laird, A. D. Cherniack, G. Saksena, S. Haake, J. Li, H. Liang, Y. Lu, G. B. Mills, R. Akbani, M. D. Leiserson, B. J. Raphael, P. Anur, D. Bottaro, L. Albiges, N. Barnabas, T. K. Choueiri, B. Czerniak, A. K. Godwin, A. A. Hakimi, T. H. Ho, J. Hsieh, M. Ittmann, W. Y. Kim, B. Krishnan, M. J. Merino, K. R. Mills Shaw, V. E. Reuter, E. Reznik, C. S. Shelley, B. Shuch, S. Signoretti, R. Srinivasan, P. Tamboli, G. Thomas, S. Tickoo, K. Burnett, D. Crain, J. Gardner, K. Lau, D. Mallory, S. Morris, J. D. Paulauskis, R. J. Penny, C. Shelton, W. T. Shelton, M. Sherman, E. Thompson, P. Yena, M. T. Avedon, J. Bowen, J. M. Gastier-Foster, M. Gerken, K. M. Leraas, T. M. Lichtenberg, N. C. Ramirez, T. Santos, L. Wise, E. Zmuda, J. A. Demchok, I. Felau, C. M. Hutter, M. Sheth, H. J. Sofia, R. Tarnuzzer, Z. Wang, L. Yang, J. C. Zenklusen, J. Zhang, B. Ayala, J. Baboud, S. Chudamani, J. Liu, L. Lolla, R. Naresh, T. Pihl, Q. Sun, Y. Wan, Y. Wu, A. Ally, M. Balasundaram, S. Balu, R. Beroukhim, T. Bodenheimer, C. Buhay, Y. S. Butterfield, R. Carlsen, S. L. Carter, H. Chao, E. Chuah, A. Clarke, K. R. Covington, M. Dahdouli, N. Dewal, N. Dhalla, H. V. Doddapaneni, J. A. Drummond, S. B. Gabriel, R. A. Gibbs, R. Guin, W. Hale, A. Hawes, D. N. Hayes, R. A. Holt, A. P. Hoyle, S. R. Jefferys, S. J. Jones, C. D. Jones, D. Kalra, C. Kovar, L. Lewis, J. Li, Y. Ma, M. A. Marra, M. Mayo, S. Meng, M. Meyerson, P. A. Mieczkowski, R. A. Moore, D. Morton, L. E. Mose, A. J. Mungall, D. Muzny, J. S. Parker, C. M. Perou, J. Roach, J. E. Schein, S. E. Schumacher, Y. Shi, J. V. Simons,

P. Sipahimalani, T. Skelly, M. G. Soloway, C. Sougnez, A. Tam, D. Tan, N. Thiessen, U. Veluvolu, M. Wang, M. D. Wilkerson, T. Wong, J. Wu, L. Xi, J. Zhou, J. Bedford, F. Chen, Y. Fu, M. Gerstein, D. Haussler, K. Kasaian, P. Lai, S. Ling, A. Radenbaugh, D. Van Den Berg, J. N. Weinstein, J. Zhu, M. Albert, I. Alexopoulou, J. J. Andersen, J. T. Auman, J. Bartlett, S. Bastacky, J. Bergsten, M. L. Blute, L. Boice, R. J. Bollag, J. Boyd, E. Castle, Y. B. Chen, J. C. Cheville, E. Curley, B. Davies, A. DeVolk, R. Dhir, L. Dike, J. Eckman, J. Engel, J. Harr, R. Hrebinko, M. Huang, L. Huelsenbeck-Dill, M. Iacocca, B. Jacobs, M. Lobis, J. K. Maranchie, S. McMeekin, J. Myers, J. Nelson, J. Parfitt, A. Parwani, N. Petrelli, B. Rabeno, S. Roy, A. L. Salner, J. Slaton, M. Stanton, R. H. Thompson, L. Thorne, K. Tucker, P. M. Weinberger, C. Winemiller, L. A. Zach and R. Zuna (2016). "Comprehensive Molecular Characterization of Papillary Renal-Cell Carcinoma." *N Engl J Med* **374**(2): 135-145. <http://doi.org/10.1056/NEJMoa1505917>

Casuscelli, J., N. Weinhold, G. Gundem, L. Wang, E. C. Zabor, E. Drill, P. I. Wang, G. J. Nanjangud, A. Redzematovic, A. M. Nargund, B. J. Manley, M. E. Arcila, N. M. Donin, J. C. Cheville, R. H. Thompson, A. J. Pantuck, P. Russo, E. H. Cheng, W. Lee, S. K. Tickoo, I. Ostrovnaya, C. J. Creighton, E. Papaemmanuil, V. E. Seshan, A. A. Hakimi and J. J. Hsieh (2017). "Genomic landscape and evolution of metastatic chromophobe renal cell carcinoma." *JCI Insight* **2**(12): <http://doi.org/10.1172/jci.insight.92688>

Chen, Q., E. J. Vazquez, S. Moghaddas, C. L. Hoppel and E. J. Lesnefsky (2003). "Production of reactive oxygen species by mitochondria: central role of complex III." *J Biol Chem* **278**(38): 36027-36031. <http://doi.org/10.1074/jbc.M304854200>

Chin, A. I., J. S. Lam, R. A. Figlin and A. S. Belldegrun (2006). "Surveillance strategies for renal cell carcinoma patients following nephrectomy." *Rev Urol* **8**(1): 1-7.

Cho, E. S., N. Johnson and B. C. Snider (1984). "Tissue glutathione as a cyst(e)ine reservoir during cystine depletion in growing rats." *J Nutr* **114**(10): 1853-1862. <http://doi.org/10.1093/jn/114.10.1853>

Circu, M. L. and T. Y. Aw (2008). "Glutathione and apoptosis." *Free Radic Res* **42**(8): 689-706. <http://doi.org/10.1080/10715760802317663>

Collins, B. C., C. L. Hunter, Y. Liu, B. Schilling, G. Rosenberger, S. L. Bader, D. W. Chan, B. W. Gibson, A. C. Gingras, J. M. Held, M. Hirayama-Kurogi, G. Hou, C. Krisp, B. Larsen, L.

## References

- Lin, S. Liu, M. P. Molloy, R. L. Moritz, S. Ohtsuki, R. Schlapbach, N. Selevsek, S. N. Thomas, S. C. Tzeng, H. Zhang and R. Aebersold (2017). "Multi-laboratory assessment of reproducibility, qualitative and quantitative performance of SWATH-mass spectrometry." Nat Commun **8**(1): 291. <http://doi.org/10.1038/s41467-017-00249-5>
- Cox, J. and M. Mann (2008). "MaxQuant enables high peptide identification rates, individualized p.p.b.-range mass accuracies and proteome-wide protein quantification." Nat Biotechnol **26**(12): 1367-1372. <http://doi.org/10.1038/nbt.1511>
- Dass, C. (2006). Tandem Mass Spectrometry. Fundamentals of Contemporary Mass Spectrometry: 119-150. <http://doi.org/10.1002/9780470118498.ch4>
- Davidson, S. M. and M. G. Vander Heiden (2017). "Critical Functions of the Lysosome in Cancer Biology." Annu Rev Pharmacol Toxicol **57**: 481-507. <http://doi.org/10.1146/annurev-pharmtox-010715-103101>
- Davis, C. F., C. J. Ricketts, M. Wang, L. Yang, A. D. Cherniack, H. Shen, C. Buhay, H. Kang, S. C. Kim, C. C. Fahey, K. E. Hacker, G. Bhanot, D. A. Gordenin, A. Chu, P. H. Gunaratne, M. Biehl, S. Seth, B. A. Kaipparettu, C. A. Bristow, L. A. Donehower, E. M. Wallen, A. B. Smith, S. K. Tickoo, P. Tamboli, V. Reuter, L. S. Schmidt, J. J. Hsieh, T. K. Choueiri, A. A. Hakimi, N. The Cancer Genome Atlas Research, L. Chin, M. Meyerson, R. Kucherlapati, W. Y. Park, A. G. Robertson, P. W. Laird, E. P. Henske, D. J. Kwiatkowski, P. J. Park, M. Morgan, B. Shuch, D. Muzny, D. A. Wheeler, W. M. Linehan, R. A. Gibbs, W. K. Rathmell and C. J. Creighton (2014). "The somatic genomic landscape of chromophobe renal cell carcinoma." Cancer Cell **26**(3): 319-330. <http://doi.org/10.1016/j.ccr.2014.07.014>
- de Hoffmann, E. (1996). "Tandem mass spectrometry: A primer." Journal of Mass Spectrometry **31**(2): 129-137. [http://doi.org/10.1002/\(sici\)1096-9888\(199602\)31:2<129::aid-jms305>3.0.co;2-t](http://doi.org/10.1002/(sici)1096-9888(199602)31:2<129::aid-jms305>3.0.co;2-t)
- Delahunt, B. and J. N. Eble (1997). "Papillary renal cell carcinoma: a clinicopathologic and immunohistochemical study of 105 tumors." Mod Pathol **10**(6): 537-544.
- Delahunt, B., J. R. Srigley, R. Montironi and L. Egevad (2014). "Advances in renal neoplasia: recommendations from the 2012 International Society of Urological Pathology

Consensus Conference." *Urology* **83**(5): 969-974.  
<http://doi.org/10.1016/j.urology.2014.02.004>

Dettmer, J., A. Hong-Hermesdorf, Y. D. Stierhof and K. Schumacher (2006). "Vacuolar H+-ATPase activity is required for endocytic and secretory trafficking in Arabidopsis." *Plant Cell* **18**(3): 715-730. <http://doi.org/10.1105/tpc.105.037978>

Dikalov, S. I. and D. G. Harrison (2014). "Methods for detection of mitochondrial and cellular reactive oxygen species." *Antioxid Redox Signal* **20**(2): 372-382.  
<http://doi.org/10.1089/ars.2012.4886>

Domon, B. and R. Aebersold (2006). "Mass spectrometry and protein analysis." *Science* **312**(5771): 212-217. <http://doi.org/10.1126/science.1124619>

Duan, J., V. K. Kodali, M. J. Gaffrey, J. Guo, R. K. Chu, D. G. Camp, R. D. Smith, B. D. Thrall and W. J. Qian (2016). "Quantitative Profiling of Protein S-Glutathionylation Reveals Redox-Dependent Regulation of Macrophage Function during Nanoparticle-Induced Oxidative Stress." *ACS Nano* **10**(1): 524-538. <http://doi.org/10.1021/acsnano.5b05524>

Durinck, S., E. W. Stawiski, A. Pavia-Jimenez, Z. Modrusan, P. Kapur, B. S. Jaiswal, N. Zhang, V. Toffessi-Tcheuyap, T. T. Nguyen, K. B. Pahuja, Y. J. Chen, S. Saleem, S. Chaudhuri, S. Heldens, M. Jackson, S. Pena-Llopis, J. Guillory, K. Toy, C. Ha, C. J. Harris, E. Holloman, H. M. Hill, J. Stinson, C. S. Rivers, V. Janakiraman, W. Wang, L. N. Kinch, N. V. Grishin, P. M. Haverty, B. Chow, J. S. Gehring, J. Reeder, G. Pau, T. D. Wu, V. Margulis, Y. Lotan, A. Sagalowsky, I. Pedrosa, F. J. de Sauvage, J. Brugarolas and S. Seshagiri (2015). "Spectrum of diverse genomic alterations define non-clear cell renal carcinoma subtypes." *Nat Genet* **47**(1): 13-21. <http://doi.org/10.1038/ng.3146>

Ellman, G. L. (1958). "A colorimetric method for determining low concentrations of mercaptans." *Arch Biochem Biophys* **74**(2): 443-450. [http://doi.org/10.1016/0003-9861\(58\)90014-6](http://doi.org/10.1016/0003-9861(58)90014-6)

Fay, A. P., S. Signoretti and T. K. Choueiri (2014). "MET as a target in papillary renal cell carcinoma." *Clin Cancer Res* **20**(13): 3361-3363. <http://doi.org/10.1158/1078-0432.CCR-14-0690>

## References

- Gasparre, G., E. Hervouet, E. de Laplanche, J. Demont, L. F. Pennisi, M. Colombel, F. Mege-Lechevallier, J. Y. Scoazec, E. Bonora, R. Smeets, J. Smeitink, V. Lazar, J. Lespinasse, S. Giraud, C. Godinot, G. Romeo and H. Simonnet (2008). "Clonal expansion of mutated mitochondrial DNA is associated with tumor formation and complex I deficiency in the benign renal oncocytoma." *Hum Mol Genet* **17**(7): 986-995. <http://doi.org/10.1093/hmg/ddm371>
- Gasparre, G., G. Romeo, M. Rugolo and A. M. Porcelli (2011). "Learning from oncocytic tumors: Why choose inefficient mitochondria?" *Biochim Biophys Acta* **1807**(6): 633-642. <http://doi.org/10.1016/j.bbabi.2010.08.006>
- Gielisch, I. and D. Meierhofer (2015). "Metabolome and proteome profiling of complex I deficiency induced by rotenone." *J Proteome Res* **14**(1): 224-235. <http://doi.org/10.1021/pr500894v>
- Gillet, L. C., P. Navarro, S. Tate, H. Rost, N. Selevsek, L. Reiter, R. Bonner and R. Aebersold (2012). "Targeted data extraction of the MS/MS spectra generated by data-independent acquisition: a new concept for consistent and accurate proteome analysis." *Mol Cell Proteomics* **11**(6): O111 016717. <http://doi.org/10.1074/mcp.O111.016717>
- Goldman, M., B. Craft, M. Hastie, K. Repečka, A. Kamath, F. McDade, D. Rogers, A. N. Brooks, J. Zhu and D. Haussler (2019). "The UCSC Xena Platform for cancer genomics data visualization and interpretation." *bioRxiv*: 326470. <http://doi.org/10.1101/326470>
- Gopal, R. K., S. E. Calvo, A. R. Shih, F. L. Chaves, D. McGuone, E. Mick, K. A. Pierce, Y. Li, A. Garofalo, E. M. Van Allen, C. B. Clish, E. Oliva and V. K. Mootha (2018). "Early loss of mitochondrial complex I and rewiring of glutathione metabolism in renal oncocytoma." *Proc Natl Acad Sci U S A* **115**(27): E6283-E6290. <http://doi.org/10.1073/pnas.1711888115>
- Gossage, L., T. Eisen and E. R. Maher (2015). "VHL, the story of a tumour suppressor gene." *Nat Rev Cancer* **15**(1): 55-64. <http://doi.org/10.1038/nrc3844>
- Grabowski, G. A., J. R. Kruse, J. D. Goldberg, K. Chockkalingam, R. E. Gordon, K. J. Blakemore, M. J. Mahoney and R. J. Desnick (1984). "First-trimester prenatal diagnosis of Tay-Sachs disease." *Am J Hum Genet* **36**(6): 1369-1378.

Grandhi, S., C. Bosworth, W. Maddox, C. Sensiba, S. Akhavanfard, Y. Ni and T. LaFramboise (2017). "Heteroplasmic shifts in tumor mitochondrial genomes reveal tissue-specific signals of relaxed and positive selection." *Hum Mol Genet* **26**(15): 2912-2922. <http://doi.org/10.1093/hmg/ddx172>

Gromova, I., P. Gromov, N. Honma, S. Kumar, D. Rimm, M. L. Talman, V. T. Wielenga and J. M. Moreira (2015). "High level PHGDH expression in breast is predominantly associated with keratin 5-positive cell lineage independently of malignancy." *Mol Oncol* **9**(8): 1636-1654. <http://doi.org/10.1016/j.molonc.2015.05.003>

Guo, T., P. Kouvonnen, C. C. Koh, L. C. Gillet, W. E. Wolski, H. L. Rost, G. Rosenberger, B. C. Collins, L. C. Blum, S. Gillessen, M. Joerger, W. Jochum and R. Aebersold (2015). "Rapid mass spectrometric conversion of tissue biopsy samples into permanent quantitative digital proteome maps." *Nat Med* **21**(4): 407-413. <http://doi.org/10.1038/nm.3807>

Haake, S. M., J. D. Weyandt and W. K. Rathmell (2016). "Insights into the Genetic Basis of the Renal Cell Carcinomas from The Cancer Genome Atlas." *Mol Cancer Res* **14**(7): 589-598. <http://doi.org/10.1158/1541-7786.MCR-16-0115>

Hakimi, A. A., E. Reznik, C. H. Lee, C. J. Creighton, A. R. Brannon, A. Luna, B. A. Aksoy, E. M. Liu, R. Shen, W. Lee, Y. Chen, S. M. Stirdvant, P. Russo, Y. B. Chen, S. K. Tickoo, V. E. Reuter, E. H. Cheng, C. Sander and J. J. Hsieh (2016). "An Integrated Metabolic Atlas of Clear Cell Renal Cell Carcinoma." *Cancer Cell* **29**(1): 104-116. <http://doi.org/10.1016/j.ccr.2015.12.004>

Hanahan, D. and R. A. Weinberg (2011). "Hallmarks of cancer: the next generation." *Cell* **144**(5): 646-674. <http://doi.org/10.1016/j.cell.2011.02.013>

Hatem, E., N. El Banna and M. E. Huang (2017). "Multifaceted Roles of Glutathione and Glutathione-Based Systems in Carcinogenesis and Anticancer Drug Resistance." *Antioxid Redox Signal* **27**(15): 1217-1234. <http://doi.org/10.1089/ars.2017.7134>

Hes, O., F. Petersson, N. Kuroda, M. Hora and M. Michal (2013). "Renal hybrid oncocytic/chromophobe tumors - a review." *Histol Histopathol* **28**(10): 1257-1264. <http://doi.org/10.14670/HH-28.1257>

## References

Hoadley, K. A., C. Yau, T. Hinoue, D. M. Wolf, A. J. Lazar, E. Drill, R. Shen, A. M. Taylor, A. D. Cherniack, V. Thorsson, R. Akbani, R. Bowlby, C. K. Wong, M. Wiznerowicz, F. Sanchez-Vega, A. G. Robertson, B. G. Schneider, M. S. Lawrence, H. Noushmehr, T. M. Malta, N. Cancer Genome Atlas, J. M. Stuart, C. C. Benz and P. W. Laird (2018). "Cell-of-Origin Patterns Dominate the Molecular Classification of 10,000 Tumors from 33 Types of Cancer." *Cell* **173**(2): 291-304 e296. <http://doi.org/10.1016/j.cell.2018.03.022>

Hofbauer, S. L., K. I. Stangl, M. de Martino, I. Lucca, A. Haitel, S. F. Shariat and T. Klatte (2014). "Pretherapeutic gamma-glutamyltransferase is an independent prognostic factor for patients with renal cell carcinoma." *Br J Cancer* **111**(8): 1526-1531. <http://doi.org/10.1038/bjc.2014.450>

Holst, M. R., M. Vidal-Quadras, E. Larsson, J. Song, M. Hubert, J. Blomberg, M. Lundborg, M. Landstrom and R. Lundmark (2017). "Clathrin-Independent Endocytosis Suppresses Cancer Cell Blebbing and Invasion." *Cell Rep* **20**(8): 1893-1905. <http://doi.org/10.1016/j.celrep.2017.08.006>

Hussain, S. P., L. J. Hofseth and C. C. Harris (2003). "Radical causes of cancer." *Nat Rev Cancer* **3**(4): 276-285. <http://doi.org/10.1038/nrc1046>

Ivan, M., K. Kondo, H. Yang, W. Kim, J. Valiando, M. Ohh, A. Salic, J. M. Asara, W. S. Lane and W. G. Kaelin, Jr. (2001). "HIFalpha targeted for VHL-mediated destruction by proline hydroxylation: implications for O<sub>2</sub> sensing." *Science* **292**(5516): 464-468. <http://doi.org/10.1126/science.1059817>

Jaakkola, P., D. R. Mole, Y. M. Tian, M. I. Wilson, J. Gielbert, S. J. Gaskell, A. von Kriegsheim, H. F. Hebestreit, M. Mukherji, C. J. Schofield, P. H. Maxwell, C. W. Pugh and P. J. Ratcliffe (2001). "Targeting of HIF-alpha to the von Hippel-Lindau ubiquitylation complex by O<sub>2</sub>-regulated prolyl hydroxylation." *Science* **292**(5516): 468-472. <http://doi.org/10.1126/science.1059796>

Jain, M., R. Nilsson, S. Sharma, N. Madhusudhan, T. Kitami, A. L. Souza, R. Kafri, M. W. Kirschner, C. B. Clish and V. K. Mootha (2012). "Metabolite profiling identifies a key role for glycine in rapid cancer cell proliferation." *Science* **336**(6084): 1040-1044. <http://doi.org/10.1126/science.1218595>

Jia, X. Q., S. Zhang, H. J. Zhu, W. Wang, J. H. Zhu, X. D. Wang and J. F. Qiang (2016). "Increased Expression of PHGDH and Prognostic Significance in Colorectal Cancer." *Transl Oncol* **9**(3): 191-196. <http://doi.org/10.1016/j.tranon.2016.03.006>

Jinzaki, M., A. Tanimoto, M. Mukai, E. Ikeda, S. Kobayashi, Y. Yuasa, Y. Narimatsu and M. Murai (2000). "Double-phase helical CT of small renal parenchymal neoplasms: correlation with pathologic findings and tumor angiogenesis." *J Comput Assist Tomogr* **24**(6): 835-842.

Joshi, S., D. Tolkunov, H. Aviv, A. A. Hakimi, M. Yao, J. J. Hsieh, S. Ganesan, C. S. Chan and E. White (2015). "The Genomic Landscape of Renal Oncocytoma Identifies a Metabolic Barrier to Tumorigenesis." *Cell Rep* **13**(9): 1895-1908. <http://doi.org/10.1016/j.celrep.2015.10.059>

Ju, Y. S., L. B. Alexandrov, M. Gerstung, I. Martincorena, S. Nik-Zainal, M. Ramakrishna, H. R. Davies, E. Papaemmanuil, G. Gundem, A. Shlien, N. Bolli, S. Behjati, P. S. Tarpey, J. Nangalia, C. E. Massie, A. P. Butler, J. W. Teague, G. S. Vassiliou, A. R. Green, M. Q. Du, A. Unnikrishnan, J. E. Pimanda, B. T. Teh, N. Munshi, M. Greaves, P. Vyas, A. K. El-Naggar, T. Santarius, V. P. Collins, R. Grundy, J. A. Taylor, D. N. Hayes, D. Malkin, I. B. C. Group, I. C. M. D. Group, I. P. C. Group, C. S. Foster, A. Y. Warren, H. C. Whitaker, D. Brewer, R. Eeles, C. Cooper, D. Neal, T. Visakorpi, W. B. Isaacs, G. S. Bova, A. M. Flanagan, P. A. Furtreal, A. G. Lynch, P. F. Chinnery, U. McDermott, M. R. Stratton and P. J. Campbell (2014). "Origins and functional consequences of somatic mitochondrial DNA mutations in human cancer." *eLife* **3**: <http://doi.org/10.7554/eLife.02935>

Kalyanaraman, B., B. P. Dranka, M. Hardy, R. Michalski and J. Zielonka (2014). "HPLC-based monitoring of products formed from hydroethidine-based fluorogenic probes--the ultimate approach for intra- and extracellular superoxide detection." *Biochim Biophys Acta* **1840**(2): 739-744. <http://doi.org/10.1016/j.bbagen.2013.05.008>

Kalyanaraman, B., M. Hardy, R. Podsiadly, G. Cheng and J. Zielonka (2017). "Recent developments in detection of superoxide radical anion and hydrogen peroxide: Opportunities, challenges, and implications in redox signaling." *Arch Biochem Biophys* **617**(Supplement C): 38-47. <http://doi.org/10.1016/j.abb.2016.08.021>

## References

- Kaplowitz, N., T. Y. Aw and M. Ookhtens (1985). "The regulation of hepatic glutathione." *Annu Rev Pharmacol Toxicol* **25:** 715-744.  
<http://doi.org/10.1146/annurev.pa.25.040185.003435>
- Kim, J., J. Kim and J. S. Bae (2016). "ROS homeostasis and metabolism: a critical liaison for cancer therapy." *Exp Mol Med* **48**(11): e269. <http://doi.org/10.1038/emm.2016.119>
- Kulak, N. A., G. Pichler, I. Paron, N. Nagaraj and M. Mann (2014). "Minimal, encapsulated proteomic-sample processing applied to copy-number estimation in eukaryotic cells." *Nat Methods* **11**(3): 319-324. <http://doi.org/10.1038/nmeth.2834>
- Kurschner, G., Q. Zhang, R. Clima, Y. Xiao, J. F. Busch, E. Kilic, K. Jung, N. Berndt, S. Bulik, H. G. Holzhutter, G. Gasparre, M. Attimonelli, M. Babu and D. Meierhofer (2017). "Renal oncocytoma characterized by the defective complex I of the respiratory chain boosts the synthesis of the ROS scavenger glutathione." *Oncotarget* **8**(62): 105882-105904. <http://doi.org/10.18632/oncotarget.22413>
- Latif, F., K. Tory, J. Gnarra, M. Yao, F. M. Duh, M. L. Orcutt, T. Stackhouse, I. Kuzmin, W. Modi, L. Geil and et al. (1993). "Identification of the von Hippel-Lindau disease tumor suppressor gene." *Science* **260**(5112): 1317-1320. <http://doi.org/10.1126/science.8493574>
- Leman, G., N. Gueguen, V. Desquiret-Dumas, M. S. Kane, C. Wetterwald, S. Chupin, A. Chevrollier, A. S. Lebre, J. P. Bonnefont, M. Barth, P. Amati-Bonneau, C. Verny, D. Henrion, D. Bonneau, P. Reynier and V. Procaccio (2015). "Assembly defects induce oxidative stress in inherited mitochondrial complex I deficiency." *Int J Biochem Cell Biol* **65:** 91-103. <http://doi.org/10.1016/j.biocel.2015.05.017>
- Li, B. and C. N. Dewey (2011). "RSEM: accurate transcript quantification from RNA-Seq data with or without a reference genome." *BMC Bioinformatics* **12:** 323. <http://doi.org/10.1186/1471-2105-12-323>
- Li, B., B. Qiu, D. S. Lee, Z. E. Walton, J. D. Ochocki, L. K. Mathew, A. Mancuso, T. P. Gade, B. Keith, I. Nissim and M. C. Simon (2014). "Fructose-1,6-bisphosphatase opposes renal carcinoma progression." *Nature* **513**(7517): 251-255. <http://doi.org/10.1038/nature13557>

Li, N., K. Ragheb, G. Lawler, J. Sturgis, B. Rajwa, J. A. Melendez and J. P. Robinson (2003). "Mitochondrial complex I inhibitor rotenone induces apoptosis through enhancing mitochondrial reactive oxygen species production." *J Biol Chem* **278**(10): 8516-8525. <http://doi.org/10.1074/jbc.M210432200>

Li, Q., Y. Li, J. Xu, S. Wang, Y. Xu, X. Li and S. Cai (2017). "Aldolase B Overexpression is Associated with Poor Prognosis and Promotes Tumor Progression by Epithelial-Mesenchymal Transition in Colorectal Adenocarcinoma." *Cell Physiol Biochem* **42**(1): 397-406. <http://doi.org/10.1159/000477484>

Li, S., B. M. Shuch and M. B. Gerstein (2017). "Whole-genome analysis of papillary kidney cancer finds significant noncoding alterations." *PLoS Genet* **13**(3): e1006685. <http://doi.org/10.1371/journal.pgen.1006685>

Linehan, W. M., L. S. Schmidt, D. R. Crooks, D. Wei, R. Srinivasan, M. Lang and C. J. Ricketts (2019). "The Metabolic Basis of Kidney Cancer." *Cancer Discov* **9**(8): 1006-1021. <http://doi.org/10.1158/2159-8290.CD-18-1354>

Linehan, W. M., J. Vasselli, R. Srinivasan, M. M. Walther, M. Merino, P. Choyke, C. Vocke, L. Schmidt, J. S. Isaacs, G. Glenn, J. Toro, B. Zbar, D. Bottaro and L. Neckers (2004). "Genetic basis of cancer of the kidney: disease-specific approaches to therapy." *Clin Cancer Res* **10**(18 Pt 2): 6282S-6289S. <http://doi.org/10.1158/1078-0432.CCR-050013>

Lopez-Beltran, A., J. C. Carrasco, L. Cheng, M. Scarpelli, Z. Kirkali and R. Montironi (2009). "2009 update on the classification of renal epithelial tumors in adults." *Int J Urol* **16**(5): 432-443. <http://doi.org/10.1111/j.1442-2042.2009.02302.x>

Lopez-Beltran, A., M. Scarpelli, R. Montironi and Z. Kirkali (2006). "2004 WHO classification of the renal tumors of the adults." *Eur Urol* **49**(5): 798-805. <http://doi.org/10.1016/j.eururo.2005.11.035>

Lu, C. and C. B. Thompson (2012). "Metabolic regulation of epigenetics." *Cell Metab* **16**(1): 9-17. <http://doi.org/10.1016/j.cmet.2012.06.001>

Lu, S. C. (2009). "Regulation of glutathione synthesis." *Mol Aspects Med* **30**(1-2): 42-59. <http://doi.org/10.1016/j.mam.2008.05.005>

## References

- Ludwig, C., L. Gillet, G. Rosenberger, S. Amon, B. C. Collins and R. Aebersold (2018). "Data-independent acquisition-based SWATH-MS for quantitative proteomics: a tutorial." *Mol Syst Biol* **14**(8): e8126. <http://doi.org/10.15252/msb.20178126>
- Makarov, A. (2000). "Electrostatic axially harmonic orbital trapping: a high-performance technique of mass analysis." *Anal Chem* **72**(6): 1156-1162. <http://doi.org/10.1021/ac991131p>
- Makarov, A., E. Denisov, A. Kholomeev, W. Balschun, O. Lange, K. Strupat and S. Horning (2006). "Performance evaluation of a hybrid linear ion trap/orbitrap mass spectrometer." *Anal Chem* **78**(7): 2113-2120. <http://doi.org/10.1021/ac0518811>
- Makarov, A., E. Denisov, O. Lange and S. Horning (2006). "Dynamic range of mass accuracy in LTQ Orbitrap hybrid mass spectrometer." *J Am Soc Mass Spectrom* **17**(7): 977-982. <http://doi.org/10.1016/j.jasms.2006.03.006>
- Mann, M., R. C. Hendrickson and A. Pandey (2001). "Analysis of proteins and proteomes by mass spectrometry." *Annu Rev Biochem* **70**: 437-473. <http://doi.org/10.1146/annurev.biochem.70.1.437>
- Mayr, J. A., D. Meierhofer, F. Zimmermann, R. Feichtinger, C. Kogler, M. Ratschek, N. Schmeller, W. Sperl and B. Kofler (2008). "Loss of complex I due to mitochondrial DNA mutations in renal oncocytoma." *Clin Cancer Res* **14**(8): 2270-2275. <http://doi.org/10.1158/1078-0432.CCR-07-4131>
- Meierhofer, D., M. Halbach, N. E. Sen, S. Gispert and G. Auburger (2016). "Ataxin-2 (Atxn2)-Knock-Out Mice Show Branched Chain Amino Acids and Fatty Acids Pathway Alterations." *Mol Cell Proteomics* **15**(5): 1728-1739. <http://doi.org/10.1074/mcp.M115.056770>
- Meierhofer, D., J. A. Mayr, U. Foetschl, A. Berger, K. Fink, N. Schmeller, G. W. Hacker, C. Hauser-Kronberger, B. Kofler and W. Sperl (2004). "Decrease of mitochondrial DNA content and energy metabolism in renal cell carcinoma." *Carcinogenesis* **25**(6): 1005-1010. <http://doi.org/10.1093/carcin/bgh104>

Meister, A. (1988). "On the discovery of glutathione." *Trends Biochem Sci* **13**(5): 185-188.  
[http://doi.org/10.1016/0968-0004\(88\)90148-x](http://doi.org/10.1016/0968-0004(88)90148-x)

Meister, A. and M. E. Anderson (1983). "Glutathione." *Annu Rev Biochem* **52**: 711-760.  
<http://doi.org/10.1146/annurev.bi.52.070183.003431>

Michalski, R., J. Zielonka, M. Hardy, J. Joseph and B. Kalyanaraman (2013). "Hydropropidine: a novel, cell-impermeant fluorogenic probe for detecting extracellular superoxide." *Free Radic Biol Med* **54**: 135-147.  
<http://doi.org/10.1016/j.freeradbiomed.2012.09.018>

Moch, H., A. L. Cubilla, P. A. Humphrey, V. E. Reuter and T. M. Ulbright (2016). "The 2016 WHO Classification of Tumours of the Urinary System and Male Genital Organs-Part A: Renal, Penile, and Testicular Tumours." *Eur Urol* **70**(1): 93-105.  
<http://doi.org/10.1016/j.eururo.2016.02.029>

Morrison, J. D. (1991). "Personal reminiscences of forty years of mass spectrometry in Australia." *Organic Mass Spectrometry* **26**(4): 183-194.  
<http://doi.org/10.1002/oms.1210260404>

Motzer, R. J., J. Bacik and M. Mazumdar (2004). "Prognostic factors for survival of patients with stage IV renal cell carcinoma: memorial sloan-kettering cancer center experience." *Clin Cancer Res* **10**(18 Pt 2): 6302S-6303S. <http://doi.org/10.1158/1078-0432.CCR-040031>

Nakajima, R., S. Nozaki, T. Kondo, Y. Nagashima, K. Abe and S. Sakai (2017). "Evaluation of renal cell carcinoma histological subtype and fuhrman grade using (18)F-fluorodeoxyglucose-positron emission tomography/computed tomography." *Eur Radiol* **27**(11): 4866-4873. <http://doi.org/10.1007/s00330-017-4875-z>

Ng, K. L., C. Morais, A. Bernard, N. Saunders, H. Samaratunga, G. Gobe and S. Wood (2016). "A systematic review and meta-analysis of immunohistochemical biomarkers that differentiate chromophobe renal cell carcinoma from renal oncocytoma." *J Clin Pathol* **69**(8): 661-671. <http://doi.org/10.1136/jclinpath-2015-203585>

## References

- Ni, Y., M. A. Hagras, V. Konstantopoulou, J. A. Mayr, A. A. Stuchebrukhov and D. Meierhofer (2019). "Mutations in NDUFS1 Cause Metabolic Reprogramming and Disruption of the Electron Transfer." *Cells* **8**(10): <http://doi.org/10.3390/cells8101149>
- Noguchi, S., Y. Nagashima, T. Shuin, Y. Kubota, H. Kitamura, M. Yao and M. Hosaka (1995). "Renal oncocytoma containing "chromophobe" cells." *Int J Urol* **2**(4): 279-280.
- Pal, S. K., S. M. Ali, E. Yakirevich, D. M. Geynisman, J. A. Karam, J. A. Elvin, G. M. Frampton, X. Huang, D. I. Lin, M. Rosenzweig, D. Lipson, P. J. Stephens, J. S. Ross, V. A. Miller, N. Agarwal, B. Shuch, T. K. Choueiri and J. H. Chung (2018). "Characterization of Clinical Cases of Advanced Papillary Renal Cell Carcinoma via Comprehensive Genomic Profiling." *Eur Urol* **73**(1): 71-78. <http://doi.org/10.1016/j.eururo.2017.05.033>
- Pavlovich, C. P., R. L. Grubb, 3rd, K. Hurley, G. M. Glenn, J. Toro, L. S. Schmidt, C. Torres-Cabala, M. J. Merino, B. Zbar, P. Choyke, M. M. Walther and W. M. Linehan (2005). "Evaluation and management of renal tumors in the Birt-Hogg-Dube syndrome." *J Urol* **173**(5): 1482-1486. <http://doi.org/10.1097/01.ju.0000154629.45832.30>
- Penhoet, E., T. Rajkumar and W. J. Rutter (1966). "Multiple forms of fructose diphosphate aldolase in mammalian tissues." *Proc Natl Acad Sci U S A* **56**(4): 1275-1282. <http://doi.org/10.1073/pnas.56.4.1275>
- Pignot, G., C. Elie, S. Conquy, A. Vieillefond, T. Flam, M. Zerbib, B. Debre and D. Amsellem-Ouazana (2007). "Survival analysis of 130 patients with papillary renal cell carcinoma: prognostic utility of type 1 and type 2 subclassification." *Urology* **69**(2): 230-235. <http://doi.org/10.1016/j.urology.2006.09.052>
- Pollard, P. J., J. J. Briere, N. A. Alam, J. Barwell, E. Barclay, N. C. Wortham, T. Hunt, M. Mitchell, S. Olpin, S. J. Moat, I. P. Hargreaves, S. J. Heales, Y. L. Chung, J. R. Griffiths, A. Dalgleish, J. A. McGrath, M. J. Gleeson, S. V. Hodgson, R. Poulsom, P. Rustin and I. P. Tomlinson (2005). "Accumulation of Krebs cycle intermediates and over-expression of HIF1alpha in tumours which result from germline FH and SDH mutations." *Hum Mol Genet* **14**(15): 2231-2239. <http://doi.org/10.1093/hmg/ddi227>
- Posadas, E. M., S. Limvorasak and R. A. Figlin (2017). "Targeted therapies for renal cell carcinoma." *Nat Rev Nephrol* **13**(8): 496-511. <http://doi.org/10.1038/nrneph.2017.82>

Pote, N., A. Vieillefond, J. Couturier, S. Arrufat, I. Metzger, N. B. Delongchamps, P. Campano, F. Mege-Lechevallier, V. Molinie and M. Sibony (2013). "Hybrid oncocytic/chromophobe renal cell tumours do not display genomic features of chromophobe renal cell carcinomas." *Virchows Arch* **462**(6): 633-638. <http://doi.org/10.1007/s00428-013-1422-4>

Priolo, C., D. Khabibullin, E. Reznik, H. Filippakis, B. Ogorek, T. R. Kavanagh, J. Nijmeh, Z. T. Herbert, J. M. Asara, D. J. Kwiatkowski, C. L. Wu and E. P. Henske (2018). "Impairment of gamma-glutamyl transferase 1 activity in the metabolic pathogenesis of chromophobe renal cell carcinoma." *Proc Natl Acad Sci U S A* **115**(27): E6274-E6282. <http://doi.org/10.1073/pnas.1710849115>

Przybycin, C. G., A. M. Cronin, F. Darvishian, A. Gopalan, H. A. Al-Ahmadie, S. W. Fine, Y. B. Chen, M. Bernstein, P. Russo, V. E. Reuter and S. K. Tickoo (2011). "Chromophobe renal cell carcinoma: a clinicopathologic study of 203 tumors in 200 patients with primary resection at a single institution." *Am J Surg Pathol* **35**(7): 962-970. <http://doi.org/10.1097/PAS.0b013e31821a455d>

Ren, X., L. Zou, X. Zhang, V. Branco, J. Wang, C. Carvalho, A. Holmgren and J. Lu (2017). "Redox Signaling Mediated by Thioredoxin and Glutathione Systems in the Central Nervous System." *Antioxid Redox Signal* **27**(13): 989-1010. <http://doi.org/10.1089/ars.2016.6925>

Repnik, U., M. H. Cesen and B. Turk (2013). "The endolysosomal system in cell death and survival." *Cold Spring Harb Perspect Biol* **5**(1): a008755. <http://doi.org/10.1101/cshperspect.a008755>

Riazalhosseini, Y. and M. Lathrop (2016). "Precision medicine from the renal cancer genome." *Nat Rev Nephrol* **12**(11): 655-666. <http://doi.org/10.1038/nrneph.2016.133>

Ricketts, C. J., A. A. De Cubas, H. Fan, C. C. Smith, M. Lang, E. Reznik, R. Bowlby, E. A. Gibb, R. Akbani, R. Beroukhim, D. P. Bottaro, T. K. Choueiri, R. A. Gibbs, A. K. Godwin, S. Haake, A. A. Hakimi, E. P. Henske, J. J. Hsieh, T. H. Ho, R. S. Kanchi, B. Krishnan, D. J. Kwiatkowski, W. Lui, M. J. Merino, G. B. Mills, J. Myers, M. L. Nickerson, V. E. Reuter, L. S. Schmidt, C. S. Shelley, H. Shen, B. Shuch, S. Signoretti, R. Srinivasan, P. Tamboli, G. Thomas, B. G. Vincent, C. D. Vocke, D. A. Wheeler, L. Yang, W. Y. Kim, A. G. Robertson, N. Cancer Genome Atlas Research, P. T. Spellman, W. K. Rathmell and W. M. Linehan

## References

- (2018). "The Cancer Genome Atlas Comprehensive Molecular Characterization of Renal Cell Carcinoma." *Cell Rep* **23**(1): 313-326 e315. <http://doi.org/10.1016/j.celrep.2018.03.075>
- Roberts, L. D., A. L. Souza, R. E. Gerszten and C. B. Clish (2012). "Targeted metabolomics." *Current protocols in molecular biology Chapter 30*: Unit 30 32 31-24. <http://doi.org/10.1002/0471142727.mb3002s98>
- Robinson, K. M., M. S. Janes, M. Pehar, J. S. Monette, M. F. Ross, T. M. Hagen, M. P. Murphy and J. S. Beckman (2006). "Selective fluorescent imaging of superoxide in vivo using ethidium-based probes." *Proc Natl Acad Sci U S A* **103**(41): 15038-15043. <http://doi.org/10.1073/pnas.0601945103>
- Rosenberger, G., Y. Liu, H. L. Rost, C. Ludwig, A. Buil, A. Bensimon, M. Soste, T. D. Spector, E. T. Dermitzakis, B. C. Collins, L. Malmstrom and R. Aebersold (2017). "Inference and quantification of peptidoforms in large sample cohorts by SWATH-MS." *Nat Biotechnol* **35**(8): 781-788. <http://doi.org/10.1038/nbt.3908>
- Sato, Y., T. Yoshizato, Y. Shiraishi, S. Maekawa, Y. Okuno, T. Kamura, T. Shimamura, A. Sato-Otsubo, G. Nagae, H. Suzuki, Y. Nagata, K. Yoshida, A. Kon, Y. Suzuki, K. Chiba, H. Tanaka, A. Niida, A. Fujimoto, T. Tsunoda, T. Morikawa, D. Maeda, H. Kume, S. Sugano, M. Fukayama, H. Aburatani, M. Sanada, S. Miyano, Y. Homma and S. Ogawa (2013). "Integrated molecular analysis of clear-cell renal cell carcinoma." *Nat Genet* **45**(8): 860-867. <http://doi.org/10.1038/ng.2699>
- Schaeffeler, E., F. Buttner, A. Reustle, V. Klumpp, S. Winter, S. Rausch, P. Fisel, J. Hennenlotter, S. Kruck, A. Stenzl, J. Wahrheit, D. Sonntag, M. Scharpf, F. Fend, A. Agaimy, A. Hartmann, J. Bedke and M. Schwab (2018). "Metabolic and Lipidomic Reprogramming in Renal Cell Carcinoma Subtypes Reflects Regions of Tumor Origin." *Eur Urol Focus*: <http://doi.org/10.1016/j.euf.2018.01.016>
- Schrime-Rutledge, A. C., S. G. Codreanu, S. D. Sherrod and J. A. McLean (2016). "Untargeted Metabolomics Strategies-Challenges and Emerging Directions." *J Am Soc Mass Spectrom* **27**(12): 1897-1905. <http://doi.org/10.1007/s13361-016-1469-y>

Shibata, H. and T. Yagi (1996). "Rate assay of N-acetyl-beta-D-hexosaminidase with 4-nitrophenyl N-acetyl-beta-D-glucosaminide as an artificial substrate." Clinica Chimica Acta **251**(1): 53-64. [http://doi.org/10.1016/0009-8981\(96\)06292-4](http://doi.org/10.1016/0009-8981(96)06292-4)

Siegel, R. L., K. D. Miller and A. Jemal (2019). "Cancer statistics, 2019." CA Cancer J Clin **69**(1): 7-34. <http://doi.org/10.3322/caac.21551>

Simic, T., D. Dragicevic, A. Savic-Radojevic, S. Cimbaljevic, C. Tulic and J. Mimic-Oka (2007). "Serum gamma glutamyl-transferase is a sensitive but unspecific marker of metastatic renal cell carcinoma." Int J Urol **14**(4): 289-293. <http://doi.org/10.1111/j.1442-2042.2006.01719.x>

Simonnet, H., J. Demont, K. Pfeiffer, L. Guenaneche, R. Bouvier, U. Brandt, H. Schagger and C. Godinot (2003). "Mitochondrial complex I is deficient in renal oncocytomas." Carcinogenesis **24**(9): 1461-1466. <http://doi.org/10.1093/carcin/bgg109>

Sipos, K., H. Lange, Z. Fekete, P. Ullmann, R. Lill and G. Kispal (2002). "Maturation of cytosolic iron-sulfur proteins requires glutathione." J Biol Chem **277**(30): 26944-26949. <http://doi.org/10.1074/jbc.M200677200>

Spinazzi, M., A. Casarin, V. Pertegato, L. Salviati and C. Angelini (2012). "Assessment of mitochondrial respiratory chain enzymatic activities on tissues and cultured cells." Nat Protoc **7**(6): 1235-1246. <http://doi.org/10.1038/nprot.2012.058>

Stahl, D. C., K. M. Swiderek, M. T. Davis and T. D. Lee (1996). "Data-controlled automation of liquid chromatography/tandem mass spectrometry analysis of peptide mixtures." J Am Soc Mass Spectrom **7**(6): 532-540. [http://doi.org/10.1016/1044-0305\(96\)00057-8](http://doi.org/10.1016/1044-0305(96)00057-8)

Steffens, S., M. Janssen, F. C. Roos, F. Becker, S. Schumacher, C. Seidel, G. Wegener, J. W. Thuroff, R. Hofmann, M. Stockle, S. Siemer, M. Schrader, A. Hartmann, M. A. Kuczyk, K. Junker and A. J. Schrader (2012). "Incidence and long-term prognosis of papillary compared to clear cell renal cell carcinoma--a multicentre study." Eur J Cancer **48**(15): 2347-2352. <http://doi.org/10.1016/j.ejca.2012.05.002>

Subramanian, A., P. Tamayo, V. K. Mootha, S. Mukherjee, B. L. Ebert, M. A. Gillette, A. Paulovich, S. L. Pomeroy, T. R. Golub, E. S. Lander and J. P. Mesirov (2005). "Gene set

## References

enrichment analysis: a knowledge-based approach for interpreting genome-wide expression profiles." Proc Natl Acad Sci U S A **102**(43): 15545-15550.  
<http://doi.org/10.1073/pnas.0506580102>

Sullivan, L. B., E. Martinez-Garcia, H. Nguyen, A. R. Mullen, E. Dufour, S. Sudarshan, J. D. Licht, R. J. Deberardinis and N. S. Chandel (2013). "The proto-oncometabolite fumarate binds glutathione to amplify ROS-dependent signaling." Mol Cell **51**(2): 236-248.  
<http://doi.org/10.1016/j.molcel.2013.05.003>

Terzyan, S. S., A. W. Burgett, A. Heroux, C. A. Smith, B. H. Mooers and M. H. Hanigan (2015). "Human gamma-Glutamyl Transpeptidase 1: STRUCTURES OF THE FREE ENZYME, INHIBITOR-BOUND TETRAHEDRAL TRANSITION STATES, AND GLUTAMATE-BOUND ENZYME REVEAL NOVEL MOVEMENT WITHIN THE ACTIVE SITE DURING CATALYSIS." J Biol Chem **290**(28): 17576-17586.  
<http://doi.org/10.1074/jbc.M115.659680>

Thoenes, W., S. Storkel and H. J. Rumpelt (1985). "Human chromophobe cell renal carcinoma." Virchows Arch B Cell Pathol Incl Mol Pathol **48**(3): 207-217.

Thyagarajan, A. and R. P. Sahu (2018). "Potential Contributions of Antioxidants to Cancer Therapy: Immunomodulation and Radiosensitization." Integrative cancer therapies **17**(2): 210-216. <http://doi.org/10.1177/1534735416681639>

Tian, Y. F., P. L. Hsieh, C. Y. Lin, D. P. Sun, M. J. Sheu, C. C. Yang, L. C. Lin, H. L. He, J. Solorzano, C. F. Li and I. W. Chang (2017). "High Expression of Aldolase B Confers a Poor Prognosis for Rectal Cancer Patients Receiving Neoadjuvant Chemoradiotherapy." J Cancer **8**(7): 1197-1204. <http://doi.org/10.7150/jca.18197>

Tickoo, S. K., M. W. Lee, J. N. Eble, M. Amin, T. Christopherson, R. J. Zarbo and M. B. Amin (2000). "Ultrastructural observations on mitochondria and microvesicles in renal oncocytoma, chromophobe renal cell carcinoma, and eosinophilic variant of conventional (clear cell) renal cell carcinoma." Am J Surg Pathol **24**(9): 1247-1256.  
<http://doi.org/10.1097/00000478-200009000-00008>

Tomlinson, I., N. Alam, A. Rowan, E. Barclay, E. Jaeger, D. Kelsell, I. Leigh, P. Gorman, H. Lamlum and S. Rahman (2002). "Multiple Leiomyoma Consortium: Germline mutations in

FH predispose to dominantly inherited uterine fibroids, skin leiomyomata and papillary renal cell cancer." Nat Genet **30**(4): 406-410.

Tyanova, S., T. Temu, P. Sinitcyn, A. Carlson, M. Y. Hein, T. Geiger, M. Mann and J. Cox (2016). "The Perseus computational platform for comprehensive analysis of (prote)omics data." Nat Methods **13**(9): 731-740. <http://doi.org/10.1038/nmeth.3901>

Valera, V. A., T. E. Li-Ning, B. A. Walter, D. D. Roberts, W. M. Linehan and M. J. Merino (2010). "Protein expression profiling in the spectrum of renal cell carcinomas." J Cancer **1**: 184-196.

Venable, J. D., M. Q. Dong, J. Wohlschlegel, A. Dillin and J. R. Yates (2004). "Automated approach for quantitative analysis of complex peptide mixtures from tandem mass spectra." Nat Methods **1**(1): 39-45. <http://doi.org/10.1038/nmeth705>

Vera-Badillo, F. E., E. Conde and I. Duran (2012). "Chromophobe renal cell carcinoma: a review of an uncommon entity." Int J Urol **19**(10): 894-900. <http://doi.org/10.1111/j.1442-2042.2012.03079.x>

Vizcaino, J. A., R. G. Cote, A. Csordas, J. A. Dianes, A. Fabregat, J. M. Foster, J. Griss, E. Alpi, M. Birim, J. Contell, G. O'Kelly, A. Schoenegger, D. Ovelleiro, Y. Perez-Riverol, F. Reisinger, D. Rios, R. Wang and H. Hermjakob (2013). "The PRoteomics IDEntifications (PRIDE) database and associated tools: status in 2013." Nucleic Acids Res **41**(Database issue): D1063-1069. <http://doi.org/10.1093/nar/gks1262>

Volpe, A., G. Novara, A. Antonelli, R. Bertini, M. Billia, G. Carmignani, S. C. Cunico, N. Longo, G. Martignoni, A. Minervini, V. Mirone, A. Simonato, C. Terrone, F. Zattoni, V. Ficarra, Surveillance, P. Treatment Update on Renal Neoplasms and F. Leading Urological No-Profit Foundation for Advanced Research (2012). "Chromophobe renal cell carcinoma (RCC): oncological outcomes and prognostic factors in a large multicentre series." BJU Int **110**(1): 76-83. <http://doi.org/10.1111/j.1464-410X.2011.10690.x>

Warburg, O. (1956). "On the origin of cancer cells." Science **123**(3191): 309-314.

Wasinger, V. C., S. J. Cordwell, A. Cerpa-Poljak, J. X. Yan, A. A. Gooley, M. R. Wilkins, M. W. Duncan, R. Harris, K. L. Williams and I. Humphery-Smith (1995). "Progress with gene-

## References

product mapping of the Mollicutes: Mycoplasma genitalium." ELECTROPHORESIS **16**(7): 1090-1094. <http://doi.org/10.1002/elps.11501601185>

Wellen, K. E. and C. B. Thompson (2012). "A two-way street: reciprocal regulation of metabolism and signalling." Nat Rev Mol Cell Biol **13**(4): 270-276. <http://doi.org/10.1038/nrm3305>

Wettersten, H. I., O. A. Aboud, P. N. Lara, Jr. and R. H. Weiss (2017). "Metabolic reprogramming in clear cell renal cell carcinoma." Nat Rev Nephrol **13**(7): 410-419. <http://doi.org/10.1038/nrneph.2017.59>

Wettersten, H. I., A. A. Hakimi, D. Morin, C. Bianchi, M. E. Johnstone, D. R. Donohoe, J. F. Trott, O. A. Aboud, S. Stirdvant, B. Neri, R. Wolfert, B. Stewart, R. Perego, J. J. Hsieh and R. H. Weiss (2015). "Grade-Dependent Metabolic Reprogramming in Kidney Cancer Revealed by Combined Proteomics and Metabolomics Analysis." Cancer Res **75**(12): 2541-2552. <http://doi.org/10.1158/0008-5472.CAN-14-1703>

Xiao, Y., R. Clima, J. F. Busch, A. Rabien, E. Kilic, S. Villegas, S. Türkmen, B. Timmermann, M. Attimonelli, K. Jung and D. Meierhofer (2019). "Metabolic reprogramming and elevation of glutathione in chromophobe renal cell carcinomas." bioRxiv: 649046. <http://doi.org/10.1101/649046>

Xiao, Y. and D. Meierhofer (2019). "Glutathione Metabolism in Renal Cell Carcinoma Progression and Implications for Therapies." Int J Mol Sci **20**(15): <http://doi.org/10.3390/ijms20153672>

Yang, Y., C. D. Vocke, C. J. Ricketts, D. Wei, H. M. Padilla-Nash, M. Lang, C. Sourbier, J. K. Killian, S. L. Boyle, R. Worrell, P. S. Meltzer, T. Ried, M. J. Merino, A. R. Metwalli and W. M. Linehan (2017). "Genomic and metabolic characterization of a chromophobe renal cell carcinoma cell line model (UOK276)." Genes Chromosomes Cancer **56**(10): 719-729. <http://doi.org/10.1002/gcc.22476>

Ye, J., G. Coulouris, I. Zaretskaya, I. Cutcutache, S. Rozen and T. L. Madden (2012). "Primer-BLAST: a tool to design target-specific primers for polymerase chain reaction." BMC Bioinformatics **13**: 134. <http://doi.org/10.1186/1471-2105-13-134>

Yusenko, M. V. (2010). "Molecular pathology of chromophobe renal cell carcinoma: a review." Int J Urol **17**(7): 592-600. <http://doi.org/10.1111/j.1442-2042.2010.02558.x>

Zhang, X., P. Liu, C. Zhang, D. Chiewchengchol, F. Zhao, H. Yu, J. Li, H. Kambara, K. Y. Luo, A. Venkataraman, Z. Zhou, W. Zhou, H. Zhu, L. Zhao, J. Sakai, Y. Chen, Y. S. Ho, B. Bajrami, B. Xu, L. E. Silberstein, T. Cheng, Y. Xu, Y. Ke and H. R. Luo (2017). "Positive Regulation of Interleukin-1beta Bioactivity by Physiological ROS-Mediated Cysteine S-Glutathionylation." Cell Rep **20**(1): 224-235. <http://doi.org/10.1016/j.celrep.2017.05.070>

Zielonka, J., M. Hardy and B. Kalyanaraman (2009). "HPLC study of oxidation products of hydroethidine in chemical and biological systems: ramifications in superoxide measurements." Free Radic Biol Med **46**(3): 329-338. <http://doi.org/10.1016/j.freeradbiomed.2008.10.031>

Zippel, J. (1941). "Zur kenntnis der onkocyten." Virchows Archiv für pathologische Anatomie und Physiologie und für klinische Medizin **308**(2): 360-382.

Zmijewski, J. W., S. Banerjee, H. Bae, A. Friggeri, E. R. Lazarowski and E. Abraham (2010). "Exposure to hydrogen peroxide induces oxidation and activation of AMP-activated protein kinase." J Biol Chem **285**(43): 33154-33164. <http://doi.org/10.1074/jbc.M110.143685>

## List of figures

Figure 1. Histological sections of different subtypes of renal cell carcinoma. ....	1
Figure 2. FDG-PET/CT of ccRCC, pRCC, and chRCC. ....	5
Figure 3. Clinical manifestations of Birt-Hogg-Dubé syndrome. ....	7
Figure 4. Schematic overview of glutathione (GSH) metabolism.....	8
Figure 5. Products formed from HE, mito-HE, and HPr+.....	11
Figure 6. Schematic representation of the triple quadrupole mass spectrometer. ....	12
Figure 7. Different scan modes of triple quadrupole mass spectrometer.....	13
Figure 8. The schematic of an orbitrap mass spectrometer. ....	14
Figure 9. An illustration of data-dependent and data-independent modes of acquisition. ....	16
Figure 10. The proteome and metabolome profiling workflow of chRCC.....	43
Figure 11. Exome-based copy number variation analysis in chRCC. ....	44
Figure 12. The proteomic analysis of chRCC.....	45
Figure 13. Gene set enrichment analysis of the proteome revealed regulated pathways in chRCC. ....	46
Figure 14. Quantified metabolites by targeted metabolome profiling of chRCC. ....	48
Figure 15. Distinct regulation of the OXPHOS complexes in chRCC and RO. ....	50
Figure 16. Comparison of the RNA expression versus the protein abundance between chRCC and kidney controls.....	52
Figure 17. The level of glutathione boosted in ChRCC. ....	54

Figure 18. Glutathione levels in plasma and urine cannot be used as a marker to distinguish RCCs from controls.....	55
Figure 19. Identified somatic mtDNA mutations and mtDNA copy number evaluation in chRCC.....	57
Figure 20. Correlation between the mtDNA content with proteins and transcripts for the respiratory chain and glutathione levels.....	59
Figure 21. Stalled gluconeogenetic pathway in chRCC. ....	61
Figure 22. Regulation of amino acid metabolism in chRCC. ....	63
Figure 23. ChRCC cells activated endocytosis when amino acids were depleted....	66
Figure 24. Chemical inhibition of the PLCG pathway decreases the endocytosis of protein in chRCC cells.....	68
Figure 25. Other unlabeled essential amino acids also decrease after chemical inhibition of the PLCG pathway. ....	69
Figure 26. Specific fragment spectra (MS <sup>2</sup> ) obtained for hydroethidine probes and its O <sub>2</sub> <sup>-</sup> specific oxidized product. ....	71
Figure 27. MRM transitions of three fluorogenic probes and their oxidation products, separated on a reverse-phase C18 column.....	72
Figure 28. Stability tests for fluorogenic probes. ....	73
Figure 29. ROS determination of fluorogenic probes after ROS stimulation with chemicals.....	74

## List of tables

Table 1. Incidences and main mutations in subtypes of renal cell carcinoma.....	2
Table 2. Clinical and pathologic features of the chRCC cohort .....	22
Table 3. qPCR reaction mix asssembling .....	33
Table 4. qPCR thermal cycling conditions .....	33
Table 5. Primer sequences used to amplify mitochondrial transcripts.....	34
Table 6. RT-qPCR reaction mix asssembling .....	35
Table 7. RT-qPCR thermal cycling conditions.....	35
Table 8. Used primary antibodies for the detection of mitochondrial proteins.....	36
Table 9. MRM transitions and MS parameters of the fluorogenic probes.....	37
Table 10. Gene set enrichment analysis of the chRCC proteome, listed are significantly upregulated pathways in chRCC. ....	47
Table 11. Gene set enrichment analysis of the chRCC proteome, listed are significantly downregulated pathways in chRCC. ....	47



## Appendix

The supplemental tables were uploaded to the publically available repository PeptideAtlas and can be downloaded via  
<ftp://PASS01532:PJ6745rhm@ftp.peptideatlas.org/>.

Supplemental Table S1. MaxQuant output file featuring the proteome profile of chromophobe RCC and matching kidney tissues with LFQ intensities.

Supplemental Table S2. List of quantified proteins and gene set enrichment analysis in chRCC and kidney tissues.

Supplemental Table S3. List of identified metabolites in chRCC and kidney tissues.

Supplemental Table S4. Mass spectrometry settings for targeted metabolite profiling.

Supplemental Table S5. Mitochondrial whole-exome sequencing analysis in chRCC and kidney tissues.

Supplemental Table S6. Proteome profiling and a subsequent gene set enrichment analysis of UOK276 cells supplemented with 1% amino acids in the presence or absence of 2.5% BSA versus a complete medium.



## List of publications

Y. Xiao, R. Clima, J. F. Busch, A. Rabien, E. Kilic, S. Villegas, S. Türkmen, B. Timmermann, M. Attimonelli, K. Jung and D. Meierhofer. "Activation of endocytosis to replenish amino acid favors cancer cell proliferation and survival in chromophobe renal cell carcinoma." (In preparation)

Y. Xiao, R. Clima, J. F. Busch, A. Rabien, E. Kilic, S. Villegas, B. Timmermann, M. Attimonelli, K. Jung and D. Meierhofer. "The decrease of mitochondrial DNA content causes dysregulation of OXPHOS in chromophobe renal cell carcinoma." (Submitted)

Y. Xiao and D. Meierhofer (2019). "Glutathione metabolism in renal cell carcinomas progression and implications for therapies." International Journal of Molecular Sciences 20(15): 3672. <http://doi.org/10.3390/ijms20153672>

Y. Xiao, R. Clima, J. F. Busch, A. Rabien, E. Kilic, S. Villegas, S. Türkmen, M. Attimonelli, K. Jung and D. Meierhofer (2019). "Metabolic reprogramming and elevation of glutathione in chromophobe renal cell carcinomas." bioRxiv 649046. (Preprint) <http://doi.org/10.1101/649046>

Y. Xiao and D. Meierhofer (2019). "Are Hydroethidine-Based Probes Reliable for Reactive Oxygen Species Detection?" Antioxidants & Redox Signaling 31(4): 359-367. <http://doi.org/10.1089/ars.2018.7535>

G. Kurschner, Q. Zhang, R. Clima, Y. Xiao, J. F. Busch, E. Kilic, K. Jung, N. Berndt, S. Bulik, H. G. Holzatter, G. Gasparre, M. Attimonelli, M. Babu and D. Meierhofer (2017). "Renal oncocyroma characterized by the defective complex I of the respiratory chain boosts the synthesis of the ROS scavenger glutathione." Oncotarget 8(62): 105882-105904. <http://doi.org/10.18632/oncotarget.22413>